TUM

Chair for Biological Imaging, Prof. Dr. Vasilis Ntziachristos

Optoacoustic mesoscopy in the frequency domain using laser diodes

Ludwig Rainer Prade

Vollständiger Abdruck der von der
Fakultät für Elektrotechnik und Informationstechnik
Der Technischen Universität München zur Erlangung des akademischen Grades
eines Doktor-Ingenieurs (Dr.-Ing.)
genehmigten Dissertation.

Vorsitzender: Prof. Dr.-Ing. habil. Dr. h.c. Alexander W. Koch

Prüfer der Dissertation:

1. Prof. Dr. Vasilis Ntziachristos
2. Prof. Dr.-Ing. Norbert Hanik

Die Dissertation wurde am 17.12.2018 bei der Technischen Universität München eingereicht und durch die Fakultät für Elektrotechnik und Informationstechnik am 28.09.2019 angenommen.

Zusammenfassung

Optoakustische Bildgebung bietet einen neuartigen und vielversprechenden Zugang zu medizinischen und biologischen Fragestellungen, da viele Einschränkungen existierender Systeme überwunden werden können. Hierbei werden optische Absorptionsmessungen mit hoher Auflösung bis hin zu Detektion einzelner Zellen nicht invasiv durchgeführt. Mittels multispektraler Messungen kann optoakustische Bildgebung Informationen gewinnen, die ansonsten nur mit optischen Methoden zugänglich sind, jedoch bei wesentlich höherer Auflösung in Abhängigkeit der Eindringtiefe. Optische Auflösung kann mit optoakustischer Mikroskopie erreicht werden, wobei die räumlichen Informationen durch den fokussierten anregenden Laserstrahl erzeugt wird. Dadurch wird eine Auflösung bis auf die Zellebene ermöglicht, kombiniert mit einer Eindringtiefe, welche mit optischer Mikroskopie nicht erreicht werden kann. Noch höhere Eindringtiefen sind mit optoakustischer Tomografie möglich. Die Anregung hierbei erfolgt über eine nicht fokussierte Beleuchtung, während das entstehende optoakustische Signal von mehreren Ultraschalldetektoren in verschiedenen Positionen aufgefangen wird. Zwar kann optoakustische Tomografie nicht die gleiche Auflösung wie optoakustische Mikroskopie bieten, jedoch sind Eindringtiefen bis zu einigen Zentimetern möglich. Eine weitere Implementierung der optoakustischen Bildgebung ist die optoakustische Mesoskopie. Hierbei wird das zu untersuchende Objekt mit einem fokussierten Ultraschalldetektor zusammen mit einer unfokussierten Beleuchtung abgerastert. Dadurch wird eine sehr hohe Auflösung von bis zu einigen Mikrometern erreicht, während die Eindringtiefe mehrere Millimeter beträgt, was deutlich über den Möglichkeiten mikroskopischer Methoden liegt.

Alle Modalitäten benötigen Lichtquellen zur Erzeugung von kurzen intensiven Lichtpulsen sowie hochempfindliche Ultraschalldetektoren. Jüngste Fortschritte bei Lichtquellen mit hoher Wiederholrate sowie akustischen Detektoren haben kostengünstige und benutzerfreundliche mesoskopische Systeme ermöglicht. Da jedoch entsprechende Lichtquellen mit für multispektrale Messungen geeigneten Wellenlängen nur eingeschränkt verfügbar sind, steht die multispektrale Mesoskopie immer noch einer großen Hürde gegenüber. Optischen parametrische Oszillatoren, die auch in der multispektralen optoakustischen Tomografie benutzt werden, haben vielversprechende Ergebnisse gezeigt. Allerdings ist dies mit einem hohen finanziellen Aufwand und langen Messzeiten verbunden.

Diese Arbeit zeigt einen alternativen Ansatz für schnelle, multispektrale und hochauflösende optoakustische, mesoskopische Messungen, indem die Messungen im Frequenzraum durchgeführt werden. Es konnte gezeigt werden, dass die gle-

1

iche Auflösung und Signalqualität wie bei Messungen im Zeitbereich möglich ist. Außerdem können multispektrale optoakustische Messungen mittels mehrerer Laserdioden bei verschiedenen Wellenlängen durchgeführt werden, was das Problem der beschränkten Verfügbarkeit geeigneter Wellenlängen löst, sowie kleinere und günstigere Systeme ermöglicht. Optoakustische Messungen im Frequenzraum haben zudem den Vorteil, dass Frequenzmultiplexing verwendet werden kann, wodurch multispektrale Messungen ohne negativen Einfluss auf die Dauer der Messung oder Bildqualität möglich werden. Dieser neue multispektrale Ansatz erlaubt es, die Morphologie medizinisch und biologisch relevanter Systeme zu visualisieren und gleichzeitig metabolische Informationen wie Blutsauerstoffsättigung auch in sehr kleinen Gefäßen zu erfassen. Dies wurde mit Hilfe von Messungen der menschlichen Haut verdeutlicht. Darüber hinaus kann das hier vorgestellten System gängige Kontrastmittel detektieren, welche zusätzliche Erkenntnisse, etwa über die Perfusion kleiner Blutgefäße, liefern. Dadurch können die Morphologie sowie verschiedene biologische Prozesse zeitgleich erfasst und miteinander korreliert werden. Dies wurde anhand von biologisch relevanten Modellorganismen demonstriert.

Abstract

Optoacoustic imaging has proven to be an exciting new approach to medical and biological imaging that overcomes many limitations of existing modalities. Being non-invasive, it provides highly resolving absorption measurements. In combination with its multispectral capabilities, optoacoustic imaging can provide information otherwise only obtainable by optical methods, yet at much higher resolution as a function of depth. Optical resolution can be provided by optoacoustic microscopy, using a focused excitation beam to provide the spatial information. This allows single cell resolution at penetration depths unobtainable by optical microscopy. Even greater penetration depths can be achieved in the regime of optoacoustic tomography. Here, the excitation is performed by wide field illumination while the detection of the resulting optoacoustic signal is done by transducers in multiple positions around the specimen. Although it cannot provide the same resolution as optoacoustic microscopy, optoacoustic tomography allows penetration depths up to several centimeters. Another implementation is optoacoustic mesoscopy. Here, a focusing transducer together with an unfocused light source raster scans over the specimen. This approach enables very high resolution of down to several micrometers while offering penetration depths up to several millimeters, exceeding the possibilities of optoacoustic microscopy by far.

All presented modalities rely on high energy, pulsed light sources and sensitive ultrasound detectors. Recent developments in pulsed laser light sources with high repetition rates and acoustic detection technology have allowed optoacoustic mesoscopy to be implemented in a powerful manner for various medical and biological applications. Nevertheless, limitations in the wavelength availability of suitable light sources make multispectral optoacoustic mesoscopy challenging. Adopting concepts of multispectral optoacoustic tomography using optical parametric oscillators, has shown some promising results at the cost of great financial expense and significant speed reduction.

This thesis will show a novel approach to high speed, high resolution multispectral optoacoustic mesoscopy by implementing it in the frequency domain. It shows that similar resolution and signal-to-noise ratios as in time domain implementations can be achieved in frequency domain. In addition, performing multispectral optoacoustic imaging using multiple laser diodes at different wavelengths removes the limitations in wavelength availability, form factor and cost known from traditional multispectral light sources. Furthermore, frequency domain optoacoustics allows for frequency multiplexing, thus enabling multispectral optoacoustic mesoscopy without reduction in acquisition time or image quality compared to time domain

systems. This new multispectral modality enables visualization of medical and biological relevant systems providing metabolic information such as blood oxygenation in small vessels. This has been demonstrated by human skin measurements. Furthermore, the presented system allows to visualize commonly used contrast agents. This is the first system that allows extraction of metabolic information at mesoscopic resolution in vivo and correlation with functional information provided by contrast agents, as has been demonstrated on biologically relevant model organisms.

List of Abbreviations

OA	Optoacoustic
SNR	Signal-to-noise
CNR	Contrast-to-noise
CT	Computational tomography
MRI	Magnet resonance imaging
TDOA	Time domain optoacoustics
FDOA	Frequency domain optoacoustics
AWGN	Additive white Gaussian noise
SPTD	Single pulse time domain
PWTD	Pulse wave time domain
SWFD	Single wave frequency domain
PWFD	Pulse wave frequency domain
SW	Single-wavelength
MS	Multispectral
NIR	Near-infrared
RSOM	Raster scanning optoacoustic mesoscopy
MSOT	Multispectral optoacoustic tomography
MIP	Maximum intensity projection
FWHM	Full width half maximum
OPO	Optical parametric oscillator
FFT	Fast Fourier transform
GPU	Graphics processing unit
CGI	Computer generated image
MPE	Maximum permissible exposure
ICG	Indocyanine green
CTC	Circulating tumor cell

Contents

Chapter 1

Introduction

1.1 Medical and biological imaging

A fundamental concept in health care is the ability to make a precise diagnosis of a patient's condition without affecting the patient or the condition itself to allow for evidence based treatment [1, 2]. Historically, physicians used their senses to draw conclusions and decide for the treatment. Scientific inventions have driven medical advances and can sometimes be considered extensions of the physician's natural senses. However, the information value obtained is very limited and does only reflect a small fraction of the overall state of the patient [3].

As the understanding of the interactions between energy and matter grew, it became possible to extract information of the condition of matter by the observation how it interacts with energy. New detection methods became available and the type of energy used is no longer limited by the human senses. Therefore, a whole new field of study emerged for diagnosis [4]. Some form of energy may penetrate deeply into the body, undergo interactions and deliver information not accessible otherwise. The novel field of medical imaging has revolutionized diagnosis and monitoring of diseases [5]. The progress of clinical applications is strongly correlated with advances in physics and biology. Interestingly, biological research faces similar challenges as medicine: understanding the condition of a biological system, may it be a single cell or a living organism, without affecting its very condition [6]. Nowadays, a variety of medical equipment is used to deliver healthcare services. Different scientific fields contribute significantly to the development of new technologies for medically and biologically relevant questions, making this field of research highly interdisciplinary. Visual examination of the patient may be considered the simplest and yet perhaps most relevant form of medical imaging. A metabolism is a highly cross-linked system. Therefore, any medical condition arising from a particular region or organ can affect the entire organism, including externally accessible body parts, such as the skin, eyes etc. An experienced physician can draw profound conclusion on the patients condition. However, accurate and qualitative information can only be provided by making spatially resolved measurements, introducing the field of medical imaging [7, 8].

X-Ray imaging

The first modality that allowed access to areas within the body was X-ray imaging, opening radiology as a new field of medicine [9]. X-rays feature a very short wavelength ($5 - 250$pm), about 1000 times shorter than visible light. Therefore, X-rays interact with the inner electrons in the K- and L- shells of atoms (inner photoelectric effect), which feature a much lower absorption coefficient than the molecular interaction of visible light, hence penetrating far deeper. The interaction cross section of X-rays σ is proportional to the nuclear mass of the target:

$$\sigma \propto \frac{Z^5}{E^{\frac{7}{2}}} \tag{1.1}$$

E is the energy of the X-ray photons and Z is the atomic number of the target. X-rays can provide a contrast of the distribution of heavier elements in the body. For medical applications, they allow an accurate segmentation of calcium-containing bone tissue and soft tissue [10]. X-rays are conducted as transmission measurements, where the specimen is placed between the source and the detector such as photostimulated luminescence plates (PSP). An example of a human full body scan, impressively demonstrating the penetration capabilities of X-rays is shown in figure 1.1. The entire skeleton of the trauma patient is visible and a bone fractures in both upper leg revealed. Some inner organs in the thorax and abdomen can also be seen. The lungs are well visible as they are filled with air, which does not attenuate X-rays. As X-rays examinations are transmission measurements, they generate

Figure 1.1: **Full body X-ray scan of trauma patient [11].** As the bones contain calcium, which has a higher atomic mass than the elements of other tissues, they strongly absorb X-rays, enabling bone-tissue separation. The lungs are filled with air, which interacts even less with X-rays than soft tissue. Therefore, they are well visible in the image.

maximum intensity projections (MIPs) and do not provide depth information. This was addressed by introducing computer tomographic (CT) devices. By replacing the PSP plates with electric sensors such as photomultiplier tubes or image sensors, X-ray density measurements suitable for electronic processing could be made [12]. Based on a mathematical framework, a three-dimensional distribution map of X-ray absorption could be created [13]. In addition, unlike X-ray, CT allowed

segmentation not only of bones, but also of soft tissue [14]. Functional information can be achieved by administering contrast agents [15]. Figure 1.2 demonstrates how CT imaging improves diagnostics compared to conventional X-ray imaging. It shows the right hip of a patient who has suffered a femoral neck fracture. 1.2a and 1.2b show two X-ray images that do not reveal the fracture. A subsequent CT scan presented in 1.2c clearly shows the injury.
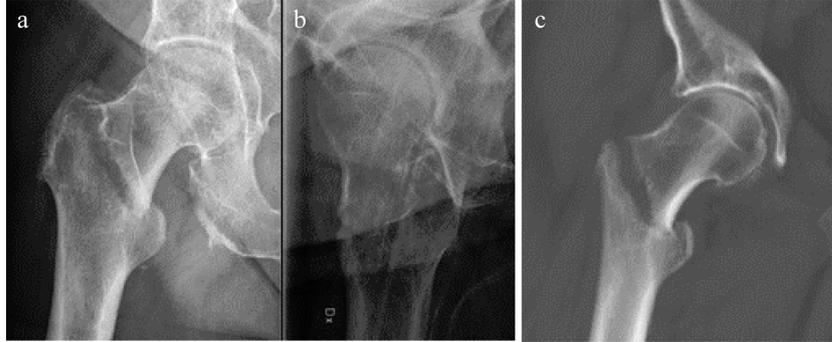

Figure 1.2: **Hip fracture unresolvable by X-ray, but visible in CT-scan.** a and b: X-ray image of hip of 78 year old patent after fall. A fracture has been masked by a skin fold and is therefore not visible. c: CT-scan of the same region revealing the injury (Image licensed under Creative Common License by Mikael Häggström).

Magnetic resonance imaging

X-rays are ionizing radiation and pose a significant burden to the patient, reducing the frequency of diagnostic scans [16, 17]. Additionally, the contrast of different soft tissues is extremely low making it difficult to identify abnormalities such as tumorigenesis in early stages. A fundamental improvement was introduced by magnetic resonance imaging (MRI) [18, 19]. In the presence of a magnetic field, spin-carrying nuclei like hydrogen orient themselves parallel to the magnetic field. When absorbing energy from an electromagnetic field, the nuclei may flip and orientate themselves anti-parallel to the magnetic field. After a characteristic relaxation time, the nuclei flip back to their original orientation, re-emitting the same energy they previously absorbed by flipping. The energy required for the flip to occur is proportional to the strength of the magnetic field and the magnetic moment of the nuclei. For a hydrogen atom, it is:

$$E_m = \mu \cdot B, \quad \mu = 8.8 \times 10^{-8}\,\text{eV/T} = 21.6\,\text{MHz/T} \tag{1.2}$$

with E_m being the energy required for the spin flip to take place, B is the magnetic field and μ is the magnetic moment of the nucleus. If the amplitude of the magnetic and electromagnetic field match equation 1.2, the spin flip may take place. The withdrawn energy from the electromagnetic field which can be detected. Imaging is performed by applying magnetic field gradients in three dimensions to the sample. This way, condition 1.2 is only fulfilled a one location in space at a time. By

varying the gradients, this location can be scanned through the sample, creating a hydrogen density map of the sample. As this is a strong indication for the type of tissue at hand, superior soft tissue contrast can be achieved with high resolution at any point in the human body. An example presenting the soft tissue contrast inside a human head is shown in figure 1.3. Various anatomical structure can be seen, including substructures of the human brain, which consist of the same cell type at different densities. For magnetic field strength in the order of a few
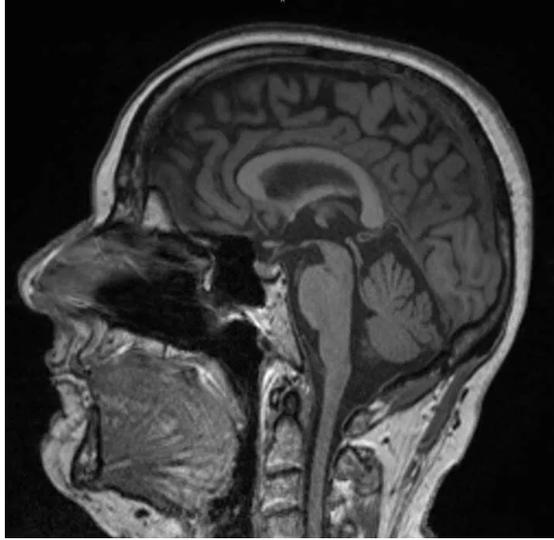

Figure 1.3: **MRI scan of human head.** The scan presents a cut through sagittal plane of a human head. The grey value of the image corresponds to the hydrogen content of the tissue. The different tissue types are clearly identifiable by their hydrogen content (Image provided by LearningNeurology.com).

Tesla, E_m is in the order of a few meV, comparable to the mean thermal energy of the hydrogen atoms at room temperature. Hence, nuclei can be flipped by their thermal energy, even if condition 1.2 is not fulfilled, causing significant noise to the MRI measurement. This can be met by using very strong magnetic fields or increasing the acquisition time. Since condition 1.2 has to be mapped over the entire sample, the magnetic field must be very homogeneous. MRI devices with strong magnetic fields are very difficult to build highlighting the main disadvantage of MRI. In addition, only one point in space can be measured at a time, resulting in long scan times of several minutes up to hours.

Sonography

Ultrasound defines acoustic waves with frequencies above $20\,\text{kHz}$ [20]. In water, this yields a wavelength of $\lambda = 7.5\,\text{cm}$ and a wavelength of below $\lambda = 1\,\text{µm}$ is obtained for frequencies in excess of $f = 1.5\,\text{GHz}$ assuming $v_s = 1500\,\text{m s}^{-1}$. Being an uncharged wave, ultrasound commonly does not strongly interact with most materials and only experiences limited attenuation, depending on the materials mechanical properties. Consequentially, it is a suitable probe to detect structures in the size of its wavelength. Depending on the application, these can be macroscopic morphology,

such as entire organs of human patients or much smaller skin features [21]. An example of the imaging potential of sonography is given in figure 1.4. Due to the

Figure 1.4: **Example for sonographic imaging of human foetus [22].** Abdominal sonographic scan of monoamniotic twins at age of 15 weeks.

limited interaction between ultrasound and matter, the contrast of sonographic imaging is general very low. The backscattered ultrasound is normally caused by acoustic impedance mismatches. In living tissue, these are very high between bone tissue, soft tissue and hollow organs (typically containing fluids or air). Other structures are typically very difficult to visualize [23]. Furthermore, ultrasound experiences an increase in attenuation at higher frequencies. This will be discussed in depth in section 1.3. Consequentially, high frequencies carrying information of small structures are readily absorbed, limiting high resolution ultrasound imaging to superficial tissue [24].

1.2 Optical imaging

Visible light interacts with the outer electrons of molecules which determine its chemical properties. Thus, it carries information about the chemical structure of the sample [25]. Consequentially, light is an ideal probe to obtain medical information. However, it is scattered by microscopic structures in the body, such as cell cores and organelles. In addition, light is absorbed by different chromophores [26]. Consequently, high resolution optical imaging can only be achieved close to the surface, where the penetration of light is short compared to the attenuation length. This is a viable method for skin or hollow organ examination [27]. Imaging deeper tissues requires biopsies, which pose serious stress to the patient. In recent years, optical imaging methods that allow for deeper penetration while maintaining high resolution have been investigated.

Optical diffuse imaging

Numerical methods to solve the scattering problem of light have been considered. Early attempts in imaging low scattering breast tissue have been made, but have

proven of little clinical value [28–30]. However, when utilizing time dependent light sources and detectors, computational methods allow to measure the spatial distribution of the absorption coefficient, an approach known as optical diffusion imaging [31]. There have been various implementations, which can be split up into two main categories, time domain systems that use short laser pulses [32, 33] and frequency domain systems that use continuous sinusoidal modulated lasers [34, 35]. These modalities allow considerable penetration depth of several tens of cm, however even the best performing systems offer resolutions in the order of mm to cm [31].

Confocal microscopy

To reconstruct the light propagation in tissue, methods based on differentiation between scattered and non-scattered photons have been considered. In biological tissue, the scattering coefficient is typically 1-2 orders of magnitude greater than the absorption coefficient. This will be discussed in detail in section 1.3. Hence, some light will be able to reach deeper layers before being absorbed, but the photons will be increasingly randomised. Confocal microscopy allows to select the non-randomized photons by leading the beam path through a pin hole [36, 37] (fig. 1.5a). The incident light (blue) originates from the source filtered by pinhole and is guided to the sample through an objective lens. The florescence light from the focus of the objective passes back through the objective and travels back to the detector behind another pinhole. The pinhole will reject any light that does not originate from the focus of the objective. Figure 1.5b shows a biological sample that has been imaged using confocal microscopy. Figure 1.5c shows the same sample after the pinholes have been removed, so that the setup behaves like a conventional microscope.
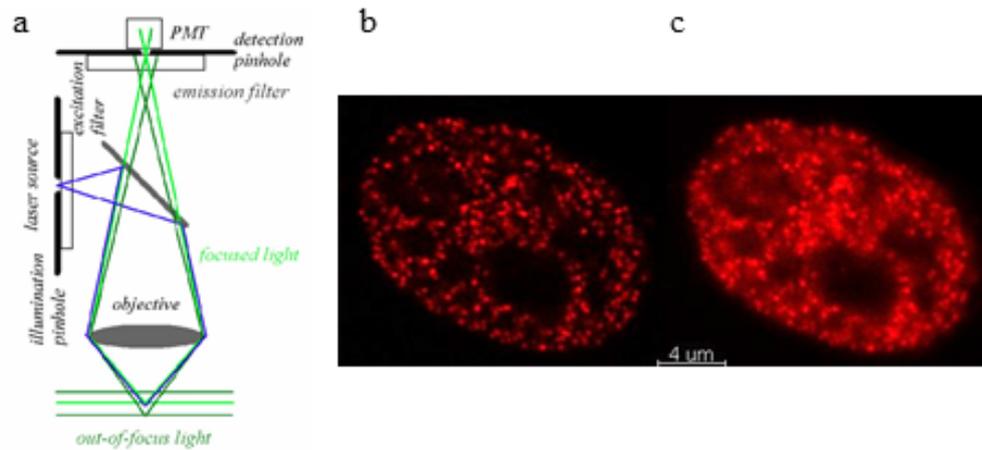
Figure 1.5: **Principal of confocal microscopy and illustrative example [38].** a: conceptional of confocal microscopy. b: single HeLa-cell nucleus with labeled DNA acquired by confocal microscope. c: Same image acquired with the pinhole opened completely, removing the confocal effect.

Two photon microscopy

Alternatively, two photon processes can be use to enhance the penetration depth [39] (fig. 1.6a). The detection wavelength is chosen to be half of the excitation wavelength. Two photons have to combine in a non-linear process to generate a detectable signal. This implies that the output signal is proportional to the photon density squared [40] (fig. 1.6b). This results in a more defined focus, even in the presents of scattering [38] (fig. 1.6c). However, non-linear processes are highly depended on the light flux, hence most applications require pulsed lasers to generate detectable two-photon signals. This increases the system cost and puts limits on the acquisition speed, to avoid the tissue to be damaged by the high light flux.
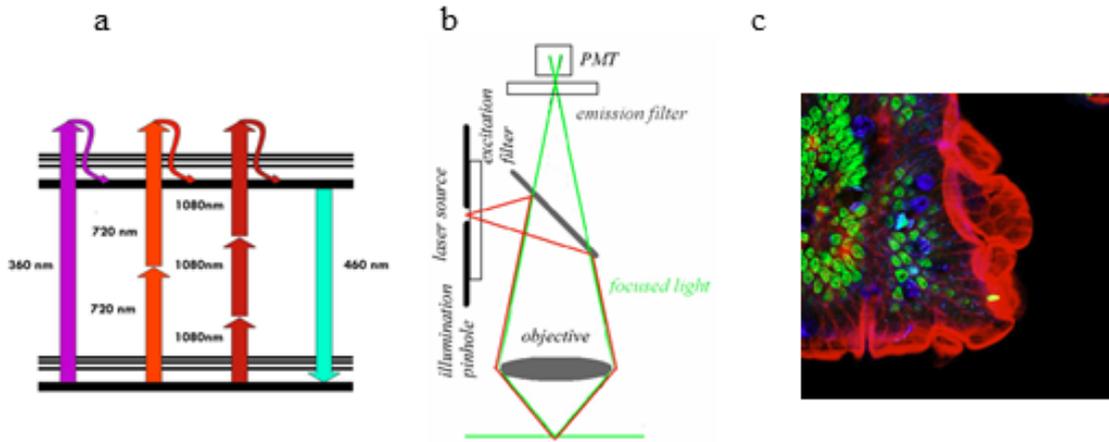
Figure 1.6: **Principal of two-photon microscopy and illustrative example [38].** a: Energy states which are excited by two low energy photons simultaneously result into a single high energy photon at a shorter wavelength. b: Setup of a two-photon microscope: the fluorescence light is separated from the excitation light by a dichroic beam splitter. Only the fluorescence light from the focus reaches the detector. c: Two-photon image of a cryosliced mouse intestine. Different cell features are labeled with different fluorescence agents.

Optical coherence tomography

Optical coherence tomography (OCT) is a method were large volumes can be acquired and allows enhanced penetration depth. The concept of OCT is to replace the pin hole of a confocal microscope with a Michelson Morley interferometer using a low coherence light source (fig. 1.7a). The sample under investigation is placed at the end of one arm of the interferometer. By scanning the mirror position on the reference arm, photons reflected from the depth within the sample corresponding to the length of the reference arm undergo constructive interference, allowing depth segmentation. Hence, depth scanning is performed in the time domain [41]. Using a OCT scan of human skin, detailed anatomical features can be resolved (fig. 1.7b). The image also demonstrates the limited penetration depth of OCT and the inability to resolve strongly absorbing features, such as blood vessels.

A common problem of these microscopy technique is that the focus has to be scanned in three dimensions, which leads to long acquisition times. A solution is presented by frequency domain (or spectral) optical coherence tomography (FD-OCT) featuring a wideband light source [43]. In this implementation, each optical wavelength in the excitation source corresponds to a different penetration depth. Using a spectroscopic detector, depth information can be acquired without the need for scanning. Finally, another implementation of optical coherence tomography utilizes a light source with a sweep-able wavelength (swept-source OCT) [44]. As in FD-OCT each optical wavelength covered by the source corresponds to a particular
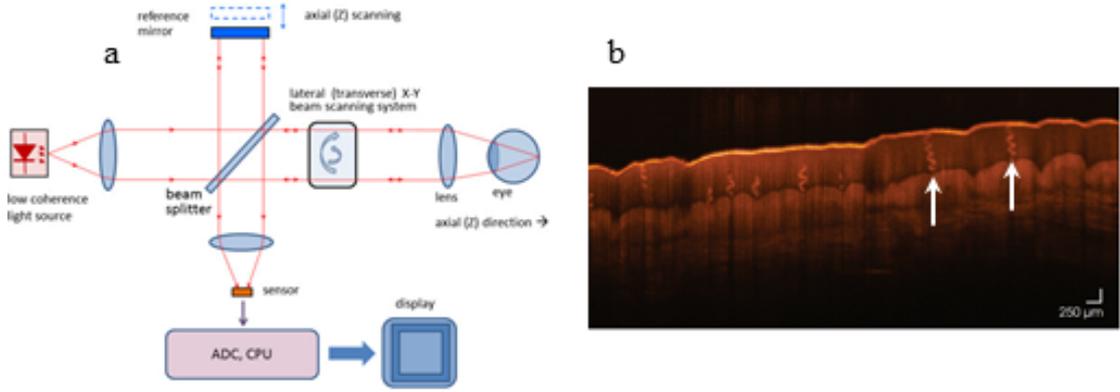
Figure 1.7: **Principal of optical coherence tomography [42] and illustrative example.** a: System setup of a time domain optical coherence tomography setup, a combination of a Michelson interferometer and a confocal microscope. b: OCT scan of human skin. The high resolution is illustrated by various skin features, including sweat glands (white arrows, copyright by Thorlabs).

penetration depth, which is being mapped into the time domain. However, a frequency sweep can be performed extremely fast, enabling accelerated image acquisition [45].

1.3 Propagation of light and sound in tissue

This chapter will give an introduction to understand the limiting factors of penetration depth and resolution for light and sound in biological tissue.

Reflection and refraction of light and sound in tissue

Ultrasound and light travel as waves through a medium. Therefore, the processes influencing their propagation are similar. Sound wave propagation is described by the pressure wave equation [46]:

$$\Delta \vec{p} = \frac{1}{v_s^2} \frac{\partial^2 \vec{p}}{\partial t^2} \tag{1.3}$$

where p is the pressure and v_s the speed of sound in the medium under consideration. Similar, the propagation of light being an electromagnetic wave is described by the wave equation deduced from the Maxwell equations [47]:

$$\Delta \vec{E} = \frac{1}{c^2} \frac{\partial^2 \vec{E}}{\partial t^2}$$

$$\Delta \vec{B} = \frac{1}{c^2} \frac{\partial^2 \vec{B}}{\partial t^2} \tag{1.4}$$

where $\vec{E}$ is the electric field, $\vec{B}$ is the magnetic flux density and c the speed of light in the considered medium. Both equation share the same form and can be solved by:

$$p(\vec{r}, t) = p(\vec{r_0}, t_0) \cdot e^{j \cdot \left(n \cdot \vec{k} \cdot \vec{r} - \omega t \right)}$$

$$\vec{E}(\vec{r}, t) = \vec{E}(\vec{r_0}, t_0) \cdot e^{j \cdot \left(n \cdot \vec{k} \cdot \vec{r} - \omega t \right)}$$

$$\vec{B}(\vec{r}, t) = \vec{B}(\vec{r_0}, t_0) \cdot e^{j \cdot \left(n \cdot \vec{k} \cdot \vec{r} - \omega t \right)} \tag{1.5}$$

where $\vec{k}$ is the wave vector pointing in the direction of propagation with the magnitude being $\frac{2\pi}{\lambda}$ and λ is the wavelength and n the refractive index. While light waves are always transverse waves, ultrasonic waves can be both transverse or longitudinal if the medium they travel in have a non-zero bulk module. Longitudinal and transverse sound waves typically have different speed of sound making them difficult to use as a probe for imaging. As only solid bodies have a non-zero bulk modulus and they are not typical media under consideration in optoacoustic imaging, this thesis will consider sound waves to be longitudinal waves only. Both ultrasound and light waves can be reflected and refracted at the interface between two media. The magnitude of the reflected and transmitted part of the wave is determined by the angle of incidence to the interface and the wave impedance Z_1 and Z_2 of the involved media. As light waves are transverse, the polarization angle between the light wave and the interface also plays a role and the reflectance is determined by the Fresnel-equations [48]:

$$R_s = \left| \frac{Z_1 \cdot \cos(\theta_i) - Z_2 \cdot \cos(\theta_t)}{Z_1 \cdot \cos(\theta_i) + Z_2 \cdot \cos(\theta_t)} \right|^2$$

$$R_p = \left| \frac{Z_2 \cdot \cos(\theta_t) - Z_1 \cdot \cos(\theta_i)}{Z_2 \cdot \cos(\theta_t) + Z_1 \cdot \cos(\theta_i)} \right|^2 \tag{1.6}$$

where R_s is the reflection coefficient for light polarized perpendicular to the plane between the two media. R_p is the reflection coefficient for the part of the light polarized in parallel to the plane. In strongly scattering media, such as biological tissue, light is commonly not polarized. The reflection coefficient of sound waves can be calculated by:

$$R = \frac{Z_1 - Z_2}{Z_1 + Z_2} \tag{1.7}$$

Furthermore, the impedance mismatch between two media causes a propagating wave to change direction, an effect known as refraction. It is due to the different

phase velocity of the two media and is described by the following equation:

$$\frac{sin(\theta_1)}{sin(\theta_2)} = \frac{v_1}{v_2} = \frac{n_2}{n_1} \tag{1.8}$$

The reflection of sound waves follow a similar law, yet since longitudinal waves do not feature polarization. Z_1 and Z_2 are the wave impedances of the two media, θ_i is the angle of incidents and θ_t is the transmitted angle, determined by the law of refraction [48]:

$$\frac{\sin(\theta_i)}{\sin(\theta_t)} = \frac{Z_2}{Z_1} \tag{1.9}$$

This equation holds true for both sound and light waves. As different tissues have different acoustic impedance, refraction can have a significant effect on the image quality of ultrasound, especially on larger scales. In particular, the mismatch between the skin and lower layers of the body can affect sound propagation away from ideal *straight-lines.*

Absorption and scattering of light and sound in tissue

The impedance for both light and sound can include an imaginary component. In this case, the wave will be attenuated as it travels through media [47]. The imaginary part of the wave impedance is the attenuation coefficient, as can be seen when replacing n in equation 1.5 by $n = n_1 + i \cdot n_2$:

$$x(\vec{r}, t) = x(\vec{r_0}, t_0) \cdot e^{-n_2 \cdot \vec{k} \cdot \vec{r}} \cdot e^{j \cdot \left(\vec{k} \cdot \vec{r} - \omega t\right)} \tag{1.10}$$

The complex component of the refractive index yields an exponential decay of the waves amplitude. By defining $n_2 = \mu_a$ as the absorption coefficient:

$$I(x) = I_0 \cdot e^{-\mu_a \cdot \vec{k} \cdot \vec{r}} \tag{1.11}$$

The absorption of ultrasonic waves is generally wavelength-dependent. This allows to define a material and frequency specific absorption coefficient $\mu_A(\lambda)$. The frequency dependent acoustic absorption coefficient of various materials is shown in figure 1.8. The main source for light absorption in the visible regime in living tissue are hemoglobin and melanin. They both feature strongly wavelength-dependent absorption spectra. They are shown together with other important absorbers in figure 1.9. Especially hemoglobin features very strong absorption for light at 400–550 nm essentially inhibiting the propagation of light in blood at these wavelength. In most healthy tissues, blood is not abundant: it is only present inside blood vessels. This fact can be used to visualize contrast agents, occupying other regions of the visible spectrum. Figure 1.10 presents a number of contrast agents with absorption regions in the red and near infra-red, of which the absorption of biological chromophores is expected to be low.

Besides absorption, scattering is the second important mechanism that affects the propagation of waves. If scattering objects are much larger than the wavelength,
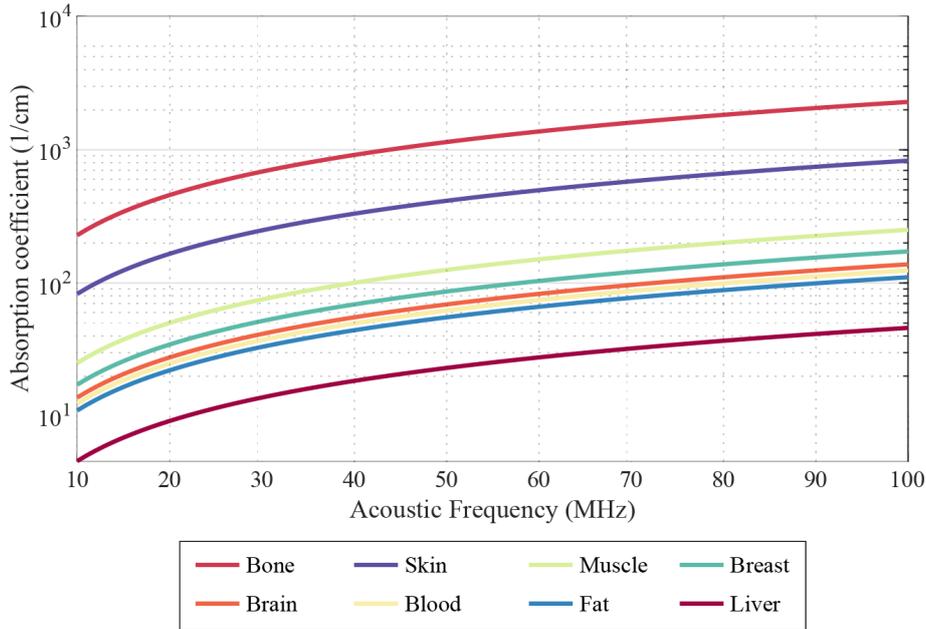
Figure 1.8: **Acoustic absorption coefficient in living tissue.** The absorption coefficient is documented at 1 MHz and is assumed to rise proportional to frequency [49].

reflection and diffraction occur and the actual scatterer's dimensions do not play a major role. However, if objects are of equal size or small compared to the wavelength, the Lorenz-Mie theory provides a comprehensive description of the scattering process [58]. The Lorenz-Mie theory can be simplified if the scatterer is much smaller than the involved wavelength (Rayleigh limit). In this case, the scattering cross section is described by [59]:

$$\sigma_{Ray} = \frac{2\pi^5}{3} \cdot \frac{d^6}{\lambda^4} \left(\frac{n^2 - 1}{n^2 + 2}\right)^2 \tag{1.12}$$

where d is the object's diameter, λ is the wavelength and n is the index of refraction. Rayleigh scattering is highly dependent on the scatterer's diameter and the wavelength. Thus, Rayleigh scattering decreases strongly with increasing wavelengths. This approximation is valid for objects up to several times smaller than the wavelength. For bigger objects, analytic solutions or approximations to the Lorenz-Mie theory become difficult to obtain. Even simple scatterers, such as homogeneous spheres, feature highly irregular scattering properties. In summary, the dependency on the wavelength becomes much weaker, until it bridges to the regime of bulk reflection and diffraction between interfaces. A list of the optical scattering coefficients in various tissue is given in figure 1.11. For very short wavelengths at which the energy of photon becomes comparable to the rest mass of the scattering object, scattering at nuclei or inner electrons become relevant [60]. For instance, this is the case of X-ray scattering on electrons. These processes have no relevance in the optical and infra-red region, and are discussed elsewhere [61].
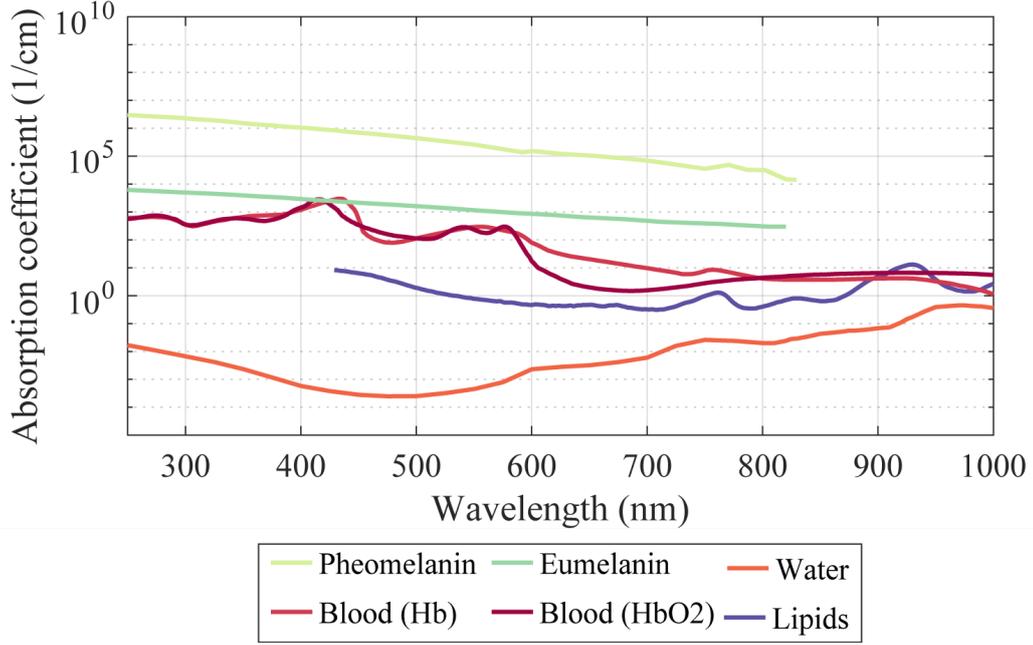
Figure 1.9: **Optical absorption coefficient in living tissue [50–56].** Important chromophores found in living tissue. The absorption has been scaled to their expected concentration.

In biological tissue, sources of scattering could be substructures of cells, such as cell nuclei or organelles with typical dimensions of several hundred nm to a few µm. The dimensions match the wavelength of light in the optical and near infra-red region, but the wavelength of ultrasound is much larger. Hence optical and infra-red light will undergo Rayleigh and Mie scattering, while ultrasound waves only "sees" the average wave impedance. The scattering coefficient of ultrasonic waves in tissue is much lower than that of visible light. This explains why high resolution ultrasound imaging is possible several centimetres inside biological tissue, while optical resolved imaging is limited to a few hundred µm.

In general, the effect of absorption and scattering on the penetration of light through media cannot be studied independently. The radiation energy transport equation provides an accurate model of light propagation and explains the effect of scattering and absorption in more detail [62]:

$$\frac{\partial L(\vec{r}, \hat{s}, t)/c}{\partial t} = \tag{1.13}$$

$$- \quad \hat{s} \cdot \nabla L(\vec{r}, \hat{s}, t) \tag{1.14}$$

$$- \quad (\mu_a + \mu_s) \cdot L(\vec{r}, \hat{s}, t) \tag{1.15}$$

$$+ \quad \mu_s \int_{4\pi} L(\vec{r}, \hat{s}, t) \cdot P(\hat{s}', \hat{s}) d\Omega' \tag{1.16}$$

$$+ \quad S(\vec{r}, \hat{s}, t) \tag{1.17}$$
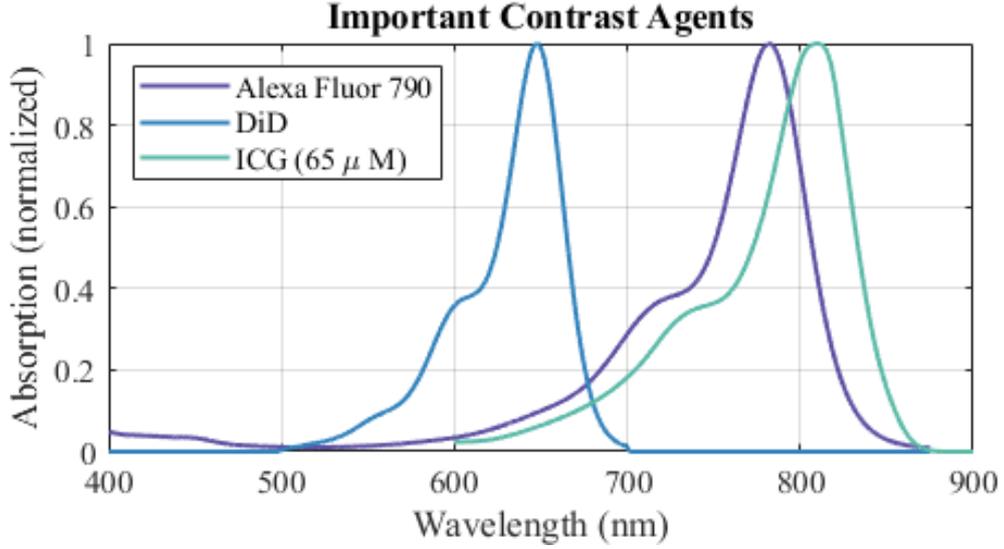
Figure 1.10: **Optical absorption coefficient of selected contrast agents [57].** The absorption spectrum of ICG varies depending on its concentration. The given value was chosen as it closely reflects values used later on in this thesis. All spectra are normalized.

The equation expresses the rate of change of radiance L:

$$L(\vec{r}, \hat{s}, t) = \frac{\partial^2 \Phi_e(\vec{r}, t)}{\partial \hat{s} \partial A \cdot cos(\theta)} \tag{1.18}$$

(Φ_e is the radiant flux in Watt $A \cdot cos(\theta)$ is the projected area) over the solid angle $\hat{s}$ at a given point $\vec{r}$ as a function of four terms and time.

1. Term 1.14 represents the diffusion of light or *random walk* of photons through the scattering media.

2. Term 1.15 takes into account any photons that have been scattered away from $\vec{r}$ or have been absorbed. As this term weighs absorption and extinction equally, they cannot be separated simply by measuring L.

3. Term 1.16 refers to the directionality of scattering by weighting the radiance with the phase function $P(\hat{s}', \hat{s})$ which determines the angular distribution of a scattering event.

4. Finally, term 1.17 represents the source term, which represents any photons added by an external light source.

No general numeric solution for the radiation transport equation exists. However, it can be solved by Monte-Carlo approaches [63]. For typical parameters of scattering tissue, the direction of the incoming photons becomes randomized within a few $100 \, \mu m$, but photons are not absorbed, as the optical absorption coefficient is much less than the scattering coefficient (fig. 1.9 and 1.11), allowing randomized photons to penetrate for several millimeter or more.
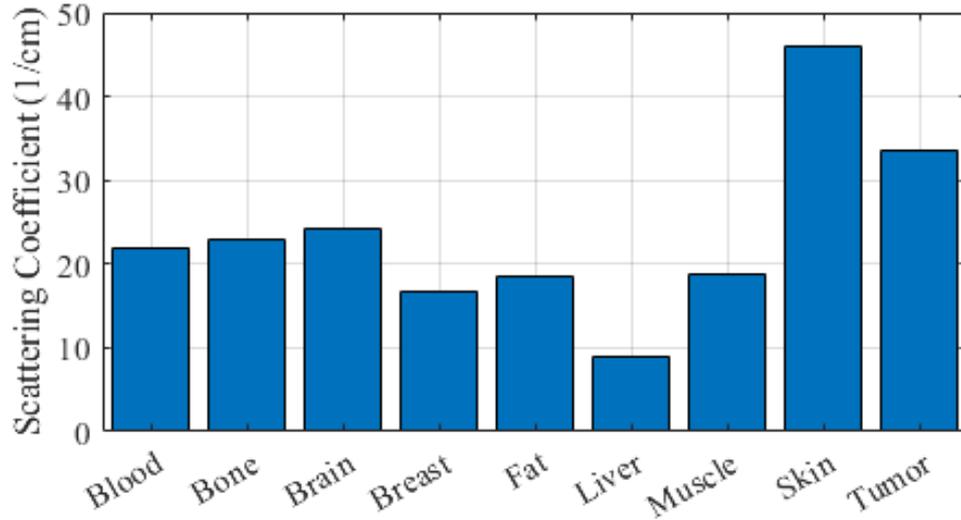
Figure 1.11: **Optical scattering coefficient in living tissue.** Presented values are collected from multiple, applicable sources [26].

1.4 Methods for optoacoustic signal generation

Before powerful pulsed light sources became available, optoacoustic measurement have been performed using natural light sources [64] or continuous sources that have been amplitude modulated [65–69]. The strength of the optoacoustic signal is proportional to the rate of change of the heating function. This means that an intensive laser pulse as made available by state-of-the-art light sources provides a rapid rate of change resulting in strong optoacoustic signals. The weak optoacoustic signals provided by excitation from continuous light sources could only be detected in combination with lock-in methods.

Continuous wave lasers consist of a gain medium inside a resonator, and a pump source (fig. 1.12) [70]. When the pump source creates a state inversion inside the gain medium, photons are created by spontaneous emission (the gain medium is pumped by causing a state inversion as shown in figure 1.12a). These travel through the gain medium and de-excite other states through stimulated emission. The coherent photons are contained inside the cavity and the stimulated emission process continues. The cavity of continuous wave lasers consist of one highly reflecting mirror and one slightly less reflecting mirror. When the number of photons being created by the pump source is greater than the number of photons leaving the cavity or being absorbed, the number of stimulated photons increases rapidly, the laser begins *lasing.* This is marked by the sharp increase in output power and leveling off of the stored energy, followed by an equilibrium between the two quantities, allowing a small portion of the laser light to be continuously coupled out of the cavity (fig. 1.12b).

State-of-the-art optoacoustic imaging systems utilize powerful, short laser pulses which are commonly provided by Q-switched lasers [71]. These are based on the same setup as continuous wave lasers, except that they feature a switchable element
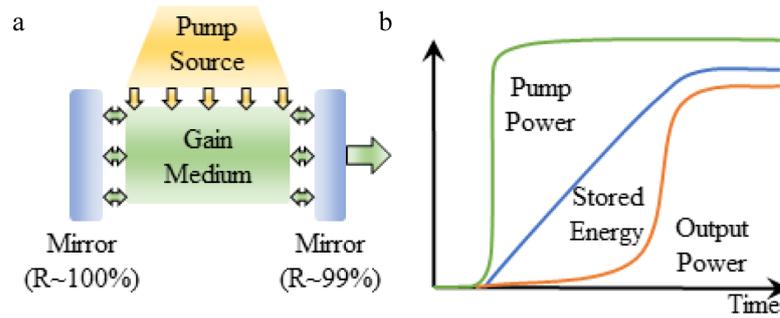
Figure 1.12: **Simplified principle of operation of continuous wave laser.** a: Schematic setup of a continuous wave laser. b: When the pump source is turned on, it causes a state inversion in the laser gain medium. This gives rise to spontaneous emission of photons, which travel through the cavity and are reflected back into it by the high reflective mirrors. This causes the number of photons in the cavity to increase (as stored energy), giving rise to amplified spontaneous emission. Some photons are lost due to absorption or the imperfect reflectivity of the mirrors. When the gain of the spontaneous amplified emissions exceeds the losses, the cavity starts lasing, causing a rapid increase in output until an equilibrium between pumping lower, losses and output power is reached.

that introduces loss to the cavity. This allows the gain medium to be excited from the pump source, but avoids the setup to lase, as the losses introduced are larger than the round trip gain (fig. 1.13a) [72]. When the gain medium has been saturated (fig. 1.13c), the switchable element is triggered, suddenly reducing the loss of the cavity. This will cause the setup to start lasing and reach a very high output power quickly, as the gain medium is fully saturated (fig. 1.13b). However, the pump source cannot re-excite the gain medium at the same rate it is being exhausted, the output power will quickly fall below the laser threshold again. This causes powerful (1–100 mJ) yet short (1–10 ns) pulsed to be created suitable for optoacoustic excitation. Q-switches can either be active or passive. Active Q-switches are Pockels or Kerr cells [72, 73]. They allow laser pulses to be triggered by an external source. Alternatively, saturable absorbers may be used which turn transparent rapidly once the photon flux has reached a given threshold [74]. These provide higher repetition rates and shorter pulses compared to actively Q-switched lasers, but do not allow laser pulses to be triggered.

The necessity to withstand the high photon flux limits the availability of gain media. Consequentially, most Q-switched lasers operate in the NIR. This represents a major drawback for medical or biological applications because the contrast in the NIR is lower than in the visible (sec. 1.3). This can be addressed by introducing non-linear frequency doubling techniques [75]. However, multispectral imaging requires measurements at a multitude of different wavelengths. The problem can be solved by introducing optical parametric oscillators (OPO). These non-linear
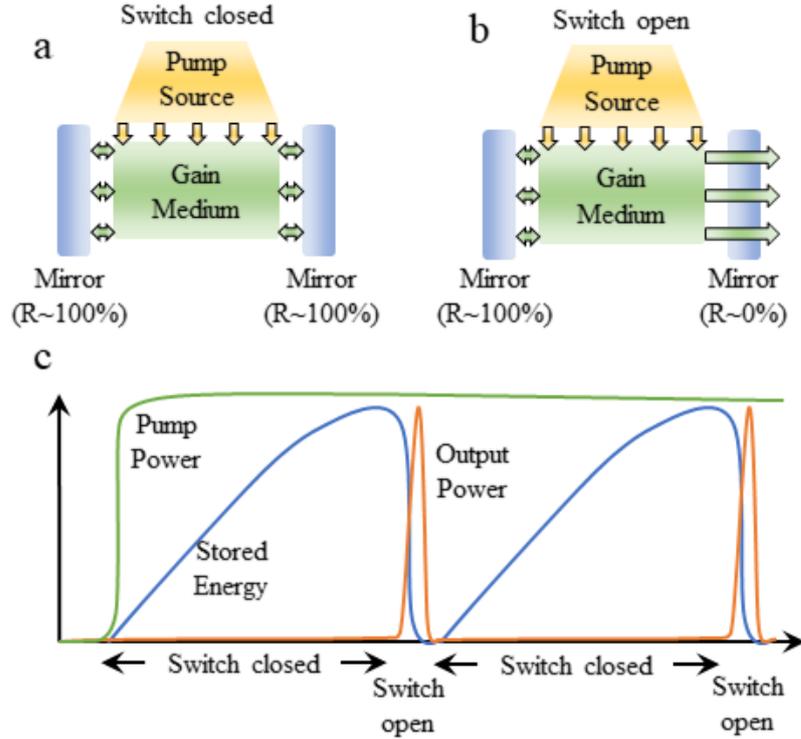
Figure 1.13: **Simplified principle of operation of Q-switched laser.** Similar as in a continuous wave laser, a pump creates a state inversion in the gain medium. a: no photons are able to leave the cavity. This causes the number of photons of the cavity to increase continuously. b: When the Q-switch is opened, all photons can leave the cavity simultaneously, creating a short yet powerful pulse. c: After the stored photons have been released, the switch is closed and the process repeats.

crystals allow a continuous conversion of radiation from a coherent light source to longer wavelengths [76–78]. As the OPO process has a high energy threshold before it occurs efficiently, Q-switched lasers are ideal sources to drive OPO systems. As the output of OPOs is always at longer wavelength than the input, a pump source in the UV must be used to provide down-converted radiation in the visible. Up-converting a Nd:YAG laser from 1064 nm to 355 nm has proven to be a feasible method to do so [79].

1.5   Methods for optoacoustic signal detection

In order to quantify the spatial distribution of the absorption coefficient $\mu_a(\vec{r})$, the optoacoustic pressure field must be measured along every infinitesimal point on a closed surface surrounding the volume of interest. The measurement must be invariant to the frequency content of the signal and the direction at which it arrives at the measurement surface. This requirement is faced with several practical limitations. A detector featuring a non-zero sensitivity must also have a finite

spatial expansion. Thus, measuring the pressure field at infinitesimal small points is not possible. Next, detectors with infinite bandwidth, are unknown. Therefore, the effect of the limited bandwidth of the utilized detector must be accounted for. Finally, the exact properties (i.e. sensitivity and bandwidth) of most detectors is affected by the angle under which it is oriented to the ultrasound source. In typical optoacoustic applications, the temperature rise induced by the laser pulse is in the order of a few mK and the resulting pressure wave amplitude is in the order of several Pa upon arriving at the detector. Consequently, sensitive detectors are of the essence to achieve reliable measurements. This however contradicts the requisite of high spatial resolution necessitating a careful tuning between these two fundamental requirements. Several technological solutions to this problem have been suggested.

| (a) | (b) |

Figure 1.14: **Internal configuration of piezoelectric transducer.** a: After the sound is coupled into the active element, it induces an electric potential proportional to the instantaneous amplitude of the sound wave. This voltage is transported to a connector and can be measured. Finally, the sound wave is absorbed by the backing layer to avoid reflections [80]. b: Impedance matching techniques may be used to improve the coupling efficiency.

Piezoelectric transducers similar to those used in conventional ultrasound measurements may be used to detect optoacoustic signals (fig. 1.14) [81]. The ultrasonic wave is coupled into the active (piezoelectric) element. The stress induced by the acoustic wave on the material gives rise to a piezoelectric potential that can be measured using a high impedance voltmeter (fig. 1.14a). Typically, the acoustic impedance of the piezoelectric material and the medium in which the ultrasonic wave travels (air or water) differ greatly. In result, a large portion of the ultrasonic wave will be reflected from the active element and is lost. This can be avoided by introducing an impedance matching layer (fig. 1.14b) [82]. The matching layer is optimized for a single frequency, close to the resonance frequency of the active element. However, through multiple matching layers, broadband matching can be achieved. In addition, a backing layer behind the piezoelectric may be introduced to avoid reflections at the rear end of the piezoelectric element.

The thickness of the active element corresponds to half the wavelength of its

resonance frequency [81]. Like a damped harmonic oscillator, the active element may oscillate at other frequencies close to the resonance frequency, but the amplitude will be lower. Increasing the damping (decreasing the Q-factor) of the oscillator will increase the bandwidth of the resonance curve (fig. 1.15a). Hence, the bandwidth of the transducer is linked to its sensitivity. Some applications utilize completely undamped active elements to achieve superior sensitivity over a very narrow bandwidth [83]. However, optoacoustic imaging utilizes very wide band signals which also achieve high spatial resolution. Therefore, it is necessary to use broadband transducers for optoacoustic imaging. As the properties of the piezoelectric material fundamentally define the bandwidth and sensitivity of the detector, there is a high incentive to develop better suited materials [84]. Great advances have been made with piezo-composite materials, that feature a much larger bandwidth than simple piezoelectrics. Another material with favourable properties is polyvinylidene fluoride (PVDF) [85]. While its sensitivity is inferior to that of piezo-composite, the acoustic impedance of PVDF is much closer matched to that of water. Hence impedance matching is not required for PVDF based transducers. In addition, PVDF is a flexible material that can be brought into almost arbitrary shapes with relative ease.
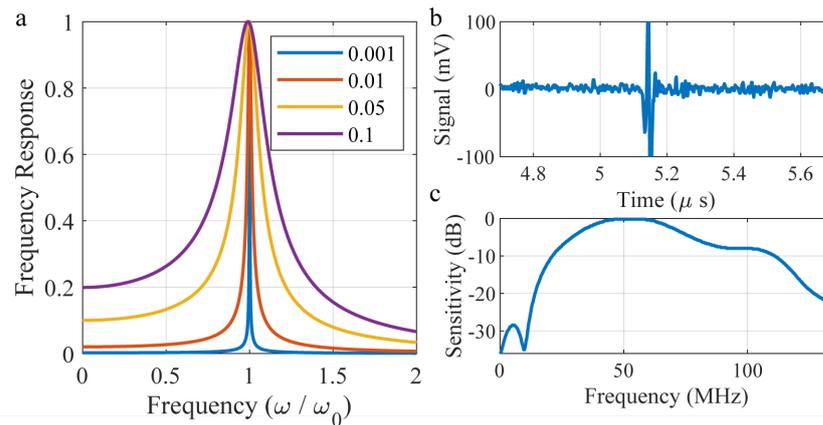

Figure 1.15: **Frequency response of harmonic oscillator and of real transducer.** a: Frequency response of harmonic oscillator for different damping coefficients. The curve for each damping coefficient has been normalized. b: Impulse response of 50 MHz transducer in time domain c: Frequency response of transducer with 50 MHz central frequency (Data taken from datasheet of SNX140517_HFM23, Sonaxis).

Increasing diameter of the piezoelectric element exposed to the ultrasonic wave augments the achievable sensitivity, since the acoustic pressure is acquired over a larger area. In return, the spatial resolution of the element is determined by its diameter and deteriorates as the elements diameter increases. For three-dimensional optoacoustic imaging, high spatial resolution is required. A possible solution is to utilize focused ultrasonic transducers (fig. 1.16a). Unlike conventional transducers, the piezoelectric element is shaped conically or a focusing lens is placed in front of it (fig. 1.16b). Such transducers will present a resolution corresponding to the

diameter of the beam at the focal point d_{lat}, which can be defined by the waist diameter of the transducers acoustic field in the focus. The dependency between frequency and waist diameter is given in figure 1.16c. The 6 dB cut-off is given by [80]:

$$d_{lat} = 1.02 \cdot \frac{Fc}{fD} = 1.02 \cdot 2 \cdot NA \cdot \frac{c}{f} \tag{1.19}$$

where F is the focal length of the transducer, c is the speed of sound of the
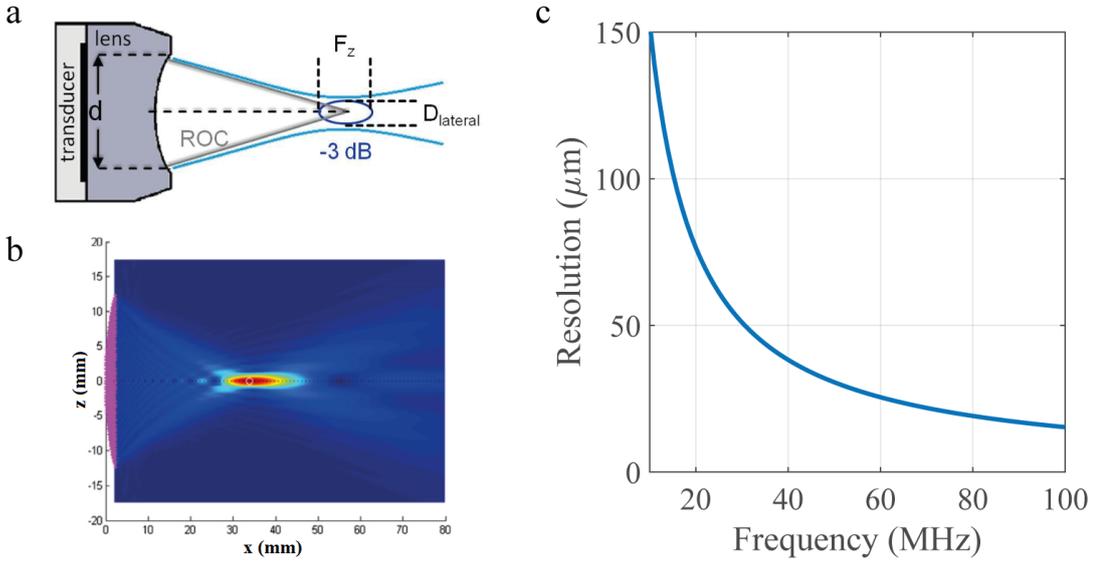
Figure 1.16: **Defining parameters and resolution of focusing transducers.** a: Definition of lateral resolution of focusing transducer, as the diameter of the focal zone F_z [86]. b: Simulation of sensitivity zone of focused transducer [87]. c: lateral resolution of focused transducer ($NA = 1$) as a function of the frequency.

medium, f is the frequency under consideration, and D is the diameter of the active element. NA is the numeric aperture of the transducer which can be expressed as $NA = D/F$. It is important to note that the resolution is frequency dependent (fig. 1.16c). Hence, the resolution defined by the beam diameter does not correspond to the theoretical limit. Using a focusing transducer will result in a gain of sensitivity compared to using a transducer featuring an element diameter of d_{lat}. At the focal point, the gain corresponds to:

$$G_f = 4 \cdot \frac{F \cdot c}{f \cdot D^2} \tag{1.20}$$

For typical transducers, G_f can reach 30–40 dB. However, the sensitivity will drop sharply when moving away from the focal point. The sensitivity field can be calculated by determining the sensitivity field at each frequency weighting it with the sensitivity of the transducer and adding them together.

A focused transducer only accepts ultrasonic signals originating from within its numerical aperture acceptance angle. In practice, this will result in a reduction in the achievable resolution. Using focused detectors with an aperture as big as possible benefits the image resolution of optoacoustic imaging systems.

Alternatively, optics-based detection methods have been suggested. In one implementation, these consist of two reflecting surfaces spaced several 100 nm apart, which forms a cavity for light whose wavelength corresponds to a multiple of the optical path length within the cavity [88,89]. The broadness of the resulting resonance depends on the reflectivity of the surfaces. The higher the reflectivity, the narrower the resonance curve becomes, which is characterized by the finesse $\mathcal{F}$. If this cavity is exposed to a ultrasonic pressure wave, the cavity length and the wavelength of the resonance light change, respectively. Numerous schemes exist to interrogate the cavity. An economic method is to use a narrow-banded continuous wave laser, whose wavelength is slightly offset to the resonance wavelength of the cavity so it matches the flank of the resonance curve. If the resonance curve varies as it is compressed or elongated by the ultrasonic wave, the transmission at the interrogation wavelength will chance proportionally. Increased finesse of the cavity results in higher sensitivity of the ultrasound detection. Etalon cavities can reach substantial sizes. Together with an appropriate readout system, spatially resolving detection can be provided. They can be interrogated by scanning microscopy or compressed sensing [90]. Due to their elasticity, etalon-based cavities commonly feature a low $\mathcal{F}$, mainly because the cavity length cannot be controlled very accurately [91].

Successful optoacoustic measurements utilizing Fiber-Bragg gratings and π-shifted Bragg gratings in integrated optics have been reported [92,93]. Since the sensitivity of the cavity depends on the amount of ultrasound coupled into it and $\mathcal{F}$, accurate process control, such as in integrated optics, allow high sensitivity as the finesse of these devices can be very high. In relation to the size of the sensitive element, π-shifted Bragg gratings feature a sensitivity several orders of magnitude larger than piezoelectric transducers. Hence, focusing is not required to enhance the sensitivity. As an alternative method, optical detection of the skin movement have been proposed as a mean to monitor the sound field due the optoacoustic effect [94,95]. While this method has the unarguable advantage of being entirely non-contact, the sensitivity has not been sufficient for high resolution *in vivo* imaging.

1.6 Development of optoacoustic imaging

Initially, optoacoustics was invented as a mean of telecommunication [64]. A flexible mirror was used to reflect sunlight to a distant light absorbing membrane (fig. 1.17). When spoken close to the mirror, sound pressure causes the mirror to deform, the mirror behaves as an acousto-optic modulator [96]. The reflected light is modulated with the waveform of the speaker's voice. This will induce an optoacoustic effect in the absorber, whose amplitude is proportional to the time derivative of the original speech pattern. This will cause the membrane to oscillate in a related pattern.

These findings were soon used to study the spectral absorption properties of materials (fig. 1.17). Some attention was drawn to this new method [98–100]. However, the absence of powerful light sources and sensitive microphones
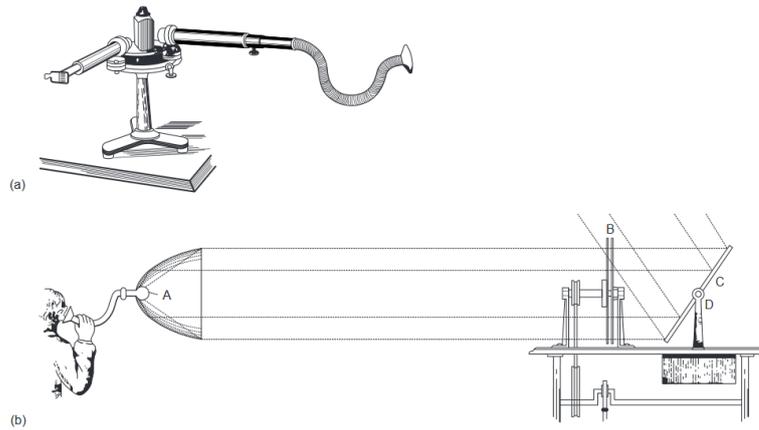
Figure 1.17: **Principal of photoacoustic setup by Bell [64].** a: Detection setup for optoacoustic spectroscopy, consisting of a spectrometer were the eyepiece has been replaced by a membrane and hearing tube. b: Photoacoustic spectrometer using sunlight. The substance under investigation A is illuminated by sunlight, that has been modulated by a chopper B after being reflected by a mirror C and spectral filter D [97]).

limited the usability of *photoacoustic spectroscopy.* Progress was reported as microphones became available as sensitive detectors to allow gas analysis using infra-red light sources, utilizing continuous wave sources and a mechanical chopper [65]. Sensitivities for trace gases down to 10^{-6} were reported [66]. Further interest was sparked upon the invention of laser light sources, as they provided much higher radiance than earlier thermal sources [101]. In addition, the pulse repetition rate of lasers can be controlled at a much higher precision than using a continuous light source and a chopper, in contrast to earlier implementations [102, 103]. This allows to utilize lock-in amplifiers which are designed to detect periodic signals at a much higher sensitivity than non-periodic signals. Consequently, the detection threshold of gaseous samples can be reduced to 10^{-8} [69]. Thereafter, *photoacoustic spectroscopy* was applied to solids, as a novel modality to measure the absorption spectrum of solid bodies without depending on difficult and inaccurate reflectance measurements [104].

1.7   History of medical optoacoustic imaging

Light transport in tissue is dominated by scattering and absorption (eq. 1.13) [105]. In consequence, measuring the spatial light distribution does not allow to separate between these two components, since one is not negligible with respect to the other. In tissue, optical scattering is typically one order of magnitude more dominant than absorption. However, the absorption coefficient relates closely to its molecular properties which is of great medical and biological interest [106] (fig. 1.9). Therefore, attempting to uncouple the scattering and absorption coefficient is required. The combination of generating acoustic signals by the optoacoustic effect and detecting using image reconstructing methods known from sonography

has enabled scientists to access the spatial distribution of absorption maps at great penetration depths. This is only limited by scattering and the resolution defined by the acoustic properties. Spectrometers for solids and gases can easily be applied to biological and medical problems [107–109]. They provide optical contrast within intact and *in vivo* samples, more accurately and at greater depth than possible by diffuse optical imaging using a single ultrasonic detector. This way, it is not possible to provide meaningful spatial information on the source of the optoacoustic signal.

1.8 Tomographic optoacoustic imaging systems

The first use of the optoacoustic effect for *in vivo* imaging was performed by combining a pulsed laser source with a clinical ultrasound system [110]. It was intended to add optical contrast to ultrasonic images. This is a viable method to allow locating and measuring the oxygenation of large blood vessels. However, this method falls short of the resolution provided by reconstructing the raw data into images where the distortions of time-of-flight offsets of the individual transducers have been corrected [111, 112].

Using transducers in multiple positions, the time-of-flight of the ultrasound between an optoacoustic source and each detector is different. This can be corrected by reconstruction to generate highly resolving images, limited only by the acoustic wavelength and the detection geometry (sec. 1.5) [114, 115]. Utilizing excitation wavelengths in the NIR allows for deep tissue penetration. Due to attenuation, the acoustic frequencies used for whole body imaging of small animals are usually below 10 MHz. This defines the resolution of such systems to be in the order of 50–200 µm [116]. An example for the potential of optoacoustic tomography can be seen in figure 1.18. The measurement using multiple transducers can be done sequentially by scanning [116, 117] or in parallel [118]. Using a tunable laser source, as provided by optical parametric oscillators, multispectral imaging is feasible. Multispectral optoacoustic tomography has proven to be an invaluable tool for small animal studies. Medical applications are currently under consideration [119, 120]. It is the first modality that allows to monitor oxygenation levels, anatomical features and fluorescence agents. An example how fluorescence agents can be detected *in vivo* is shown in figure 1.19. Commercially available systems are used for biological research throughout the world.
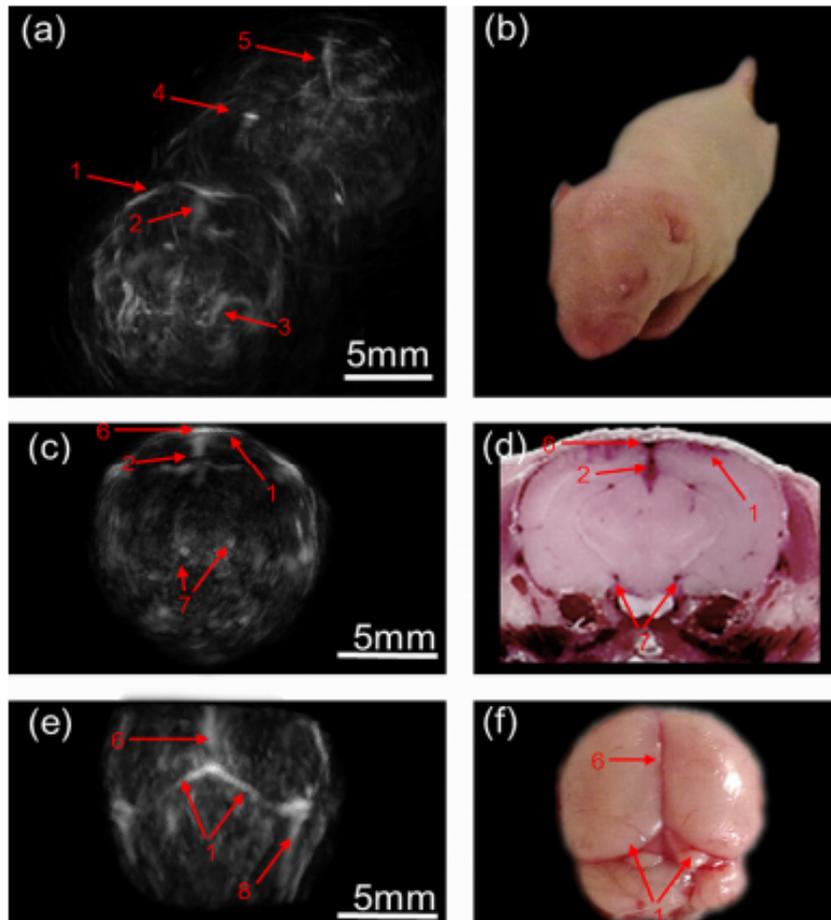
Figure 1.18: **Reconstructed image of baby mouse using optoacoustic tomography [113].** a: Maximum intensity projection of vasculature. b: Photographic image of specimen. c: Maximum intensity projection over $1\,cm$ region of mouse brain. d: Cryoslice of the same region. e: Maximum intensity projection as shown in c: from the top. f: Photograph of an excised mouse brain.
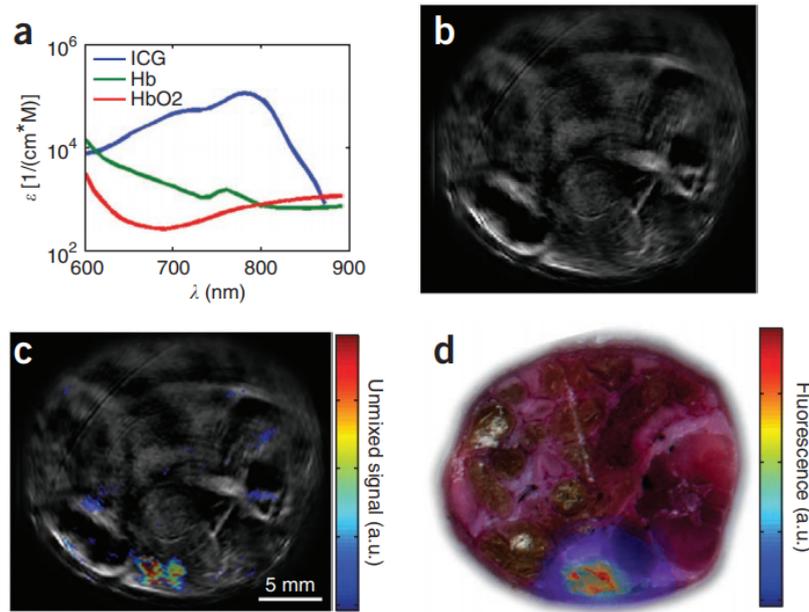
Figure 1.19: **Visualization of fluorescent agent in living mouse using multi-spectral optoacoustic tomography (MSOT) [118].** (a) Extinction coefficient of indocyanine green (ICG) in water, oxygenated and deoxygenated hemoglobin. (b) Maximum intensity projection of reconstructed image of mouse of mouse at 780 nm. (c) Superposition of the spectral unmixed ICG component and the image shown in (b). (d) Superposition of the epifluorescence image with a color photograph of the cryoslice at a corresponding height.

1.9 Optical resolution optoacoustic systems

An alternative modality of optoacoustic imaging is based on augmentation of conventional optical microscopy, where penetration depth is limited by the strong scattering of visible and NIR light in biological tissue. Methods to increase the penetration depth have been developed [121, 122]. However, they are often limited by still unsatisfactory penetration depth or require labels such as fluorescent agents to be added for contrast. Optoacoustic microscopy provides high penetration depth to visualize intrinsic contrast of biological tissue at optical microscopy resolution [123–125]. It can be combined with other microscopic imaging modalities to provide multimodal, simultaneous measurements [126, 127]. The performance is illustrated in figure 1.20, were the microvasculature in the ear of a mouse is visualized at a high resolution over a large field of view.
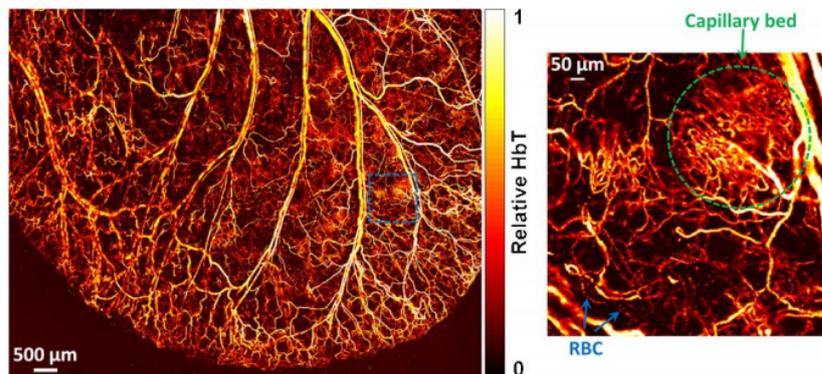

Figure 1.20: **Optoacoustic microscopy of mouse ear [128].** Optical-resolution optoacoustic microscopy image of hemoglobin concentration in the ear of a living mouse. As hemoglobin is located inside the vessels, the vascular anatomy is visible. The blue insert shows a densely packed capillary bed and individual red blood cells traveling along a capillary.

1.10 Acoustic resolution optoacoustic systems

Optoacoustic tomography allows in depth optical absorption measurements by sacrificing resolution and limiting itself to the NIR spectrum. Optoacoustic microscopy on the other hand provides extremely high resolving images, but is limited to very narrow penetration depth. Commercially, transducers with suitable sensitivity in the region beyond 100 MHz are available. Theoretically, assuming an NA of 1, resolutions down to 10 µm are achievable, which is more than one order of magnitude higher than possible in optoacoustic tomography (eq. 1.19). While this does not allow intra-cellular imaging as presented by optoacoustic microscopy, single-cell imaging is feasible. The penetration depth of very high frequencies in biological tissue is restricted (fig. 1.8). However, the losses are acceptable up to several millimeter penetration depth. In this case, it is also possible to use highly scattering visible light for excitation, in which the optical contrast is higher

than in the NIR region. In addition, when deploying a raster-scanning method, where the transducer is moved above the sample, very large volumes can be easily scanned. This allows to generate three dimensional, high resolving images of optical absorption in the visible range. This method is known as *optoacoustic mesoscopy*. An example of imaging the morphology of the vasculature around a subcutaneous tumor is shown in figure 1.21.
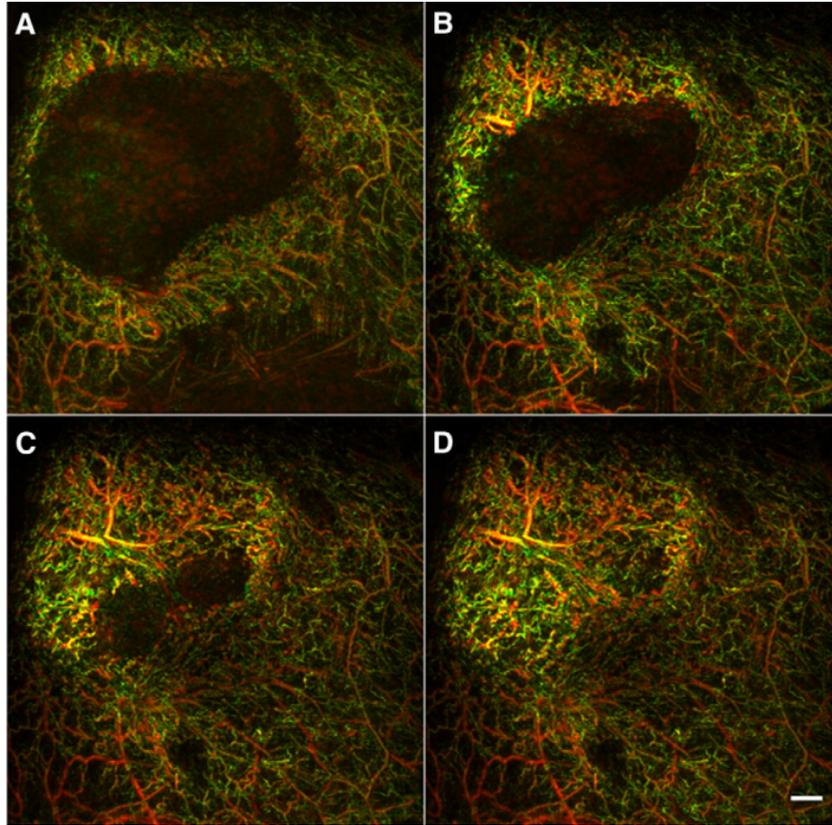

Figure 1.21: **Visualization of melanoma tumor cells subcutaneously injected into a Nude-Foxn1 mouse [129].** The maximum intensity projection along different depth range is shown: a: 0–930 μm. b: 0–615 μm. c: 0–390 μm. d: 0–2115 μm. Low acoustic frequencies are color coded red, high frequencies are color coded green.

Chapter 2

Theory

2.1   Theory of optoacoustic signal generation

Existing imaging modalities have been revolutionary advancements at their time. They have become standard procedures for many medical and biological questions. However, despite the progress made, all modalities suffer from their inability to provide enhanced soft tissue contrast or are unable to penetrate the tissue deeply. An important exception is MRI imaging which can be considered a hybrid modality. The penetration is performed by radio frequency radiation interacting with matter through magnetic resonance. The magnetic resonance condition is defined by the external magnetic field that provides spatial information.

Another modality that uses a different probe for excitation and detection is optoacoustic (OA) imaging. The optoacoustic effect was discovered utilizing sunlight on a deformable mirror for communication purposes [64]. The sample is exposed to electromagnetic radiation featuring energy gradients. This will give rise to small, rapid temperature increases causing an thermoelastic expansion. The expansion will propagate through the surrounding media as an ultrasonic wave [71]. Unlike optical imaging, the strength of the optoacoustic signal is only proportional to the absorption, but not to scattering. Therefore, optoacoustic imaging can provide information at depths where photons have been completely randomized. The scattering coefficient of sound can be neglected compared to that of light. Therefore, the resulting acoustic wave of an optoacoustic signal is virtually unaffected by scattering. This allows optoacoustic to retrieve optical information at high resolution from much deeper layers than possible with other optical methods.

The principles of optoacoustics are depicted by the optoaocustic wave equation [130]:

$$\left(\nabla^2 - \frac{1}{v_s^2}\frac{d^2}{dt^2}\right) \cdot p(\vec{r}, t) = -\frac{\beta}{\kappa v_s^2}\frac{d^2 T(\vec{r}, t)}{dt^2} \tag{2.1}$$

which shares the shape of equation 1.3 with a time dependent source term on the right. The equation describes the pressure field $p(\vec{r}, t)$ as a function of the temperature rise T of the sample. The speed of sound v_s, isothermal compressibility κ and thermal expansion coefficient β are material specific parameters of the sample.

Assuming that the sample is illuminated by a light pulse of duration τ_L, the sample will absorb the irradiated energy and increase its temperature according to its heat capacity and its volume due to thermal expansion. Next, the energy will propagate to unaffected parts of the sample thermally (by heat diffusion) and mechanically (by pressure propagation). The distance travelled by the pressure wave d_p and the thermal energy d_{th} during the pulse duration is [130]:

$$d_p = \tau_L \cdot v_s \tag{2.2}$$
$$d_{th} = \sqrt{\tau_L \cdot \alpha_{th}} \tag{2.3}$$

with α_{th} being the thermal diffusivity, typically $0.1\,\mathrm{mm^2/s}$ for biological tissue and v_s being the speed of sound, which is dependent on the temperature, but is $1481\,\mathrm{m\,s^{-1}}$ at $20\,°\mathrm{C}$ and $1509\,\mathrm{m\,s^{-1}}$ at $30\,°\mathrm{C}$ for distilled water [131]. These values define the theoretical spatial resolution of an optoacoustic imaging system. Typically, the mechanical energy travels much faster than the thermal energy:

$$d_p >> d_{th} \tag{2.4}$$

defining the resolution as d_p. Hence, the optoacoustic effect can be considered an adiabatic process, called thermal confinement and allows neglecting thermal dissipation. Consequently, a relationship between the deposited laser energy H and the consequent initial temperature rise of the sample T can be defined as:

$$H(\vec{r}, t) = \rho C_v \cdot \frac{dT(\vec{r}, t)}{dt} \tag{2.5}$$

where C_v is the specific heat capacity at constant volume and ρ is the mass density. Substituting equation 2.5 into equation 2.1 results in:

$$\left(\nabla^2 - \frac{1}{v_s^2} \frac{\partial^2}{\partial t^2} \right) \cdot p(\vec{r}, t) = - \frac{\beta}{\kappa v_s^2 \rho C_v} \frac{\partial H(\vec{r}, t)}{\partial t} \tag{2.6}$$

using the identity for the isothermal compressibility:

$$\kappa = \frac{C_p}{C_v \rho v_s^2} \tag{2.7}$$

equation 2.6 can be expressed as:

$$\left(\nabla^2 - \frac{1}{v_s^2} \frac{\partial^2}{\partial t^2} \right) \cdot p(\vec{r}, t) = \frac{\beta}{C_p} \frac{\partial H(\vec{r}, t)}{\partial t} \tag{2.8}$$

alternatively, introducing the Grueneisen-Coefficient:

$$\Gamma = \beta / \kappa \rho C_V \tag{2.9}$$

equation 2.6 can be written in the more common form:

$$\boxed{\left(\nabla^2 - \frac{1}{v_s^2} \frac{\partial^2}{\partial t^2} \right) \cdot p(\vec{r}, t) = \frac{\Gamma}{v_s^2} \frac{\partial H(\vec{r}, t)}{\partial t}} \tag{2.10}$$

Equation 2.10 is an inhomogeneous wave function composed of a source term (right side) and a propagation term (left side). The equation can be solved using the Green function [132]:

$$G(\vec{r} - \vec{r'}, t - t') = \frac{1}{4\pi} \frac{\delta\left(t - t' - \frac{|\vec{r} - \vec{r'}|}{v_s}\right)}{|\vec{r} - \vec{r'}|} \tag{2.11}$$

and can be used to formulate the following solution to equation 2.6:

$$p(\vec{r}, t) = -\frac{1}{4\pi} \int_V \int_t G(\vec{r} - \vec{r'}, t - t') \cdot \frac{\Gamma}{v_s^2} \frac{\partial H(\vec{r'}, t')}{\partial t} dr'^3 dt'$$

$$p(\vec{r}, t) = \frac{\Gamma}{4\pi v_s^2} \cdot \frac{\partial}{\partial t} \int_V \frac{H(\vec{r'}, t')}{|r - r'|} \underbrace{\left. \delta\left(t - t' - \frac{|\vec{r} - \vec{r'}|}{v_s}\right)\right|_{t' = t - \frac{|r - r'|}{v_s}}}_{=1} dr'^3$$

$$p(\vec{r}, t) = \frac{\Gamma}{4\pi v_s^2} \cdot \frac{\partial}{\partial t} \int_V \frac{H(\vec{r'}, t')}{|r - r'|} \Bigg|_{t' = t - \frac{|r - r'|}{v_s}} dr'^3 \tag{2.12}$$

The expression in the Kronecker-Delta yielding $= 1$ in equation 2.12 indicates that one must integrate the pressure field over a closed surface surrounding the volume of interest. Assuming the heating only takes place at one particular point in space (single point source), the heating function can be simplified as:

$$H(\vec{r}, t) = H_t(t) \cdot H_{\vec{r}}(\vec{r}) = H_t(t) \cdot \delta(\vec{r} - \vec{r_0}) \tag{2.13}$$

which can be substituted into equation 2.12:

$$p(\vec{r}, t) = \frac{\Gamma}{4\pi v_s^2} \cdot \frac{\partial}{\partial t} \int_V H_t\left(t - \frac{|r - r'|}{v_s}\right) \cdot \frac{\delta(\vec{r'} - \vec{r_0})}{|r - r'|} dr'^3$$

$$p(\vec{r}, t) = \frac{\Gamma}{4\pi v_s^2 \cdot |\vec{r} - \vec{r_0}|} \cdot \frac{\partial}{\partial t} H_t\left(t - \frac{|r - \vec{r_0}|}{v_s}\right) \tag{2.14}$$

The optoacoustic pressure field caused by a point source is a spherical wave originating from the position of the point source. The shape of the wave front is the first order time derivative of the heating function. Therefore, a higher rate of change of the heating function will yield a stronger optoacoustic signal. Assuming $H_t(t)$ to be a Gaussian shaped pulse:

$$H_t(t) = H_0 \cdot e^{-\left(\frac{t - t_0}{\tau_L}\right)^2} \tag{2.15}$$

equation 2.12 becomes:

$$p(\vec{r}, t) = H_0 \frac{\Gamma}{4\pi v_s^2} \cdot \frac{2 \cdot \left(t - t_0 - \frac{|r - r_0|}{v_s}\right)}{\tau_L^2} \cdot e^{-\left(\frac{t - t_0 - \frac{|r - r_0|}{v_s}}{\tau_L}\right)^2} \tag{2.16}$$

which illustrates that the pressure intensity is a function of the inverse of the pulse duration squared.

2.2 Frequency content of optoacoustic signals

When considering the frequency contents of equation 2.14, one finds:

$$p(\vec{r}, \omega) = |\mathcal{F}(p(\vec{r}, t))| = \frac{\Gamma}{4\pi v_s^2 \cdot |\vec{r} - \vec{r}_0|} \cdot \left| \mathcal{F}\left(\frac{\partial}{\partial t} H_t \left(t - \frac{|r - \vec{r}_0|}{v_s} \right) \right) \right|$$

$$p(\vec{r}, \omega) = \omega \cdot \frac{\Gamma}{4\pi v_s^2 \cdot |\vec{r} - \vec{r}_0|} \cdot \mathcal{F}\left(H_t \left(t - \frac{|r - \vec{r}_0|}{v_s} \right) \right) \quad (2.17)$$

the frequency content of the pressure field corresponds to the time derivative of the heating function. Assuming a Gaussian shape for the heating function by inserting equation 2.15 into equation 2.17:

$$p(\vec{r}, \omega) = \omega \cdot \frac{H_0 \cdot \Gamma}{4\pi v_s^2 \cdot |\vec{r} - \vec{r}_0|} \cdot \mathcal{F}\left(e^{-\left(\frac{t - t_0}{\tau_L} \right)^2} \right)$$

$$p(\vec{r}, \omega) = \omega \frac{H_0 \cdot \Gamma}{4\pi v_s^2 \cdot |\vec{r} - \vec{r}_0|} \cdot \sqrt{\frac{\pi}{\tau_L}} \cdot e^{-\frac{\tau_L^2 \omega^2}{2}} \quad (2.18)$$

According to equation 2.3, the pulse duration defines the achievable resolution. This can also be explained in the frequency domain, since shorter pulses create higher frequencies, which correspond to shorter wavelengths. A single point source will produce an optoacoustic signal (eq. 2.18). However, a spatial distributed absorber will generate a more complex optoacoustic response. As already implied by the Green function (eq. 2.11), optoacoustics obeys the Huygens principle, in which any arbitrary wave front can be considered as the superposition of individual point sources. Consequently any distribution of absorbers giving rise to an optoacoustic signal may be considered as a distribution of individual point sources. Thus, the resulting optoacoustic signal measured at position $\vec{r}$ at the time t can be calculated by convoluting equation 2.14 with the spatial distribution of the absorbers. This will result in destructive interference between the signal emitted from each point emitter, whose wavelength is comparable to the dimension of the distribution. In consequence, the optoacoustic signal of spatially distributed absorbers will have a lower frequency content compared to a point source.

In many cases, the spectral content of equation 2.3 is much higher than the effect of the convolution of equation 2.14 with the spatial distribution, since a short pulse duration is chosen not only to achieve high resolution, but to maximize signal generation efficiency. Typical duration of laser pulses is between 1–10 ns. Assuming that the speed of sound is 1500 m/s, equation 2.3 concludes that the theoretical resolution is 1.5–15.0 µm, which is smaller than the size of most visualized structures.

2.3 Reconstruction in optoacoustic imaging

For some clinical applications reconstruction may not be necessary. While the acquired data does not precisely reflect the actual spatial absorption distribution,

the relation may be sufficient for conclusions to be drawn [133–135]. In some optoacoustic modalities such as optoacousic microscopy, the spatial information is provided by other means, making reconstruction superfluous [125, 136]. In other cases, concepts from acoustic resolving scanning microscopy can be adapted for high resolution optoacoustic imaging, as both rely on focusing transducers [67, 137]. This method will provide high resolution image in the focal plane of the transducer. Moving away from it will diminish the resolution depending on the numerical aperture of the transducer. If a homogeneous resolution over a large field of view (along the scanning direction) and large depth of field (perpendicular to the scanning direction) is desired, employing reconstruction algorithms is necessary. However, analytic solutions to the inversion of equation 2.12 are generally not available. Therefore, numerical approaches have been developed.

Filtered back-projection

The initial pressure at the source of the optoacoustic wave $p_0(r)$ can be found by mathematically inverting the equation 2.12 [114]:

$$p_0(\vec{r}) = \int_{\Omega_0} \frac{d\Omega}{\Omega_0} \left(2 \cdot p(\vec{r_0}, t) - 2 \cdot t \frac{\partial p(\vec{r_0}, t)}{\partial t} \right)\Big|_{v_s \cdot t = r - r_0} \tag{2.19}$$

which expresses the initial pressure as a function of pressure $p(r_0, t)$ detected at the detector position r_0 over time t. However, measuring the sound field at a single point r_0 does not allow the initial pressure distribution to be calculated. r_0 must be integrated over a closed surface surrounding $p_0(r)$. Depending on the geometry, analytical solutions for the integral $\int_{\Omega_0} \frac{d\Omega}{\Omega_0}$ are available. Solutions for cylindrical and spherical geometries are known, which are taking into account the solid angle element $d\Omega$ [114]. In experimental practice, a transducer array or scanning a single transducer would be used to acquire $p(r_0, t)$ at as many positions on Ω as possible. Next, the acquired signal at each position $p(r_0, t)$ will be used to calculate the term in brackets in 2.19 and projecting it over the angular element $d\Omega$. The process is repeated for all acquired projections.

It is neither possible to sample Ω with infinite resolution, nor over an entirely closed surface. Therefore, the achieved resolution will fall behind the theoretical limit. In addition, artefacts will be introduced due to the non-ideal detection geometry.

Model-based reconstruction

Equation 2.12 can be written in sum notation [115]:

$$p(\vec{r}, t) = \frac{\Gamma}{4\pi v_s^2} \cdot \sum_i^N \frac{\partial/\partial t H(\vec{r_i}, t)}{|\vec{r} - \vec{r_i}|} \Delta r_i^3 \tag{2.20}$$

which can be expressed in the form of matrix multiplication:

$$p(\vec{r}, t) = A_{ji} \cdot \frac{\partial}{\partial t} H(\vec{r_j}, t) \Delta r_i^3, \quad A_{ji} = \frac{\Gamma}{4\pi v_s^2} \cdot \frac{1}{|\vec{r_j} - \vec{r_i}|} \tag{2.21}$$

Hence, the inverse of the matrix A_{ji} can be used to find an expression of $\frac{\partial}{\partial t}H(\vec{r_k},t)$ using the acquired pressure field $p(\vec{r},t)$.

$$A_{ji}^{-1} \cdot p(\vec{r},t) = \frac{\partial}{\partial t}H(\vec{r_k},t) \tag{2.22}$$

However, the matrix A_{ji}^{-1} does not exist in most cases, as A_{ji} is commonly not invertible. However, a solution can be obtained by minimizing the difference between $p(\vec{r},t)$ and $A_{ji} \cdot \frac{\partial}{\partial t}H$

$$p(\vec{r},t) - A_{ji} \cdot \frac{\partial}{\partial t}H(\vec{r_k},t) \to 0 \tag{2.23}$$

This can be done by minimizing the norm of the above expression using a LSQR algorithm:

$$\frac{\partial}{\partial t}H = argmin||p(\vec{r},t) - A_{ji}|| \tag{2.24}$$

This approach is advantageous over back-projection because it allows non-ideal reconstruction geometries to be taken into account [138]. Typically, additional weighting factors are added to equation 2.24 which compensate for the effects of non-closed detector surfaces and finite spatial resolution of acoustic detectors. Images generated by model based algorithms commonly feature a superior image quality and less artefacts than by filtered back projection.

In contrast, model based reconstruction is extremely computationally and memory expensive [139]. The size of matrix A_{ij} corresponds to the number of acquired positions along the detection surfaces by the number of voxels to be reconstructed, easily exceeding several gigabyte. Moreover, solving equation 2.24 is an iterative process which may not converge for many iterations. Therefore, executing the optimization presents a significant computational challenge and may be difficult to perform in real-time [140].

2.4 Multispectral optoacoustic imaging

The energy deposition $H(\vec{r_0},t)$ corresponds to the laser fluence $I(\vec{r_0},t)$ and the samples absorption coefficient $\mu_a(\lambda)$ at the wavelength of the excitation laser. The absorption coefficient can also be written as the molar absorption times the concentration [141]:

$$\mu_a(\lambda) = \epsilon(\lambda) \cdot c(\vec{r_0}) \tag{2.25}$$

where $\epsilon(\lambda)$ is the wavelength-dependent molar absorption coefficient and c is the molar concentration in the sample. The absorption spectrum of various chromophores can vary strongly with the wavelength (fig. 1.9). Furthermore, in biological samples more than one chromophore can be present at a given position $\vec{r_0}$. This problem can be addressed by measuring the optoacoustic response of the sample at a multitude of excitation wavelengths. If the wavelengths are chosen in a way that the absorption of the various chromophores differs significantly, it is possible to determine the concentration of each individual chromophore

through "multispectral unmixing". Assuming that a sample consists of N different chromophores, the optoacoustic response at a given wavelength is:

$$p(\vec{r}, t, \lambda) \propto H(\vec{r_0}, t, \lambda) \cdot \sum_i \epsilon_i(\lambda) \cdot c_i(\vec{r_0}) \qquad (2.26)$$

when repeating the measurement for M different wavelengths, these measurements can be defined as:

$$p(\lambda_1) = H(\vec{r_0}, t, \lambda_1) \cdot \sum_i \epsilon_i(\lambda_1) \cdot c_i(\vec{r_0}) \qquad (2.27)$$

$$p(\lambda_2) = H(\vec{r_0}, t, \lambda_2) \cdot \sum_i \epsilon_i(\lambda_2) \cdot c_i(\vec{r_0}) \qquad (2.28)$$

$$... \qquad (2.29)$$

$$p(\lambda_M) = H(\vec{r_0}, t, \lambda_M) \cdot \sum_i \epsilon_i(\lambda_M) \cdot c_i(\vec{r_0}) \qquad (2.30)$$

$$(2.31)$$

this system of coupled linear equations can be changed to:

$$\begin{pmatrix} p(\lambda_1) \\ p_(\lambda_2) \\ ... \\ p_(\lambda_N) \end{pmatrix} = \underbrace{\begin{pmatrix} H(\lambda_1) \cdot \epsilon_1 & H(\lambda_1) \cdot \epsilon_2 & .. & H(\lambda_1) \cdot \epsilon_M \\ H(\lambda_2) \cdot \epsilon_1 & H(\lambda_2) \cdot \epsilon_2 & .. & H(\lambda_2) \cdot \epsilon_M \\ ... & ... & ... & ... \\ H(\lambda_N) \cdot \epsilon_1 & H(\lambda_N) \cdot \epsilon_2 & .. & H(\lambda_N) \cdot \epsilon_M \end{pmatrix}}_{=A_{NM}} \cdot \begin{pmatrix} c_1(\vec{r_0}) \\ c_2(\vec{r_0}) \\ ... \\ c_M(\vec{r_0}) \end{pmatrix} \qquad (2.32)$$

$$p(\lambda_N) = A_{NM} \cdot c_M(\vec{r_0}) \qquad (2.33)$$

This linear system can be inverted when A_{NM}^{-1} exists. Thus, the concentration of each absorber is simply given by:

$$c_M(\vec{r_0}) = A_{NM}^{-1} \cdot p(\lambda_j) \qquad (2.34)$$

The outcome strongly depends on the signal quality of $p(\lambda)$ and how linear independent the vectors making up A_{NM} i.e. how well conditioned A_{NM} is. If A_{NM}^{-1} does not exist an approximate solution to equation 2.32 can be found by using a minimization approach introduced in section 2.3, which leads to the solution [142]:

$$c_M(\vec{r_0}) = argmin||p(\lambda_N) - A_{NM}|| \qquad (2.35)$$

2.5 Introduction to frequency domain optoacoustics (FDOA)

Powerful light sources for optoacoustic imaging in the time domain are available, yet Q-switched lasers suffer from very limited wavelength availability (sec. 1.4). In addition, they feature a large form factor and require relatively high investments. As they are not tunable, multispectral imaging requires deploying multiple

Q-switched lasers at different wavelengths, increasing cost and complexity proportionally. Alternatively, when using frequency doubling the pump wavelength can be used to allow imaging at both wavelengths [143]. Microchip lasers show potential to significantly reduce the complexity of Q-switched systems [144, 145]. These have become available at visible wavelength which makes them attractive for medical and biological applications [146]. Nevertheless, the wavelengths are still limited to a number of specific values and they still provide a financial investment unattractive for many applications. OPOs can be used to address the limited wavelength availability of Q-switched lasers. While providing powerful, short laser pulses at nearly arbitrary wavelengths in the visible and infra-red range, Q-switched OPOs suffer from a number of shortcomings [147]. They are based on spontaneous parametric down conversion, which is a nonlinear effect. Effective operation requires accurate phase-matching between the OPO crystal and the pump laser. This makes such systems complicated to build and maintain. In addition, optoacoustic imaging typically requires pulse energy in the µJ to mJ range. While these systems exist, their repetition rate is limited to several 100 Hz. When performing multispectral optoacoustic imaging using OPOs, the wavelength is changed from pulse to pulse. Hence, the number of pulses needed for a single multispectral measurement corresponds to the number of wavelengths to be measured. Together with the limited repetition rate, this increases the measurement time to unacceptable levels for most medical applications [148].

More flexible semiconductor based light sources such as light emitting devices or laser diodes have been considered for optoacoustic imaging, but struggle to provide sufficient pulse energy at the short durations necessary for high resolution imaging. Nevertheless, semiconductor light sources can be pulsed at very high repetition rates. Therefore, coherent signal averaging is a possibility to increase the signal-to-noise (SNR) ratio, increasing the acquisition time significantly [149–155]. Multispectral imaging using semiconductor light sources is possible by combining several light sources, with the desired wavelength and acquire the data by time sharing [154]. Semiconductor sources are available at a much larger range of wavelengths than Q-switched lasers and are commonly much simpler and more reliable [156–158]. However, the acquisition time will also increase proportional to the number of wavelengths acquired. Moreover, *in vivo* specimen do show motion during the measurement process. If the specimen moves between the acquisition of two wavelengths, this significantly decreases the multispectral performance of such systems as the acquired data is no longer comparable.

2.6 Chirped pulse frequency domain optoacoustics

The problem of generating short pulses with continuous wave sources with low instantaneous power is a problem shared by many other fields, including radar, sonar and lidar [159–161]. To overcome the limited pulse energy of such sources, pulse compression has been suggested [162]. Using a single pulse in the time domain

as the interrogation function provides access to the impulse response function of the system, as the initial impulse only occupies a small region in the time domain. Therefore, the region not occupied by the initial pulse is available for response function of the system, which in this case is the optoacoustic signal. In other words, the pulse is a *sparse* function in the time domain. The measured total response function $x(t)$ is the convolution between the actual system response $y(t)$ (which carries the desired information) and the input pulse $g(t)$:

$$x(t) = y(t) * g(t) \tag{2.36}$$

If $g(t)$ is a short pulse, it can be approximated as a dirac-function $g(t) = \delta(t - t_0)$, equation 2.36 becomes:

$$x(t) = y(t) * g(t) = y(t) * \delta(t - t_0) = y(t) \tag{2.37}$$

therefore, $y(t)$ matches the measured function $x(t)$. Pulse compression is based on the concept that a waveform $h(t)$ exists which does not satisfy the condition 2.37, but its auto-correlation does:

$$\delta(t - t_0) = h(t) * h(t)^* \tag{2.38}$$

If a function $h(t)$ fulfilling condition 2.38 is used to interrogate a system with the impulse response $y(t)$:

$$x(t) = y(t) * h(t) \tag{2.39}$$
$$x(t) * h(t)^* = y(t) * \underbrace{h(t) * h(t)^*}_{=\delta(t-t_0)} \tag{2.40}$$
$$x(t) * h(t)^* = y(t) \tag{2.41}$$

The cross correlation between the measured response $x(t)$ and the interrogation function $h(t)$ provides the systems impulse response $y(t)$, just as when using a single pulse $h(t)$ as shown in equation 2.38. If $h(t)$ is a continuous function, it can easily be modulated by continuous wave light sources such as laser diodes or other light emitting devices. A number of functions exist that satisfy condition 2.37. An important example is the chirp function:

$$h(t) = \sin\left(2\pi\left(f_0 + \frac{k}{2}t\right)t\right) \tag{2.42}$$

where k is the chirp constant, defining how fast the frequency varies over time. The larger the bandwidth is covered by $h(t)$, the better the requirement of equation 2.38 is fulfilled [163]. Typically, the chirp bandwidth will be chosen to match the transducer bandwidth. Figure 2.1a shows a chirped pulse with $f_0 = 100\,\text{kHz}$ and $k = 1\,\text{MHz/µs}$. The cross correlation of the pulse is shown in figure 2.1b and exhibits a dirac-function like behaviour. Figure 2.1c simulates an optoacoustic measurement by convolution of the chirped pulse with an optoacoustic point source with and without noise. After undergoing cross correlation, the recovered signal features a low noise level (fig. 2.1d). However, due to the limited bandwidth,
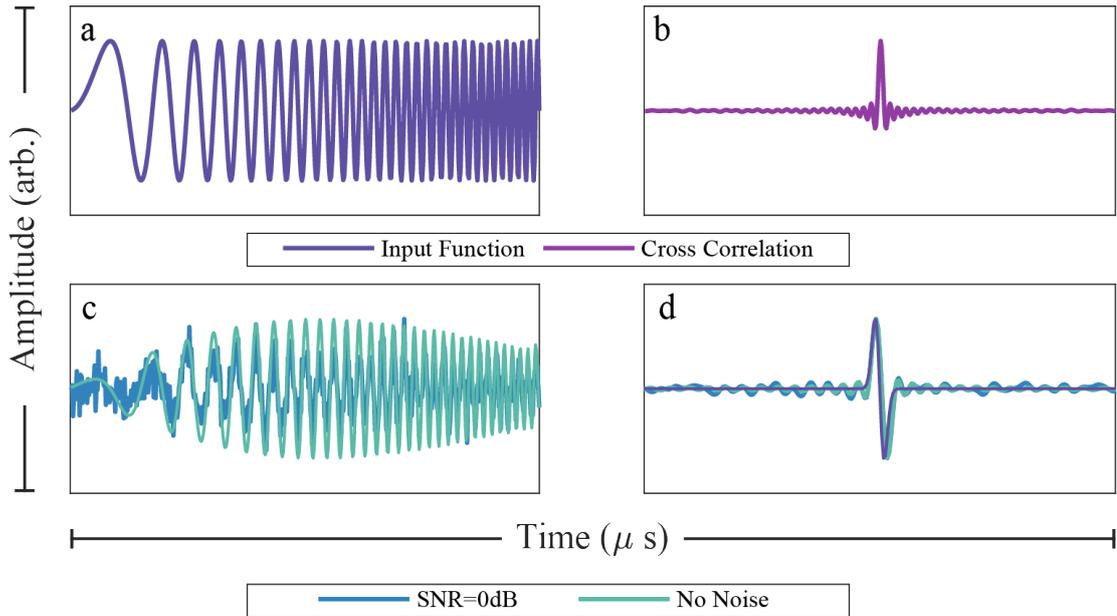
Figure 2.1: **Concept of pulse compression in optoacoustics.** a: Chirped pulse with 2.5 µs duration, $f_0 = 100\,\text{kHz}$ and $k = 1\,\text{MHz/µs}$. b: Auto correlation of chirped pulse shows a dirac-function like behaviour. c: Convolution of chirped pulse with simulated optoacoustic point source simulating optoacoustic response of chirped pulse. Simulation done assuming no noise and $SNR = 0\,\text{dB}$. d: Cross correlation of simulated optoacoustic signal with chirped pulse for both discussed cases. Original signal from point source added for reference.

equation 2.42 does not precisely match a dirac-function. Therefore, some artefacts in the recovered function remain, even when no noise is present. A major drawback of the discussed method is, that it does not achieve the same SNR as provided by pulsed excitations (eq. 2.14). The optoacoustic signal strength is proportional to the rate of change of the heating function and the peak energy, not its total energy content. Therefore, if a chirped pulse contains the same energy as a single pulse of the same bandwidth, the SNR generated by the single pulse will be higher, as the rate of change of the heating function is higher [164]. Nevertheless, pulse compression demonstrated that *in vivo* optoacoustic imaging of tissue is possible with continuous wave sources [165–167].

2.7 Single wave frequency domain optoacoustics (SWFD)

Section 1.4 and 1.6 discussed how optoacoustic signals can be detected with lock-in detection when they are modulated to a single frequency. Before Q-switched lasers became available, this was the only feasible method to perform optoacoustic measurements. Conventionally, this was done using continuous wave light sources combined with a mechanical beam chopper. Using continuous wave laser diodes, it

is possible to modulate the laser output waveform to nearly arbitrary waveforms including single frequencies. However, as discussed in section 2.1, this will yield a lower SNR compared to single pulses containing the same energy and frequency content. This decrease in SNR can partially be compensated by the high noise rejection provided by lock-in detection [102, 103]. Inserting the interrogation function $g(t) = I_0 \cdot \sin(\omega_0 t)$ into equation 2.17 yields:

$$
p(\omega) = I_0 \cdot y(t) * \sin(\omega_0 t) \tag{2.43}
$$

$$
p(\omega) = \frac{I_0 \cdot \omega}{2\pi} \cdot \underbrace{\mathcal{F}(y)(\omega_0)}_{=1} \cdot \delta(\omega - \omega_0) \tag{2.44}
$$

where $\mathcal{F}(y)(\omega_0)$ is the Fourier transform of $y(t)$ evaluated at ω_0. The optoacoustic signal resulting from single wave excitation only features one single frequency component. While this opens up the concept of lock-in detection for optoacoustic applications, it also highlights how single wave excitation does not provide any spatial resolution (sec. 2.2), since the bandwidth of a single frequency is close to zero. Therefore, single wave frequency domain (SWFD) optoacoustics is unsuitable for optoacoustic tomography. Hence, the usability for biological or medical applications is limited. However, optoacoustic microscopy provides spatial information by optical focusing. Consequently, spatial information from the optoacoustic signal is not required. This has lead to the development of a number of SWFD optoaocoustic microscopy systems. These also benefit from the very high optical flux at the focus of the system. This increases the SNR to sufficient levels despite the low signal generation efficiency [168–170].

The fundamental concept of SWFD optoacoustics is explained in figure 2.2a, which presents a sine wave at $f = 10\,\text{MHz}$ with and without noise. The frequency spectrum of the waves is shown in figure 2.2b with visible frequency components. These frequency components are extracted in figure 2.2c. The inverse Fourier transform of these components is shown in figure 2.2d, which presents the same waveform seen in figure 2.2a but with strongly reduced noise.

In single wave applications, lock-in detection can be used to detect single frequencies in noisy signals. The fundamental motivation for developing lock-in detectors was to improve narrow band filters at high frequencies, since available filters allow significant noise to pass in frequencies close to the signals frequency. Utilizing lock-in detection, the signal $f_{sig} = A_{sig} \cdot \sin(\omega_0 \cdot t + \phi)$ is multiplied by a reference signal $f_{ref} = A_{ref} \cdot \sin(\omega_0 \cdot t)$:

$$
\begin{aligned}
f_{lock-in} &= f_{sig} \cdot f_{ref} \\
f_{lock-in} &= A_{sig} \cdot \sin(\omega_0 \cdot t + \phi) \cdot A_{ref} \cdot \sin(\omega_0 \cdot t) \\
f_{lock-in} &= \frac{A_{sig} \cdot A_{ref}}{2} \cdot \cos((\omega_0 + \omega_0) \cdot t + \phi) \\
&+ \frac{A_{sig} \cdot A_{ref}}{2} \cdot \cos((\omega_0 - \omega_0) \cdot t + \phi)
\end{aligned}
\tag{2.45}
$$
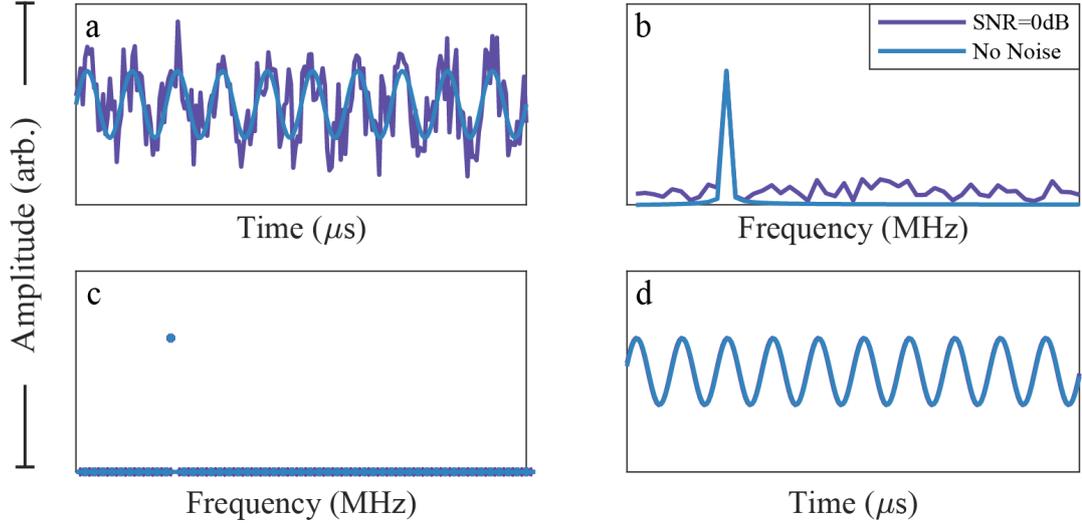
Figure 2.2: **Concept of SWFD optoacoustics.** a: Simulated response of point source illuminated with sinusoidal waveform at $10\,\mathrm{MHz}$ with additive white Gaussian noise at SNR=$0\,\mathrm{dB}$ (violet). Same signal with no noise added for reference (blue). b: Fourier transform of data presented in a. c: Frequency components of data shown in b. d: Inverse Fourier transform of extracted data shown in c. Most noise has been rejected.

Assuming $\omega_{sig} = \omega_{ref} = \omega_0$:

$$f_{lock-in} \quad = \quad \frac{A_{sig} \cdot A_{ref}}{2} \cdot \cos(\phi) + \frac{A_{sig} \cdot A_{ref}}{2} \cdot \cos(2 \cdot \omega_0 \cdot t + \phi) \quad (2.46)$$

This results in two new frequency components located at $f = 2 \cdot \omega_0$ and at $f = 0$. A low pass filter is used to remove the higher frequency component. Hence, only the component at $f = 0$ pass which carries the same information (amplitude A_{sig} and phase ϕ) as the original input waveform. The low signal strength during excitation can be partially compensated by the very low noise detection [171, 172]. The concept is highlighted in figure 2.3a which shows a sine waves without noise and with noise. The resulting Fourier transform is seen in figure 2.3b, together with a bandpass filter to remove noise present at all other frequencies. Due to the finite bandwidth of the filter, some noise passes nevertheless. Therefore, the inverse Fourier transformed signal does not match the noiseless signal precisely (fig. 2.3c). If the two signals are subjected to lock-in detection (fig. 2.3d) noise has a much lower effect on the resulting signal (fig. 2.3e).
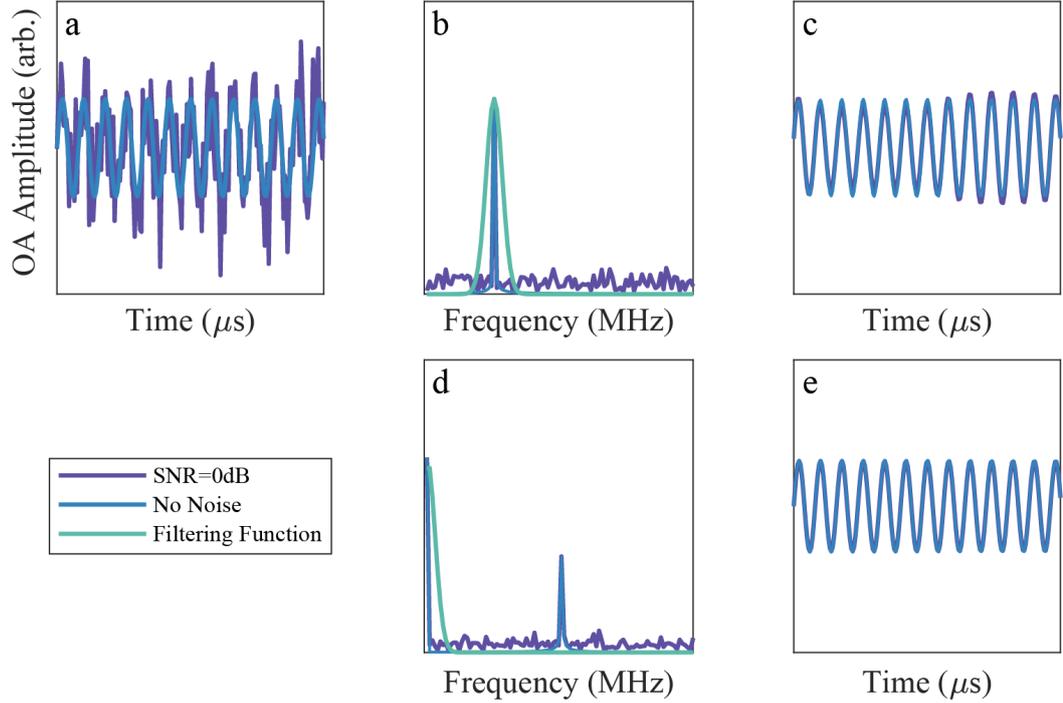
Figure 2.3: **Principle of lock-in detection in SWFD optoacoustics.** a: Simulated optoacoustic response of point source illuminated with sinusoidal waveform with 12.5 MHz and additive white Gaussian noise of SNR=0 dB (violet) and without noise (blue). b: Fourier transformation of data shown in a, superimposed with a filter-function centred around $f = 12.5$ MHz and a FWHM bandwidth of 5 MHz (green). c: Inverse Fourier transform of data shown after filtering shown in b. d: Fourier transformation of data shown in a, after being demodulated with a reference signal of $f_{ref} = 12.5$ MHz. The same filter function as in b is shown, but this time it is centred around $f = 0$ MHz. e: Inverse Fourier transform of data shown in d.

2.8 Single pulse and pulse wave time domain (SPTD, PWTD)

In single pulse time domain (SPTD) optoacoustics, a single pulse of light is used to interrogate the sample, as used in most existing systems. The sampling rate and the speed of sound v_s define the limit of the axial resolution due to the acquisition system:

$$\delta x_{TD} = v_s/F_s \tag{2.47}$$

where v_s is the speed of sound and F_s is the sampling rate, which must exceed the value given by equation 2.3 by at least a factor of two to avoid spatial aliasing [173]. The depth of field defined in time domain DoF_{TD} is given by:

$$DoF_{TD} = t_{int} \cdot v_s \tag{2.48}$$

with t_{int} being the integration time over which the signal is acquired. This allows to define the total number of data points acquired as:

$$N_t = \frac{DoF_{TD}}{\delta x_{TD}} = \frac{t_{int} \cdot v_s}{v_s/F_s} = t_{int} \cdot F_s \qquad (2.49)$$

For single pulse time domain (SPTD) optoacoustics, the data acquisition system is usually triggered by the laser pulse and starts acquiring for a predefined time corresponding to the expected depth of field. This typically is several cm in tomographic systems and several mm in mesoscopic systems. Thus, the acquisition time t_{int} is in the range of 10–100 µs.

Multiple pulses acquired from a pulse train can be averaged coherently in time domain. In this case, as soon as the acquisition for one pulse is completed, the next pulse is emitted. The data acquisition is not triggered by each individual pulse, but continuously acquires the desired number of pulses. Pulse wave time domain (PWTD) optoacoustics shares similarities with classical single pulse time domain (SPTD) optoacoustics. However, PWTD can be conducted using the same experimental setup as pulse wave frequency domain optoacoustics. Depending on the pulse energy and the type of sample, the number of pulses acquired N_{avg} is typically in the range of 10-1000. This will increase the acquisition time proportional to the number of pulses averaged:

$$t_{tot} = t_{int} \cdot N_{avg} \qquad (2.50)$$

2.9 Pulse wave frequency domain optoacoustics (PWFD)

To this point, time domain optoacoustics using a single pulse or a pulse wave for excitation and frequency domain optoacoustics using a single wave have been considered. Both modalities have their distinct advantages and disadvantages. A hybrid modality between the two is *pulse wave frequency domain* (PWFD) optoacoustics. It is based on an excitation signal consisting of a wave of individual pulses, at a fixed pulse duration τ_p (typically several ns) and fixed repetition rate f_{rep} (typically several 100 kHz to MHz).

In the frequency domain, a pulse wave is a multitude of discrete frequency components. The spacing of these frequency components corresponds to the pulse wave repetition rate f_{rep}. The amplitude of each frequency component corresponds to the Fourier transform of a single pulse, evaluated at the corresponding frequency. In other words, the frequency components of a single pulse share the same envelope as the frequency components of a pulse wave. The bandwidth of the envelope of a pulse is proportional to the inverse of the pulse duration τ_p (sec. 2.2). To illustrate the concept of PWFD, a pulse train with $f_{rep} = 1$ MHz and $\tau_p = 20$ ns for two cases, one assuming no noise and the other assuming added white Gaussian noise are considered (fig. 2.4a). The Fourier transform of the two cases is calculated and presented together with the spectrum of a single pulse for reference (fig. 2.4b). The frequency components of the pulse train match the shape

of the single pulse (fig. 2.4c). Inverse Fourier transforming the components yields the original signal with strongly reduced noise (fig. 2.4d).
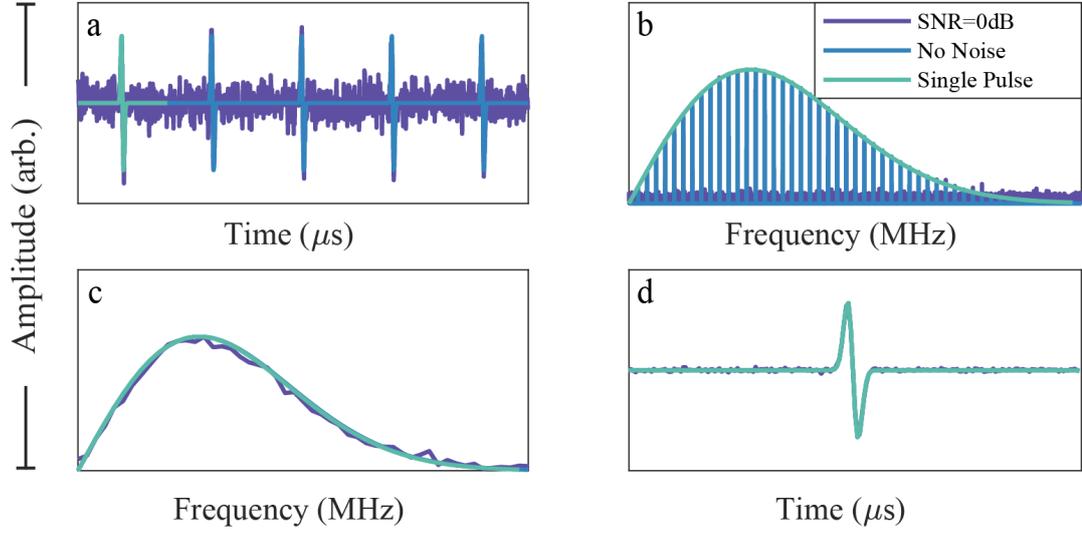

Figure 2.4: **Concept of PWFD optoacoustics.** a: response to pulse wave with pulse duration of $\tau_p = 20\,\text{ns}$, $f_{rep} = 1\,\text{MHz}$ and $SNR = 0\,\text{dB}$ (violet) and no noise (blue). Single pulse added for reference (green) b: Fourier transform of data shown in a. c: Extracted frequency components of the pulse train. d: inverse Fourier transform of data shown in c.

PWFD combines the advantages of time domain and frequency domain excitation. While the signal generation efficiency of the optoacoustic signal is as high as in pulsed excitation, single frequency components are available for lock-in detection. Hence, the detection of each frequency component can be performed over a very narrow bandwidth reducing the detection noise. Since a multitude of frequency components are acquired, spatial resolution is provided by the optoacoustic signal, unlike in single wave frequency domain (SWFD). The frequency spectrum of a pulse train will be populated by a multitude of discrete frequency components spaced f_{rep} apart. Due to the Nyquist-limit, the highest frequency component that carries meaningful information is $\frac{F_s}{2}$. Hence, the obtainable number of frequency components is:

$$N_f = \frac{F_s/2}{f_{rep}} = \frac{F_s \cdot t_{rep}}{2}, \quad f_{rep} = \frac{1}{t_{rep}} \tag{2.51}$$

When assuming continuous acquisition $f_{rep} = 1/t_{int}$ the number of samples acquired per pulse is:

$$N_p = F_s \cdot t_{rep} \tag{2.52}$$

and the ratio between N_f and N_p is:

$$\frac{N_p}{N_f} = 2 \tag{2.53}$$

Therefore, the number of samples obtainable in the time domain is twice that in the frequency domain. However, the sampling point in the frequency domain are *complex*, carrying twice the information of a real signal (amplitude *and* phase). This highlights how the information obtained in PWFD and PWTD is equivalent. The lowest frequency that can be acquired in PWFD is f_{rep}. Thus, the depth of field in PWFD is:

$$DoF_{FD} = \frac{v_s}{f_{rep}} = v_s \cdot t_{rep} \tag{2.54}$$

which matches the depth of field in PWTD (equation 2.48). In order to calculate the resolution achievable in PWFD, δx_{FD}, equation 2.47 can be arranged in the frequency domain:

$$\delta x_{FD} = \frac{DoF_{FD}}{N_f} = \frac{v_s/f_{rep}}{F_s/(2 \cdot f_{rep})} = 2 \cdot \frac{v_s}{F_s} \tag{2.55}$$

The achievable resolution under the same condition is the same for the time domain and the frequency domain pulse wave optoacoustics (since in PWFD, the acquired data points carry twice the information as in PWTD). When acquiring N_{avg} pulses, the number of frequency components N_f remains constant. However, the total number of acquired samples N_{tot} increases proportionally to the number of averages:

$$N_{tot} = \frac{F_s}{f_{rep}} \cdot N_{avg} \tag{2.56}$$

Assuming $v_s = 1500 \, \text{m/s}$, if the data is acquired at $F_S = 200 \, \text{MS/s}$ and the desired depth of field is $DoF = 6 \, \text{mm}$, the maximum repetition rate is:

$$f_{rep} = \frac{v_s}{DoF} = \frac{1500 \, \text{m/s}}{6 \, \text{mm}} = 250 \, \text{kHz} \tag{2.57}$$

which results in the number of acquired frequencies being:

$$N_f = \frac{F_s}{2 \cdot f_{rep}} = \frac{200 \, \text{MS/s}}{2 \cdot 250 \, \text{kHz}} = 400 \tag{2.58}$$

If $N_{avg} = 100$, the total number of samples acquired would be $N_f \cdot N_{avg} = 40 \cdot 10^3$

2.10 Multispectral PWFD optoacoustics (MS-PWFD)

Existing multispectral methods are based on time sharing (sec. 2.4). A laser pulse of a particular optical wavelength is used to interrogate a system, followed by a laser pulse of the next desired wavelength. This process is repeated for all wavelengths causing an increase of the measurement time proportional to the number of wavelengths used. When an optical parametric oscillator is used, the total repetition rate is limited, typically to a few $100 \, \text{Hz}$ (sec. 2.1). This puts an even more severe limit on the achievable scanning times and the number of wavelengths that can be interrogated.

PWFD optoacoustics provides a solution to this trade-off by replacing time sharing with frequency sharing. When considering the frequency spectrum of a pulse wave, the energy is concentrated into N_f discrete peaks (fig. 2.4), the number of peaks is given by equation 2.51. Since the number of sampling points is not changed by the discrete Fourier transformation, the total number of data points in the frequency domain is given N_{tot} (eq. 2.56). This means that in *single wavelength PWFD* only N_f of $N_{avg} \cdot N_f$ sampling points in the frequency spectrum are occupied by a frequency component. This helps to increase the SNR, as the noise is equally distributed over all frequency bins. Hence the information carrying bins only carry $1/N_{tot}$ of the total noise. It also means that the majority of the system bandwidth is unused. **MS-PWFD presents the possibility to populate the unused frequency bins with information from other wavelengths**. N_λ lasers at different optical wavelengths are deployed simultaneously, but at slightly different repetition rates $f_{rep,\lambda}$. The optoacoustic signal of these lasers overlaps and is detected with the same transducer. This will result in the frequency components of each laser to occupy different frequency bins. As the frequency components of each laser are multiples of $f_{rep,\lambda}$, each frequency component can be assigned to the appropriate laser. Figure 2.5a and b shows two frequency combs with slightly different repetition rates. If they illuminate the same absorber simultaneously, the resulting optoacoustic signal will overlap in the time domain (fig. 2.5c). Fourier transforming will result in distinct peaks, which can be allocated to the according laser (fig. 2.5d). Inverse Fourier transforming the extracted frequency components will recover the optoacoustic signal generated by each laser (fig. 2.5e and f).

$f_{rep,\lambda}$ must be chosen in a way that the frequency components of two lasers do not occupy the same bin in the frequency domain. When considering the limited detection bandwidth of available transducers, $f_{rep,\lambda}$ must be chosen in a way that the frequency components do not overlap within the *transducers bandwidth* which is defined by the lower and upper cut-off frequency f_1 and f_2. In practice, $f_{rep,\lambda}$ is chosen by first selecting a base frequency $f_{rep,0}$ according to equation 2.54. Next, a frequency step Δf is chosen to yield:

$$f_{rep,\lambda} = f_{rep,1} + n \cdot \Delta f, \qquad n \in [1, N_\lambda] \tag{2.59}$$

In result, the frequency components of the lasers will be $n \cdot \Delta f$ apart for the nth frequency component. In order to assign each frequency component to the appropriate laser, the space between two f components must be greater than the frequency resolution of the system, which is assumed to be $\delta f = 1/t_{int}$. From this, we can state two conditions for Δf:

1. For the first frequency component greater than f_1, Δf must be greater than δf. This ensures that the frequency components of all lasers are spaced apart far enough in order to be resolved:

$$N_{f_1} = f_1/f_{rep,0}$$
$$N_{f_1} \cdot \Delta f > 2 \cdot \delta f \tag{2.60}$$

2. For the last frequency component smaller than f_2, $n \cdot \Delta f$ must be smaller than $f_{rep,0}$. This guarantees that the frequency component with the highest
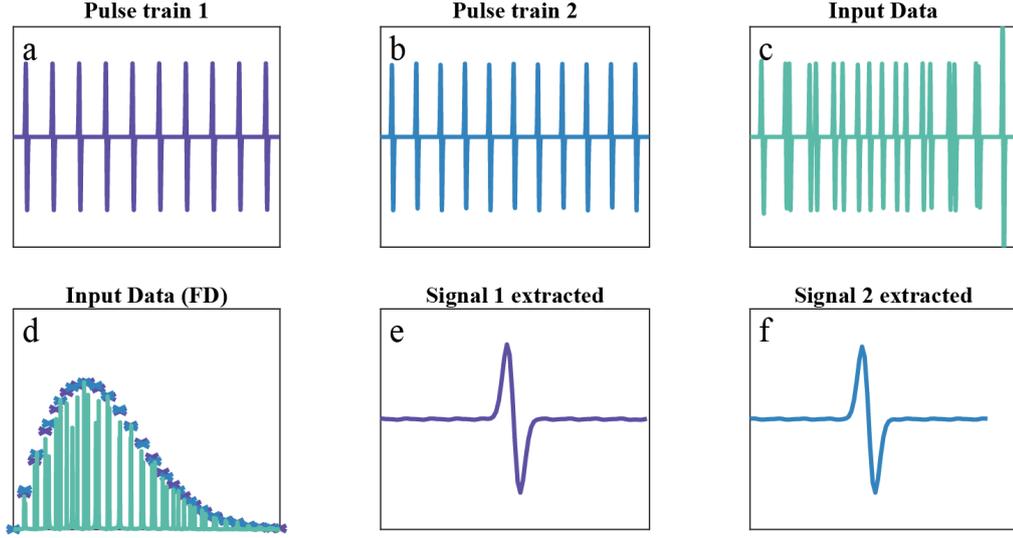
Figure 2.5: **Concept of multispectral PWFD optoacoustics.** a: Response of an optoacoustic point source illuminated with pulse waves featuring $20\,\text{ns}$ long pulses at $f_{rep} = 2\,\text{MHz}$. b: Optoaoustic response due to illumination with same pulse duration and $f_{rep} = 2.21\,\text{MHz}$. c: Sum of both waveforms as detected by transducer. d: Fourier transform of overlapping waveform, with frequency components corresponding to the two pulse waves (violet crosses, first pulse wave, blue crosses: second pulse wave). e: Inverse Fourier transformation of the frequency components associated to the first pulse wave. f: Same as e, but for the second pulse wave.

value f_{rep,N_λ} does not overlap with the lowest frequency component with the lowest value of the next group of components:

$$N_{f_2} = f_2/f_{rep,0}$$
$$N_{f_2} \cdot \Delta f < f_{rep,0} \tag{2.61}$$

To pick Δf correctly, the mid point value between the two limiting cases is calculated:

$$\Delta f = \frac{1}{2} \cdot \left(\frac{\delta f}{N_{f_1}} + \frac{f_{rep,0}}{N_{f_2}} \right) \tag{2.62}$$

Frequency component extraction in MS-PWFD

SWFD and PWFD rely on extracting the frequency content of a time domain signal. In SWFD, this can be achieved by using lock-in amplification or other demodulation techniques. When multiple frequency components are to be extracted, which is required for PWFD, digitizing the waveform and applying the fast Fourier transformation (FFT) algorithm is a viable method. In optoacoustic mesoscopy, a large number (typically $10^5 - 10^6$) of projections are acquired. Therefore, it is highly beneficial, when the frequency content of the acquired time domain data is extracted on the fly. In this case only N_f (eq. 2.51) instead of N_t (eq. 2.49) have to

be saved. This is only possible if efficient frequency extraction algorithms are used on powerful computer hardware. Typically, the FFT algorithm is implemented on a fast CPU or GPU unit. However, the FFT assumes that the input signal is periodic. In PWFD, this can be achieved by choosing an integration time t_{int} that is a multiple of the pulse wave repetition period:

$$t_{int} = \frac{N}{f_{rep}}, \quad N \in \mathbb{N} \tag{2.63}$$

Condition 2.63 is difficult to satisfy using several lasers in parallel, which all share the same integration time t_{int} but all have different repetition rates $f_{rep,\lambda}$. Since conditions 2.62 must also be satisfied, choosing appropriate parameters becomes difficult using multiple lasers. This can be solved by using an alternative frequency extraction algorithm. Lock-in amplifiers have already been discussed in section 1.6. Fundamentally it is based on the Fourier theorem:

$$(\mathcal{F}f)(\omega) = \frac{1}{\sqrt{2\pi}} \cdot \int_{-\infty}^{\infty} f(t) \cdot e^{-i\omega \cdot t} dt \tag{2.64}$$

which can be formulated as:

$$
\begin{aligned}
(\mathcal{F}f)(\omega) &= \frac{1}{\sqrt{2\pi}} \cdot \int_{-\infty}^{\infty} f(t) \cdot (\cos(\omega t) - i \cdot \sin(\omega t)) \, dt \\
(\mathcal{F}f)(\omega) &= \underbrace{\frac{1}{\sqrt{2\pi}} \cdot \int_{-\infty}^{\infty} f(t) \cdot \cos(\omega t) dt}_{I} - i \underbrace{\frac{1}{\sqrt{2\pi}} \cdot \int_{-\infty}^{\infty} f(t) \cdot \sin(\omega t) dt}_{Q} \\
(\mathcal{F}f)(\omega) &= I(\omega) - i \cdot Q(\omega) \tag{2.65}
\end{aligned}
$$

in the case of phase sensitive lock-in detection (known as IQ-demodulation) only one particular frequency ω_0 is to be extracted, as the low-pass filter will remove all frequency components that have not been shifted to zero, hence: $f(t) = sin(\omega_0 t + \phi)$. Multiplication by the sine and cosine function is performed by a hardware multiplication circuit. This is done by splitting the signal into two separate circuits, one representing the real component and one the imaginary. The integral can be replaced by a low pass filter whose cut-off frequency corresponds to the frequency resolution. The real (in phase, I component) and out of phase (quadrature, Q component) can be expressed as:

$$
\begin{aligned}
I(\omega_0) &= LPF\left(f(t) \cdot \cos(\omega_0 \cdot t)\right) \\
Q(\omega_0) &= LPF\left(-f(t) \cdot \sin(\omega_0 \cdot t)\right) \tag{2.66}
\end{aligned}
$$

where I and Q correspond to the real and imaginary component of the frequency component of the signal $f(t)$ at the frequency ω_0:

$$(\mathcal{F}f)(\omega_0) = I + i \cdot Q \tag{2.67}$$

When $f(t)$ has been digitized in N_{tot} samples over t_{int}, equations 2.66 can also be expressed as:

$$
\begin{aligned}
I(\omega) &= \frac{1}{N_{tot}} \cdot \sum_{n=0}^{N_{tot}} f_n \cdot \cos(\omega_0 \cdot t_n) \\
Q(\omega) &= \frac{1}{N_{tot}} \cdot \sum_{n=0}^{N_{tot}} -f_n \cdot \sin(\omega_0 \cdot t_n)
\end{aligned}
\tag{2.68}
$$

Since the mean value of sine and cosine function is unity, the normalization factor in equation 2.68 can be dropped. In PWFD, N_f frequency components must be extracted. Therefore, the operation in equation 2.68 must be performed for each frequency component. When f_n is expressed as a row vector of length N_t, this can be achieved by a matrix operation:

$$
\begin{aligned}
I(\omega_m) &= f_n \cdot ID_{m \times n} \\
Q(\omega_m) &= f_n \cdot QD_{m \times n}, \quad m \in [1, N_t], n \in [1, N_f]
\end{aligned}
\tag{2.69}
$$

with the demodulation matrix $ID_{t \times f}$ and $QD_{t \times f}$ given by:

$$
ID_{t \times f} = \begin{pmatrix} \cos(\omega_0 \cdot t_1) & \dots & \cos(\omega_{N_f} \cdot t_1) \\ \vdots & \ddots & \vdots \\ \cos(\omega_0 \cdot t_{N_t}) & \dots & \cos(\omega_{N_f} \cdot t_{N_t}) \end{pmatrix}
$$

$$
QD_{t \times f} = - \begin{pmatrix} \sin(\omega_0 \cdot t_1) & \dots & \sin(\omega_{N_f} \cdot t_1) \\ \vdots & \ddots & \vdots \\ \sin(\omega_1 \cdot t_{N_t}) & \dots & \sin(\omega_{N_f} \cdot t_{N_t}) \end{pmatrix}
\tag{2.70}
$$

This will yield a row vector length N_f containing the I and Q components for each frequency of interest. Matrix multiplication sums over the element of each vector, performing the operation shown in equation 2.68. Formulating the frequency extraction using matrix multiplication has several benefits:

1. It is possible to process arbitrary waveforms, even if they are not periodic. This allows any combinations of repetition rates for the pulse waves to be chosen, as long as condition 2.62 is fulfilled.

2. Matrix multiplications can be executed very efficiently in graphics processing units (GPU). This allows the acquired data to be compressed in real-time and only the extracted frequency domain data have to be stored.

3. The formalism can be applied to single and to multiple scans. For the latter case, the raw data is formatted in a matrix were each scan occupies a column vector resulting in a matrix where the frequency content of each scan occupies a column vector. Assuming that N_b scans are to be processes, each of length

N_t:

$$
\begin{pmatrix} f_1(t_1) & \dots & f_1(t_{N_t}) \\ \vdots & \ddots & \vdots \\ f_{N_b}(t_1) & \dots & f_{N_b}(t_{N_t}) \end{pmatrix} \cdot (ID + i \cdot QD)
$$

$$
= \begin{pmatrix} IQ_1(\omega_1) & \dots & IQ_1(\omega_{N_f}) \\ \vdots & \ddots & \vdots \\ IQ_b(\omega_1) & \dots & IQ_b(\omega_{N_f}) \end{pmatrix} \tag{2.71}
$$

Combined with the efficient implementation of matrix multiplication in GPUs, this allows to quickly process large amounts of data.

2.11 Signal strength and SNR comparison

After having introduced the various modulation patterns suitable for optoacoustic measurements, this chapter will give a theoretical discussion on the achievable signal strength and SNR of each of these modalities. These will later be compared to measurements presented in chapter 4.

Comparison of optoacoustic signal generation efficiency for different modalities

In SWFD, the illumination energy is evenly spread out over the entire measurement time and not concentrated into individual peaks. This resulted in weak energy transients. Equation 2.10 shows that the optoacoustic pressure is proportional to the rate of change of the heating function:

$$
\left(\nabla^2 - \frac{1}{v_s^2} \frac{\partial^2}{\partial t^2} \right) \cdot p(\vec{r}, t) = \frac{\Gamma}{v_s^2} \frac{\partial H(\vec{r}, t)}{\partial t}
$$

where the right side is identified as the *source term*

$$
p_S(t) = \frac{\Gamma}{v_s^2} \frac{\partial H(\vec{r}, t)}{\partial t} \tag{2.72}
$$

to identify the maximum pressure of the source term for single wave excitation, the excitation signal is assumed as a single sine wave:

$$
H^W(t) = H_0^W \cdot \sin(2\pi f_0 t) \tag{2.73}
$$

and the source term in equation 2.72 becomes:

$$
p_S^W(t) = H_0^W \frac{\Gamma}{v_s^2} \cdot 2\pi f_0 \cdot \cos(2\pi f_0 t) \tag{2.74}
$$

which has a maximum at $t = 0$, hence:

$$
\boxed{\max(p_S^W) = p_S^W(t = 0) = H_0^W \frac{\Gamma}{v_s^2} \cdot 2\pi f_0} \tag{2.75}
$$

to calculate the signal generation efficiency of single pulse excitation, the heating function is assumed to be a Gaussian pulses:

$$H_t(t) = H_0^P \cdot e^{-\frac{1}{2} \cdot \left(\frac{t-t_0}{\tau_L}\right)^2} \tag{2.76}$$

consequently, the source term to the right of equation 2.10 becomes:

$$p_S^P(t) = H_0^P \frac{\Gamma}{v_s^2} \cdot \frac{\partial}{\partial t} e^{-\frac{1}{2} \cdot \left(\frac{t-t_0}{\tau_L}\right)^2} \tag{2.77}$$

$$= H_0^P \frac{\Gamma}{v_s^2} \cdot \left(\frac{t-t_0}{\tau_L^2}\right) \cdot e^{-\frac{1}{2} \cdot \left(\frac{t-t_0}{\tau_L}\right)^2} \tag{2.78}$$

which features a maximum at $t = \tau_L + t_0$. Thus, the maximum pressure created by the source term is:

$$\max(p_S^P) = p_S(\tau_L + t_0) = H_0^P \frac{\Gamma}{v_s^2} \cdot \frac{1}{\tau_L \sqrt{e}} \tag{2.79}$$

Setting the term of equation 2.75 and 2.79 into relation yields:

$$\frac{\max(p_S^P)}{\max(p_S^W)} = \frac{H_0^P \frac{\Gamma}{v_s^2} \cdot \frac{1}{\tau_L \sqrt{e}}}{H_0^W \frac{\Gamma}{v_s^2} \cdot 2\pi f_0}$$

$$\frac{\max(p_S^P)}{\max(p_S^W)} = \frac{H_0^P}{H_0^W} \cdot \frac{1}{\sqrt{e} \cdot 2\pi} \cdot \frac{1}{\tau_L \cdot f_0} \tag{2.80}$$

therefore, at equal irradiation strength and assuming $\tau_L = 1/f_0$, the optoacoustic pressure generated by single wave excitation is $\sqrt{e} \cdot 2\pi \approx 10.35$ bigger than that generated by single pulse excitation. Since different waveforms of the excitation methods yield different energy transients, scaling factors $\sqrt{e}$ and 2π are introduced. For practical applications, the illumination power for single pulse and single wave excitation cannot be equal. According to the ANSI limits for maximum permissible exposure of skin, a single pulse with a duration of 10 ns or less may feature a pulse energy of up to $P_0 = 20 \, \text{mJ/cm}^2$ [174]. Assuming the pulse duration is $\tau_L = 10 \, \text{ns}$ and that an area of $1 \, \text{mm}^2$ is illuminated, the maximum illumination power H_0 is:

$$H_0^P = \frac{P_0}{\int_{-\infty}^{\infty} H_t(t) dt} = \frac{P_0}{\sqrt{\pi}/2 \cdot \tau_L} = \frac{200 \, \mu\text{J}}{\sqrt{\pi}/2 \cdot 10 \, \text{ns}} = 22.6 \, \text{kW} \tag{2.81}$$

further assuming the Grueneisen-parameter to be 0.81 [175] and the speed of sound to be $v_s = 1450 \, \text{m/s}$ [176] the initial pressure can be calculated:

$$\max(p_S^P) = 22.6 \, \text{kW} \cdot \frac{0.81}{(1450 \, \text{m/s})^2 \cdot 10 \, \text{ns} \cdot \sqrt{e}} = 522 \, \text{kPa} \tag{2.82}$$

The ANSI limits also specify a limit for the maximum permissible exposure for continuous irradiation as $200 \, \text{mW/cm}^2$ [174]. Again assuming an illumination spot

size of $1\,\text{mm}^2$, the resulting illumination power is $H_0^W = 2\,\text{mW}$. Further presuming that $\omega_0 = 1/2\pi \cdot 1/\tau_L = 100\,\text{MHz}$ results in:

$$\max(p_S^W) = 2\,\text{mW} \cdot \frac{0.81}{(1450\,\text{m/s})^2} \cdot 2\pi \cdot 100\,\text{MHz} = 480\,\text{mPa} \qquad (2.83)$$

for experimental parameters in compliance with the ANSI MPE limits, the signal strength generated by single pulse illumination is more than 10^5 times stronger than that generated by single wave illumination [174]. The continuous illumination limit also applies for pulsed illumination. Comparing the signal generation efficiency for the two cases:

$$\frac{\max(p_S^P)}{H_0^P} = \frac{522\,\text{kPa}}{22.6\,\text{kW}} = 23\,\text{Pa/W} \qquad (2.84)$$

$$\frac{\max(p_S^W)}{H_0^W} = \frac{480\,\text{mPa}}{2\,\text{mW}} = 242\,\text{Pa/W} \qquad (2.85)$$

yields:

$$\frac{\max(p_S^W)/H_0^W}{\max(p_S^P)/H_0^P} = \frac{242\,\text{Pa/W}}{23\,\text{Pa/W}} = 10.52 \qquad (2.86)$$

Which is in good agreement with the discussion of equation 2.80.

If the sample was illuminated at the maximum possible pulse energy of $200\,\text{µJ/mm}^2$, the repetition rate would be limited to $10\,\text{Hz}$. Otherwise the continuous illumination limit of $2\,\text{mW/mm}^2$ would be exceeded.

SNR comparison for different modalities

No single light source exists that can provide single pulses powerful enough to generate detectable signals and at the same time provide a sufficient bandwidth to generate single waves at a similar bandwidth. Therefore, PWTD excitation was introduced to generate optoacoustic signals by pulsed excitation utilizing the same light source as used for single frequency excitation. The SNR of the signal was raised to detectable levels by coherent averaging in the time domain. Assuming a constant noise background with a noise equivalent pressure of n_{nep}, the SNR of a single pulse is proportional to:

$$SNR_{PWTD} \propto \frac{P_S^P}{n_{nep}} = \frac{H_0^P}{n_{nep}} \cdot \frac{\Gamma}{v_s^2} \cdot \frac{1}{\tau_L \sqrt{e}} \qquad (2.87)$$

acquiring N pulses and averaging them coherently, the final SNR increases proportional to the square root of N:

$$SNR_{PWTD} \propto \sqrt{N} \cdot \frac{P_S^P}{n_{nep}} = \sqrt{N} \cdot \frac{H_0^P}{n_{nep}} \cdot \frac{\Gamma}{v_s^2} \cdot \frac{1}{\tau_L \sqrt{e}} \qquad (2.88)$$

assuming a given repetition rate f_{rep} and obtaining the generated signal over a given integration time t_{Int}, equation 2.88 becomes:

$$SNR_{PWTD} = \sqrt{f_{rep} \cdot t_{Int}} \cdot \frac{P_S^P}{n_{nep}} = \sqrt{f_{rep} \cdot t_{Int}} \cdot \frac{H_0^P}{n_{nep}} \cdot \frac{\Gamma}{v_s^2} \cdot \frac{1}{\tau_L \sqrt{e}} \qquad (2.89)$$

The SNR depends directly on the pulse energy H_0^P, but only on the square root of the integration time t_{Int}. Assuming the pulse energy was below the ANSI limit, it made sense to optimize the pulse energy first within the limits of the used light source and then increased the repetition rate until the maximum continuous power of $2\,\mathrm{mW/mm^2}$was reached. The SNR obtained by single wave excitation in the frequency domain can be defined in the same way:

$$SNR_{SWFD} = \frac{P_S^W}{n_{nep}} \cdot \sqrt{t_{Int}} = \frac{\sqrt{t_{Int}}}{n_{nep}} \cdot H_0^W \frac{\Gamma}{v_s^2} \cdot 2\pi f_0 \qquad (2.90)$$

similar as for SNR_{PWTD}, the peak power of SNR_{SWFD} should be optimized within the experimental parameters first, as it has a linear influence on SNR, while the integration time only affects the SNR by its square root. In PWFD, a pulse wave with constant repetition rate was used. Hence the energy was concentrated onto discrete frequency components in the frequency domain. The signal generation efficiency was the same as for PWTD. To understand the effect of the integration time on the SNR achieved by PWFD, a constant noise density spectrum $n_{nep}(f) = const.$ was assumed. If the discrete Fourier transform was applied to such a signal, the noise power was equally distributed over the entire spectrum. The bandwidth in frequency domain was proportional to the integration time. The upper limit of the bandwidth was defined by the Nyquist theorem. However, the longer the integration time, the more noise was acquired. In result, the noise level showed a proportionality $\sqrt{t_{Int}}$. At the same time, the number of frequency components was not affected by the increase in acquisition time:

$$SNR_{PWFD} = \frac{S}{N} = \frac{P_S^P \cdot \sqrt{N}}{n_{nep}} \cdot = \frac{\sqrt{t_{Int} \cdot f_{frep}}}{n_{nep}} \cdot H_0^P \cdot \frac{\Gamma}{v_s^2} \cdot \frac{1}{\tau_L \sqrt{e}} \qquad (2.91)$$

Chapter 3

Materials and methods

3.1 Experimental setups for PWFD evaluation and mesoscopy

As laser diode based mesoscopy system are a novelty, it was required to understand how appropriate illumination can be implemented. Theoretical understanding of how the signal generation efficiency in different modalities compare is well established (sections 2.7 and 2.8). However, no experimental data providing a fair comparison has been published. To demonstrate the properties of *PWFD* optoacoustics and compare them to established optoacoustics techniques, **Signal Evaluation Setup 1** was devised which is a non-scanning setup featuring an arbitrary waveform laser diode driver with a fixed illumination to further understand the effects of different illumination strategies. Subsequently, **Signal Evaluation Setup 2** was devised with an adjustable illumination, to optimize the illumination spot size for further measurements.

Once the optimal parameters for *PWFD* optoacoustics were established, a dedicated system for mesoscopic imaging, **single wavelength SW-PWFD Mesoscopy Setup 3** was constructed. This setup sacrificed the flexibility of arbitrary excitation patterns, as they have been optimized using the previous setups. Instead, a pulsed diode driver was deployed that could generate optical pulses at a higher energy than the arbitrary waveform laser driver. The setup was finally augmented with **multispectral** capabilities presented in **MS-PWFD Mesoscopy Setup 4**. The technical outlines of these systems will be discussed in this chapter, while the results achieved with these setups will be discussed in chapter 4. A measurement computer, configured as shown in table 3.1 was used for all discussed measurements.

Table 3.1: List of Components of measurement PC

Component	Type	Manufacturer
Processor	Core i7 3820 3.6 GHz	Intel
Mainboard	P9X79	Asus
RAM	DDR3 64 GB	various
Disk	500 GB 850 EVO	Samsung
GPU	GTX1070	Nvidia

3.2 Signal evaluation setup 1

Table 3.2: List of components composing **Signal Evaluation Setup 1**.

Component	Type	Manufacture
Function generator	DG4162	Rigol
Laser diode driver	BFS-VRM 03 HP	Picolas
Laser diode (450 nm)	FBLD-450-0.8W-FC105-BTF	FrLaCo
Illumination lens	GRIN2906	Thorlabs
Positioning system	M-460A	Newport
Transducer	13183A	Imasonic
Amplifier	Miteq AU-1291-R	Hauppauge
Data acquisition (DAQ)	Picoscope 3204D (8 bit, 125 Ms/s)	Picotech

Laser diodes provide a far lower instantaneous power than Q-switched lasers. Consequentially, confining the light from the laser diode to the sensitive region of the transducer is essential for high-SNR *PWFD* imaging. A setup dedicated to generating high signal strength was developed. This was done to investigate illumination patterns that were not expected to generate a high SNR. A photographic image is shown in figure 3.1b. A **GRIN** lens, which is able to operate under water, was used to focus the excitation light on the transducers sensitivity field (fig. 3.1a). *Signal evaluation setup 1* allowed to generate arbitrary illumination patterns. Thereby the SNR achievable by different illumination strategies could be compared. All used components are listed in table 3.2. The function generator was programmed by the measurement PC described in table 3.1 and provided the desired waveform to the directly modulating laser diode driver. The driver operated the 450 nm laser diode which was coupled into a 105 µm core diameter fiber and lead into the GRIN lens. The GRIN lens was positioned using a custom made holder so it focused the light onto the focal point of the transducer. By placing a sample in the common focal point of the GRIN lens and the transducer, accentuate measurements of the SNR generated by various illumination strategies could be completed. The generated optoacoustic signal was amplified using a high gain, high bandwidth, low noise amplifier, and subsequently digitized by the data acquisition system (DAQ) and send to the PC for further processing.
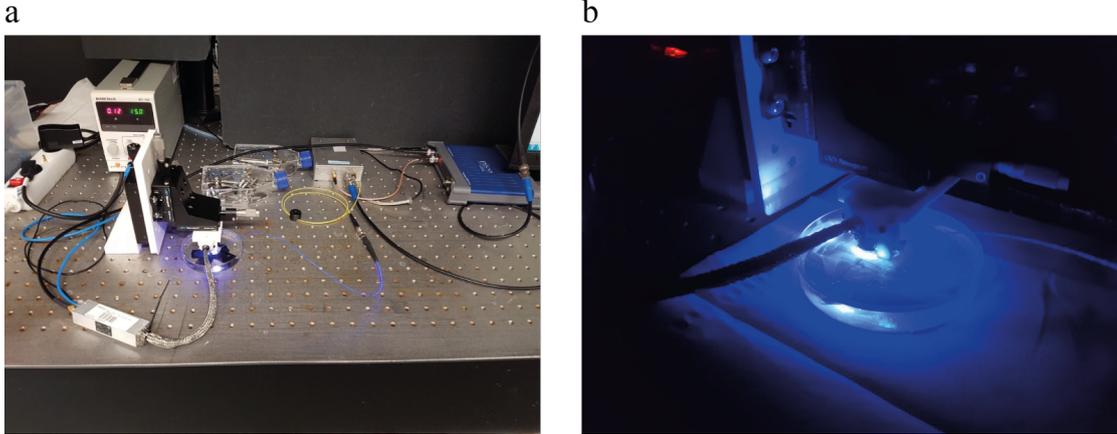
Figure 3.1: **Photographic image of Signal Evaluation Setup 1**. a: Overview of entire setup featuring the data acquisition, the laser diode and laser driver and the transducer, mounted on the position control system. b: Image enlargement of the transducer and a sample during a measurement.

3.3 Signal evaluation setup 2

A setup with adjustable illumination was developed to investigate how the illumination spot size and further measurement conditions affect the achievable SNR. The components used for this setup are listed in table 3.3.

Table 3.3: List of components composing **Signal Evaluation Setup 2**.

Component	Type	Manufacture
Function generator	33522B	Keysight
Laser diode driver	BFS-VRM 03 HP	Picolas
Laser diode (780 nm)	FOLD-785-600-VBG-BTF	FrLaCo
Illumination lens	RMS4X	Thorlabs
Positioning system	M-460A	Newport
Transducer	V324-SU	Olympus NDT
Amplifier	Miteq AU-1291-R	Hauppauge
Data acquisition	Picoscope 3204D (8 bit, 125 Ms/s)	Picotech

The function generator was programmed by the measurement PC described in table 3.1 and provided the desired waveform to the laser diode driver. The driver operated the 780 nm laser diode which was coupled into a 105 µm core diameter fiber and lead into the microscope objective. The objective in turn was mounted onto a positioning system. This allowed the distance between the sample and the objective to be varied by up to 10 mm to control the size of the illumination spot. A photographic image of the setup can be seen in figure 3.2a and a detailed CGI generated image in 3.2b. To determine the mean power of the laser, a thermal power meter which is insensitive to rapid power fluctuations was used (30(150)A-BB-18 combined with Vega power meter, Ophir.)

The optoacoustic signal generated by the illuminated target was detected with a
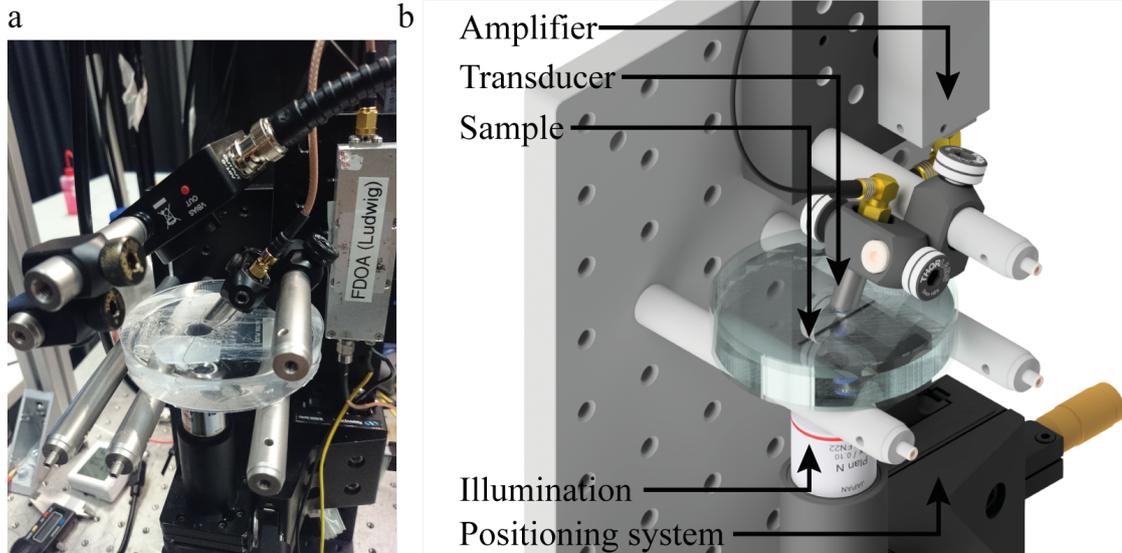
Figure 3.2: **Image of Signal Evaluation Setup 2.** a: Photographic image of setup one, showing the Petri dish with the suture, the illumination objective (below Petri dish) and transducer (in Petri dish). b: Computer generated image of the same setup.

focused 25 MHz transducer (focal length 12.5 mm, NA=0.25). Next, the signal was amplified using a high gain, high bandwidth, low noise amplifier, and subsequently digitized by the DAQ and send to the PC for further processing.

3.4 Pulsed light source for PWFD mesoscopy

The arbitrary laser driver used in setup 1 and 2 does not provide sufficient current to generate more intensive light pulses with laser diodes. Therefore, a dedicated pulsed laser diode driver was deployed for setup 3 and 4 (fig. 3.3). An AC-MOSFET circuit was used to generate short current pulses (fig. 3.3a). The short, high current pulse passing through the laser diode gives rise to a short, yet intense light pulse. Various laser diodes have been tested for different current pulses, corresponding to a voltage up to 300 Volt have been conducted [177]. The pulse energy and duration was defined by selecting appropriate values for $R_{CL} = 3.4\,\Omega$ and $C = 400\,\mathrm{pF}$. For many laser diodes, pulse energies in excess of 200 nJ were possible while the pulse duration was kept below 10 ns (fig. 3.3b). The function generator (fig. 3.3c, blue) provided the trigger signal, which was passed on to the laser diode driver mounted on a PCB (fig. 3.3c, light green). The laser diode was mounted inside the first XY stage. The collimation lens were mounted in the consecutive z stage. Subsequently, the light is focused and coupled into the output fiber, which was also positioned using high precision XY stages.

To ensure the absorption measured were comparable, a photodiode was used that constantly acquired a small part (1%) of the laser energy of the laser diode. The resulting data was subjected to the same PWFD processing as the optoacoustic
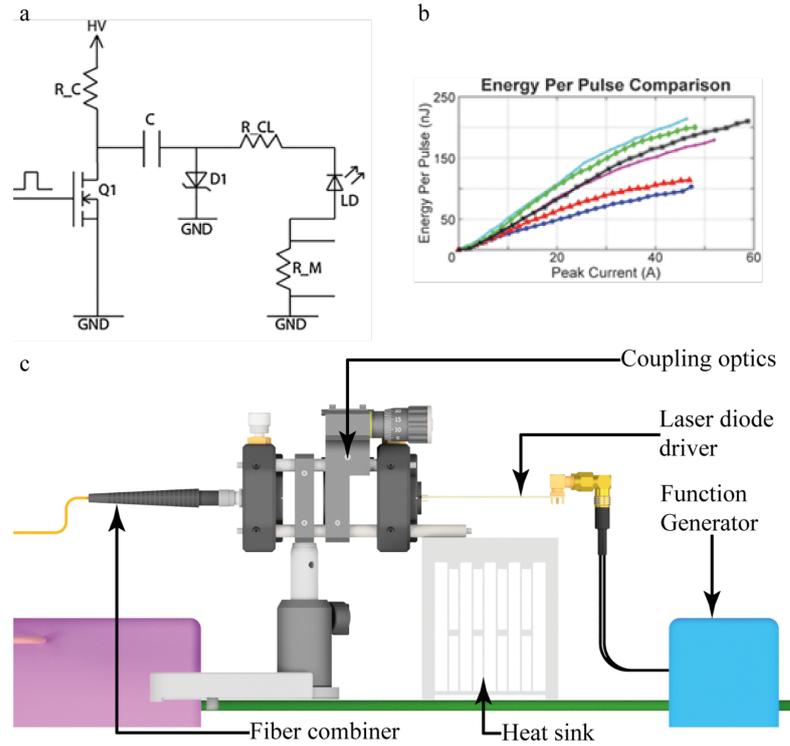
Figure 3.3: **Schematic and pulse energy of light source.** a: Schematic of used pulsed current source to generate short current pulses to operate CW laser diodes. b: Pulse energies achievable for various laser diodes using high voltage up to 300 Volt. c: CGI of SW-PWFD light source together with coupling optics [177].

data. Together with the spectral sensitivity of the photodiode provided by the manufacturer (Thorlabs, biased Si detector response), the pulse energy could be monitored during the measurement and was used to correct the amplitude of the resulting optoacoustic signal. Furthermore, for multispectral applications as shown in setup 4, The signal originating from the individual laser diodes in the photo diodes data was identified. Thereafter the phase of the acquired photo diode signal was used to synchronize the laser trigger relative to the data acquisition.

3.5 SW-PWFD mesoscopy setup 3

After confirming that *PWFD* signal generated by laser diodes were detectable and ideal parameters for optimum SNR generation had been established, a dedicated imaging system was constructed. The components used to assemble the setup are listed in table 3.4.

Unlike the previous setups, the imaging system did no longer feature an arbitrary laser diode driver, but a pulsed driver instead (sec. 3.4). This allowed to generate more intensive laser pulses. The total measurement setup including all utilized components can be seen in figure 3.4a. To ensure homogeneous illumination and confine the excitation light to the sensitivity field of the transducer, a multi-fiber

Table 3.4: List of components composing **SW-PWFD setup 3**.

Component	Type	Manufacture
Function generator	33522B	Keysight
Laser diode driver	$I_{max} = 60\,\text{A}$, $\tau_p = 6\,\text{ns}$	Custom made [177]
Laser diode 445 nm	NDB7K75	Nichia
Positioning system	M-663	PI
Illumination	MPC-4-M21-M41-P23	Lasfiberio
Transducer	SNX140517_ HFM23	Sonaxis
Data acquisition	Razor Express 16XX	GaGe

based illumination scheme was developed (fig. 3.4c). The light from the laser diode was coupled into a 420 µm diameter fiber which splits into four 105 µm, NA=0.22 fibers through a tapered fiber combiner. Using a high resolution stereolithografic 3D printer (Form 2, Formlabs, USA) a custom designed component holder was created, which positioned the polished fiber ends equally spaced around the transducer (60° to the acoustic axis, at a distance of 3 mm to the acoustic focal point). This resulted in an illumination spot size of 1.32 mm and an illumination spot area of 1.36 mm² (fig. 3.4c). The custom holder containing the fiber based illumination system and the transducer was placed on a set of high precision stages.

50 Ω termination of the electrical output was required to optimize shielding and avoid external interference to couple into the cable. Piezoelectric transducers however feature a capacitative electrical behaviour. Thus, switching the laser diodes using the custom made driver caused significant interference. The interference signal shared the same frequency components as the optoacoustic signal and could not be rejected using the *PWFD* formalism. To minimize this effect, the cable was kept as short as possible. A custom made component using a fused deposition modeling 3D printer (Ultimaker 2, Ultimaker, Netherlands) was designed to hold the high precision stages and the high gain amplifier. This way, the amplifier could be kept in close proximity to the transducer and the cables could be kept short (10 cm). A CGI generated image of the component is shown in figure 3.4d. Together with further external shielding, the effect of the trigger interference on the optoacoustic signal could be suppressed to acceptable levels. Using the high-throughput data acquisition system, a large number of scans could be performed in a short time. The acquired data was transferred to the computer's graphics processing unit, where it was processed using the formalism discussed in section 2.9. An image of the system conducting a scan of a phantom is presented in figure 3.4d.

a
Stage Controller
Sensor Holder
Amplifier
Measurement PC
Sensor
Stages

Laser diode driver
Function Generator
Heat sink
Coupling optics
Fiber combiner

b   c   d
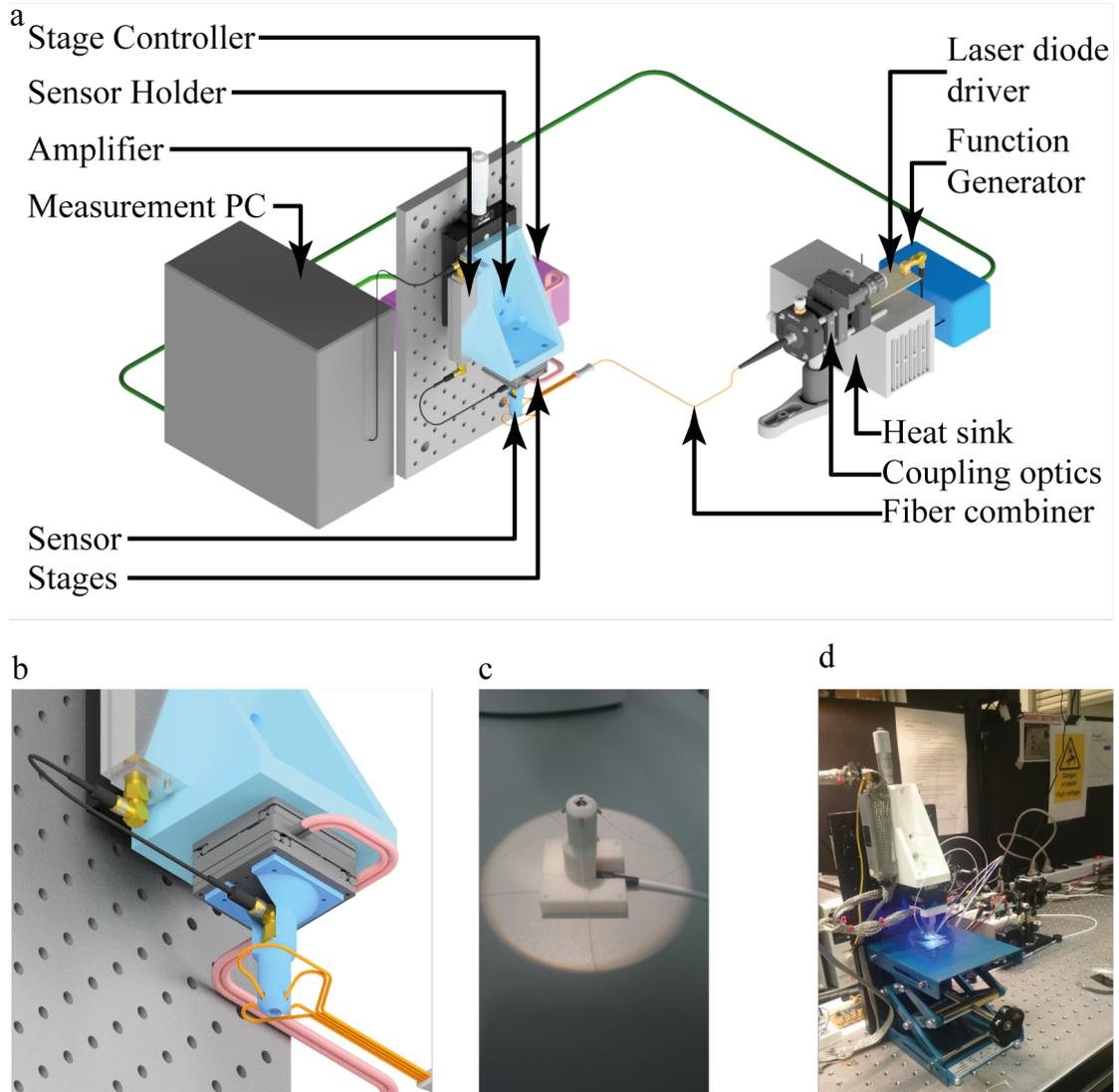
Figure 3.4: **SW-PWFD setup 3 system and measurement head.** a: CGI image of system featuring all components. b: CGI rendering of measurement head. The focused high frequency transducer is located inside the blue holder. The fibers originating from the tapered fiber combiner (orange) are arranged around the transducer and directed at its focal point. c: Photographic image of measurement head. d: Photographic image of system during operation.

3.6 MS-PWFD mesoscopy setup 4

This setup presents an augmentation of the setup presented in section 3.5, as it utilizes four laser diodes instead of one to employ frequency sharing in *PWFD*. The components making up the *MS-PWFD* system are listed in table 3.5. Three

Table 3.5: List of components composing *MS-PWFD setup 4*.

Component	Type	Manufacture
Function generator 1	33522B	Keysight
Function generator 2	33522B	Keysight
Laser diode driver	$I_{max} = 60\,\text{A},\ \tau_p = 6\,\text{ns}$	Custom made
Laser diode 445 nm	NDB7K75	Nichia
Laser diode 465 nm	NDA7175	Nichia
Laser diode 638 nm	HL63193MG	Ushio
Laser diode 808 nm	K808D02FN	BWT
Positioning system	M-663	Physik Instrumente
Illumination	4x4 200/220μm, 0.22NA	LFiber
Transducer	SNX140517_ HFM23	Sonaxis
Data acquisition	Razor Express 16XX	GaGe

additional laser diode drivers, coupling optics and laser diodes at different wavelengths were installed (fig. 3.5a). The light originating from these diodes were coupled into a star coupler with four input fibers and four output fibers, all with a diameter of 200 μm and numerical aperture of 0.22. The output fibers were arranged around the transducer using the existing holder (fig. 3.4b). The second channel of the existing function generator was used to to drive the second laser diode. Furthermore, another function generator was installed to operate laser 3 and 4 (fig. 3.5b). An overview of the entire system is shown in figure 3.5c. Since the absorption coefficient of many absorbers is lower at 638 nm and 808 nm the capacitance of the driver for these two laser diodes R_{CL} was increased to $C = 800\,\text{pF}$, which yielded a higher pulse energy, but also resulted in a slightly higher pulse duration. The resulting pulse duration and pulse energies are shown in table 3.6. The repetition rate of each laser was chosen according to equation 2.62.

Table 3.6: Approximate pulse energies and duration of laser diodes used in *MS-PWFD setup 4*.

| Wavelength	Pulse energy	Pulse duration
445 nm	200 nJ	7 ns
465 nm	200 nJ	7 ns
638 nm	140 nJ	15 ns
808 nm	140 nJ	15 ns
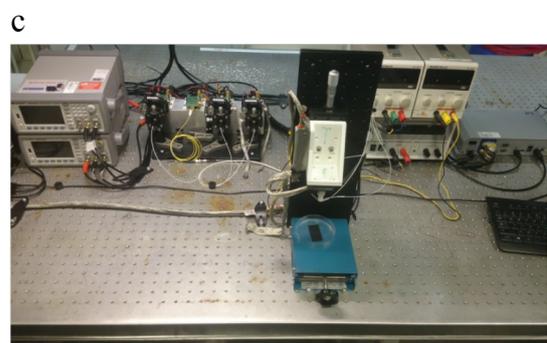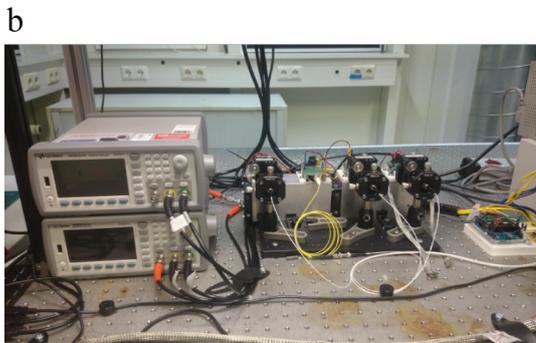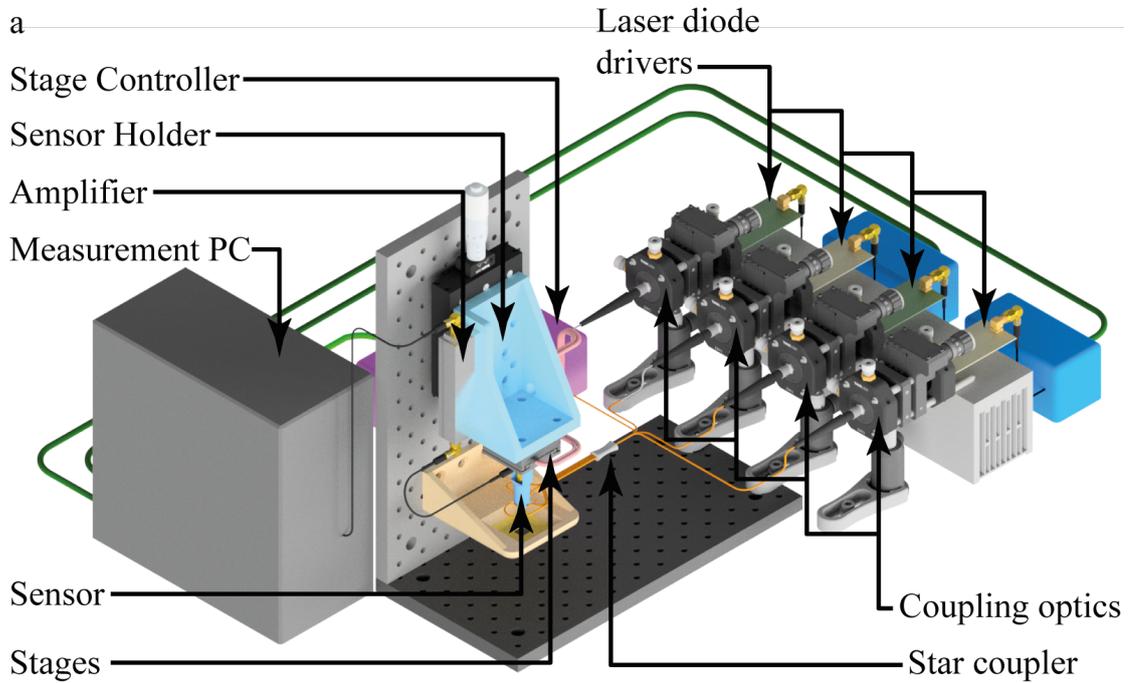
Figure 3.5: **Illustration of MS-PWFD Mesoscopy Setup 4.** a: CGI rendering of the system including all used components. Three additional light sources were added to provide multispectral capabilities. A second function generator was added to control all four light sources. Furthermore, the light from the light sources was guided to the sample using a fiber star coupler. b: Photographic image of the light source, showing the coupling optics and the function generators. c: Photographic image of entire system.

3.7 Image acquisition in PWFD mesoscopy

To scan a field of view of X by Y, the translation stages were moved to the starting position of the scan at $(x, y) = (-X/2, -Y/2)$. Next, the *fast x* stage was set into motion at a velocity, chosen to cover the distance of one step δx in the time it took to generate and acquire one pulse wave at $t_{step} = N_{Avg} \cdot f_{rep}$. The actual velocity of the stage was reduced by 10%-25% to provide a *safety margin* to ensure the acquisition of one scan was complete before the position of the next scan was reached. Every time the *fast* stage moved the defined step size δx, a trigger signal was sent to the function generator and one *A-scan* was acquired: the function generator generates the desired pulse wave, which served as a trigger signal for the pulsed laser diode driver. Simultaneously, the data acquisition system was triggered by the function generator. The resulting optoacoustic signal was detected by the spherically focusing transducer and was digitized at $Fs = 200\,\mathrm{MS\,s^{-1}}$ and stored in the on-board memory of the data acquisition system. When the *fast* stage reached its target position of $(x, y) = (+X/2, -Y/2)$, one *B-scan* was completed.

Next, the acquired data was transferred from the on-board memory of the data acquisition system to the RAM memory of the measurement PC and the *slow* stage was moved by one step size $(x, y) = (+X/2, -Y/2 + \delta y)$ and the x stage was set into motion in the opposite direction, again sending a trigger to the function generator every time the stage moved the distance δx. While the next B-scan was acquired, the raw data of the previous B-scan was processed using the PWFD algorithm on the measurements PCs GPU. This was done to reduce the data acquired at each step from $N_t = N_{avg} \cdot Fs/f_{rep}$ data points to $N_f = Fs/(2 \cdot f_{rep})$, resulting in a data reduction of $2 \cdot N_{avg}$. The factor of 2 is accounted for by the PWFD algorithm, which only extracts the frequencies up the Nyquist frequency f_{Nq}. This process was repeated until both stages have reached their final position $(x_{final}, y_{final}) = (+X/2, +Y/2)$.

The acquired PWFD data was converted to the time domain by the inverse fast Fourier transform algorithm. The signal was passed on to a time domain filtered back-projection algorithm introduced in section 2.3 for reconstruction.

3.8 Submersible beam profiler

To measure the illumination spot size of a setup under the same conditions used during measurements (hence, submerged by the coupling medium), a commercial CMOS camera (daA1920-30uc/CS-Mount, Basler) was modified. The casing of the camera was removed and the electronics sealed with two component epoxy (Epoxydharz L, Composite Technology). The camera was submerged in a Petri dish so that the CMOS sensor was at the same position within the dish as the sample would be during an optoacoustic measurement.

3.9 Signal quality evaluation phantoms

Phantom 1, 100 µm suture

Phantom 1 consisted of a 100 µm suture made of surgical nylon that has been suspended 2 mm above the bottom of a 70 mm Petri dish. This way, any ultrasound generated by the suture due to the optoacoustic effect could propagate in all directions without being directly influenced by the boundaries of the vessel. Furthermore a 10 mm hole was drilled through the bottom of the Petri dish and covered with a standard microscope slide. The suture could be illuminated from the bottom, without influencing the shape of the focus through absorption or scattering by the Petri dish material. To investigate the influence of scattering on the measurements, intralipid was added to the coupling medium (I141 SIGMA Intralipid 20% emulsion, Sigma Aldrich).

Phantom 2, 10 µm suture

Similar to *phantom 1*, this phantom presented a surgical suture suspended in a Petri dish. To study higher frequencies, the suture diameter was only 10 µm. The suture was spanned across a 30 mm Petri dish which in turn was placed inside a 70 mm Petri dish. This allowed any generated ultrasound to propagate omni-directionally without disturbance.

Phantom 3, Siemens star on glass

Suture phantoms provide a highly localized optoacoustic source. To evaluate the homogeneity of imaging systems, a more distributed source was of benefit. A commercially resolution test target for microscopy applications (R1L1S3P, Thorlabs USA, fig. 3.6) was used. While not being a suspended target like *phantom 1 and 2* in which the generated ultrasound could travel in all directions without disturbance, the manufacturing process ensured well defined optical properties over the entire region.

The target consisted of a soda lime glass wafer with a pattern of 120 nm thick chrome. The high optical absorption of chrome made it an excellent optoacoustic signal source. The pattern of the chrome featured a standard resolution test target, commonly known as a *Siemens Star*. It was a 10 mm circular pattern consisting of chrome 72 sectors interrupted by 72 clear sectors. At the center of the circle, a clear circular area with 200 µm diameter was located to aid with alignment. This pattern presented different feature sizes depending on the distance from the center. At the outer edge, the distance segment length of a sector is 218 µm, at the inner edge it was 4.36 µm. The glass wafer was placed inside a 30 mm Petri dish to allow it to be covered with water for acoustic coupling.

Figure 3.6: **Image of test target used for phantom 3**. The lower right test target was used to construct the phantom. It consisted of a 120 nm thick layer of chrome on clear soda lime glass image and data provided by Thorlabs).

Phantom 4, suspended microspheres

Point like emitters are favourable optoacoustic sources for resolution qualification. 10 µm ferromagnetic polystyrene microspheres were used to obtain such a phantom. To produce the phantom, agarose without microspheres was poured in to a 30 mm Petri dish to about 1 mm below the upper edge and allowed to solidify. The microspheres were added to a 1.3% solution of agarose (Agarose BioReagent, for molecular biology, low EEO, Sigma-Aldrich) at a concentration of $1 \times 10^6 \, \text{mL}^{-3}$. This mixture was than poured onto the existing layer of clear agarose, until the Petri dish was filled completely. The top 1 mm layer of agarose in the Petri dish contained to $1000 \, \text{mm}^{-3}$ microspheres on average.

Blood vessel mimicking phantom

To explore the systems ability to investigate liquid chromophores in small blood vessels below the skin, a specialized vessel mimicking phantom was used. Because it is difficult to manufacture phantoms of this size, a microfluidic chip was used instead. The substance under investigation was covered by a layer of TOPAS, which is a material whose optical properties are well understood [178], but its acoustic properties are not studied in depth. To enable the usage of TOPAS based phantoms for optoacoustic imaging, a sample of the same TOPAS foil used for microfluidic chips was acquired. Acting as a well characterized test target, a 10 µm nylon suture was placed partially under the TOPAS foil. By comparing the optoacoustic signal of the suture acquired through the TOPAS foil to the signal of the same suture acquired without the foil, the effect of the foil on acoustic waves over a wide frequency range could be explored.

The phantom itself was based on a microfluidic chip (microfluidic ChipShop

GmbH, Germany), featuring a channel in a polycarbonate carrier open at one side (fig. 3.7a). It carried rectangular channels with several tenths of μm edge length and several cm total length. These channels were covered with $145\,\mu m$ thick foil of TOPAS. While some of the ultrasound generated by the content of the channel was absorbed by the TOPAS covering layer, its properties are now well understood and could be accounted for. The channel was accessible by Micro-Luer connectors on both ends allowing various liquid chromophores to be inserted (fig. 3.7b).
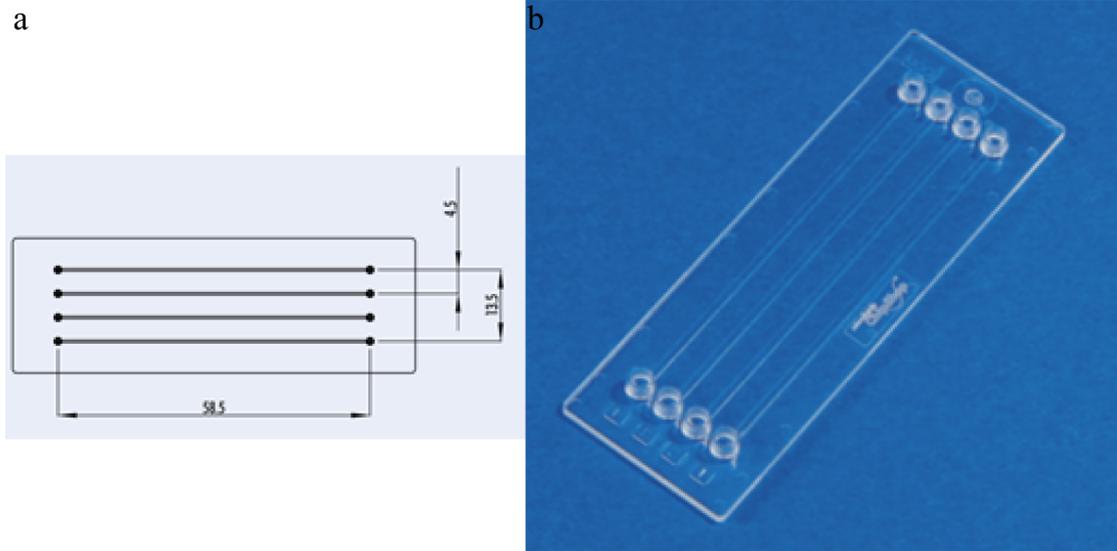
Figure 3.7: **Dimensions and visual image of microfluidic chip.** a: Dimensions of the microfluidic chip used which matched a standard microscopy slide. The channels were spaced $4.5\,mm$ apart and were $58.5\,mm$ long. The size of the channel was in region of $10–100\,\mu m$. b: Photographic image of a microfluidic chip containing four channels.

3.10 *In vivo* imaging setups

After having established relevant measurement parameters using various phantom and signal evaluation setups, the aim of this thesis is to demonstrate the imaging performance of the presented system in medical and biological applications.

Universal holder for *in vivo* measurements

The position of the analysed specimen had to be maintained within the field of view of the measurement setup for the duration of the measurement while not affecting the specimen to a point where it changes its behaviour or properties. Past studies have shown that volunteers were able to remain motionless for up to several minutes during measurements. Using the presented setup, fields of view covering several mm^2 could be acquired during that time. Using a skin holding and flattening device, high resolution images of human skin could be obtained.

Biological model organism such as mice are unable to actively cooperate during measurements. Hence, they were anaesthetized to ensure they remained motionless. Having designed a custom small animal holder, it was possible to position relevant parts of the subjects body (i.e. the ears) within the field of view of the measurement setup for the measurement duration. For the duration of the measurement the animal remained under stable anaesthesia and its vital functions were monitored.
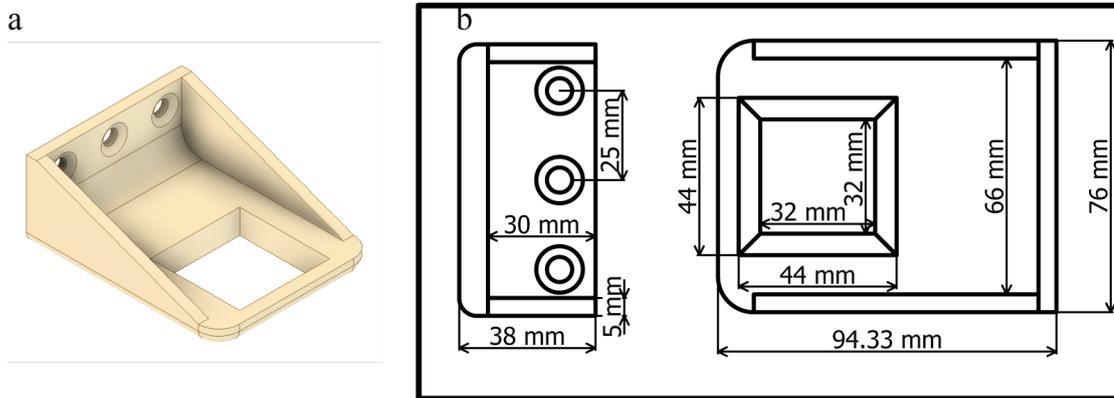
Figure 3.8: **Universal holder for *in vivo* measurements.** a: CGI of universal holder. b: projected view of universal holder, providing its dimensions. All units in millimter.

All discussed *in vivo* measurements utilize a *Universal Holder* (fig. 3.8a). The specimen was placed beneath the aperture and mechanically stabilized. This way, the sample was positioned exactly in the middle of the imaging setups field of view and held it in the focal plane. This was achieved in combination of custom designed holders of each applications, which were attached to the specimen (commonly with double sided tape) and fit into the central window of the universal holder. The dimensions of the holder are given in figure 3.8b. The holder was manufactured using the same stereolithographic 3D printer as was used to produce the measurement head presented in section 3.5.

Small animal imaging setup

The small animal imaging setup consisted of three components, all manufactured using 3D printing technology. The animal was anaesthetized and rested inside the holder (fig. 3.9a). It allowed the animal's head to rest on an elevated stage and its ears to be positioned in the two small cavities on the left and right. The right ear was fixed on the imaging platform using double sided tape. Then, a small fixation device introduced in figure 3.9c was placed on top of the ear to be investigated and ultrasound gel was applied to the mouse ear for acoustic coupling. Gel instead of water was used to avoid leakage from the skin holder. The skin holder would fit below the universal holder. This fixation device fulfilled multiple functions. First, it kept the ear flat so it could be imaged reliably. Second, it provides a small container in which gel can be filled as a coupling medium for the ultrasound to travel in. An image of a mouse during a measurement is shown in figure 3.10d.
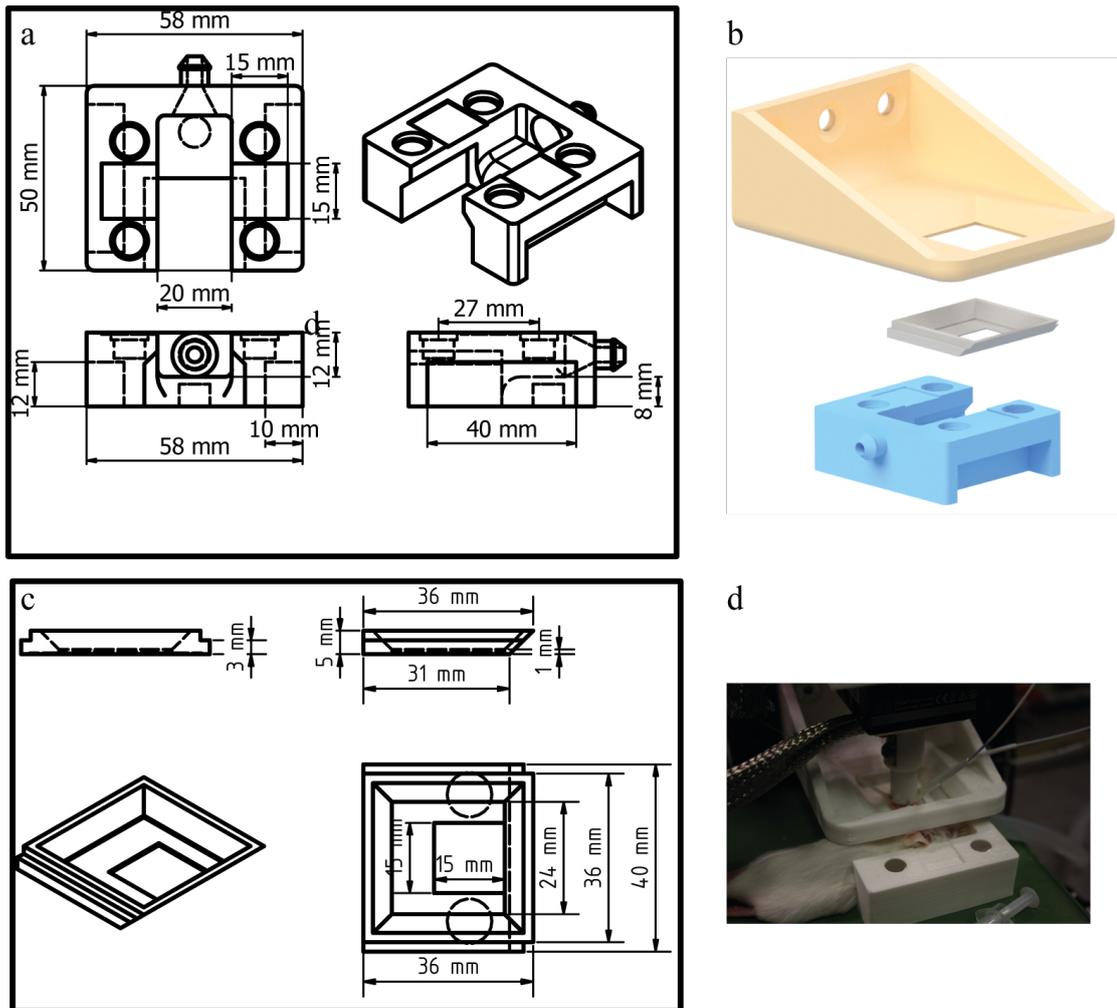
Figure 3.9: **Custom made small animal holder to image mouse ears.** a: Holder for the head and ear of mouse. b: Drawing illustrating how the components are assembled to perform an *in vivo* measurement. c: Cover over the mouse ear provide a water tight reservoir for the coupling medium. d: Photographic image of *in vivo* measurement using small animal holder.

The test subject was anaesthetized by using a 3%/97% isofluorane/oxygen mixture as its breathing gas and placed in the custom designed mouse holder. The animal was maintained under anaesthesia using a 2%/98% isofluorane/oxygen mixture. Next, a cannula was inserted into the tail vein of the animal to provide intravenous access. Finally, the mouse was placed in the positioning clamp of the mesoscopic setup.

Human skin imaging setup

A small skin holder was glued onto the volunteers skin using double sided tape (fig. 3.10a). The open aperture was positioned over the part of skin to be investigated, commonly on an extremity of the volunteer (arm). The holder flattened the skin

and provided a small reservoir for a coupling medium, normally distilled water (fig. 3.10b). The volunteer was then positioned under the universal holder (fig. 3.8). This ensured that the region of interest of the skin was placed exactly at the center of the field of view of the volunteer.
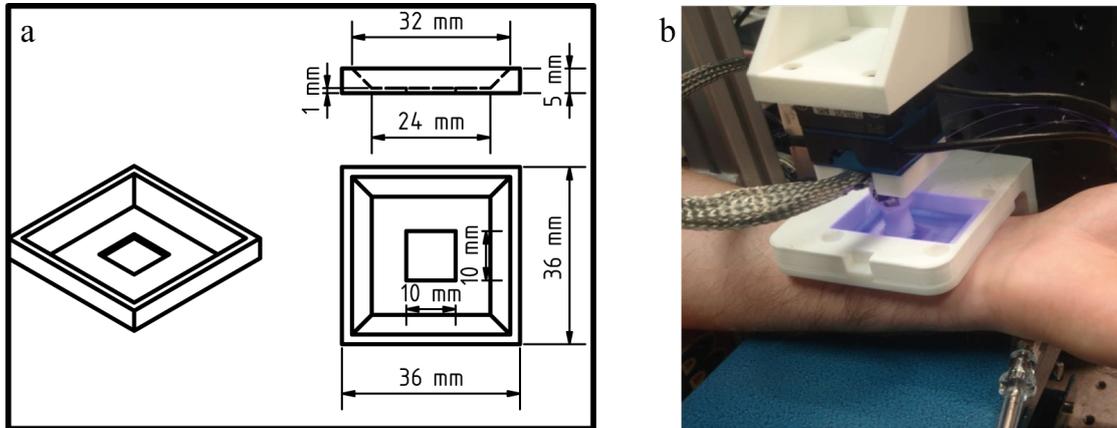
Figure 3.10: **Custom made small animal holder to image human skin.** a: Dimensions of the custom skin holder. b: Image of a scan on the left lower arm of a volunteer being conducted. The custom designed skin holder was placed on the region of interest using double sided tape. The skin holder was then positioned in the universal holder shown in figure 3.8. After distilled water for ultrasound coupling was added on the skin holder, mesoscopic scans could commence.

List of volunteers for human skin measurements

The skin of the lower right arm of a number of volunteers was acquired. The age and sex of the volunteers is listed in table 3.7.

Table 3.7: List of Volunteers.

Volunteer	Age	Gender
1	29	male
2	32	female
3	26	male
4	37	male
5	29	male
6	29	female
7	28	male
Mean	30.0	

Chapter 4

Results

This chapter begins by evaluating the signal strength generated by the presented modalities in order to optimize them for imaging. Subsequently, the dedicated imaging setups are used to demonstrate the capability of PWFD imaging on phantoms, as well as medical and biological applications.

4.1 Evaluation of PWTD, SWFD, and PWFD

To illustrate the potential of PWFD optoacoustic imaging, the optoacoustic signals of PWFD to PWTD and SWFD acquisition are compared. This is of particular interest, since SWFD and PWTD are established modalities and are therefore important reference to evaluate PWFD.

Depth of field and SNR comparison of SWFD and PWFD

The data presented in figure 4.1 was acquired by Mathias Steffner during his master thesis under supervision by the author.

Due to experimental limitations, previous studies only focused on limiting cases of pure single wave in the frequency domain and pure pulsed excitation in the time domain. To provide a more holistic study, *Signal Evaluation Setup 1* was used to generate an excitation pattern with 62.5 kHz repetition rate and 160 ns pulse duration with a pulse energy of 1.6 µJ (fig. 4.1a). This presents the limiting case of pulse wave excitation. A frequency component of the resulting optoacoustic signal present at 3.125 MHz. It was processed using the SWFD algorithm. The frequency components were converted to the time domain using the inverse Fourier transform (fig. 4.1b) and the resulting SNR was calculated (fig. 4.1i). The same data was processed in PWFD (fig. 4.1b) and the SNR was calculated (fig. 4.1i), were 500 available frequency components were used. The resulting depth of field was $DoF \approx 24$ mm. The signal processed in PWTD is plotted for reference (fig. 4.1b). Subsequently, the repetition rate was increased to 312.5 kHz (fig. 4.1c). The pulse energy was decreased to 320 nJ so the average power of 100 mW was maintained. Again, the PWFD components and SWFD component at 3.125 MHz were extracted and converted to the time domain and plotted together with the PWTD signal
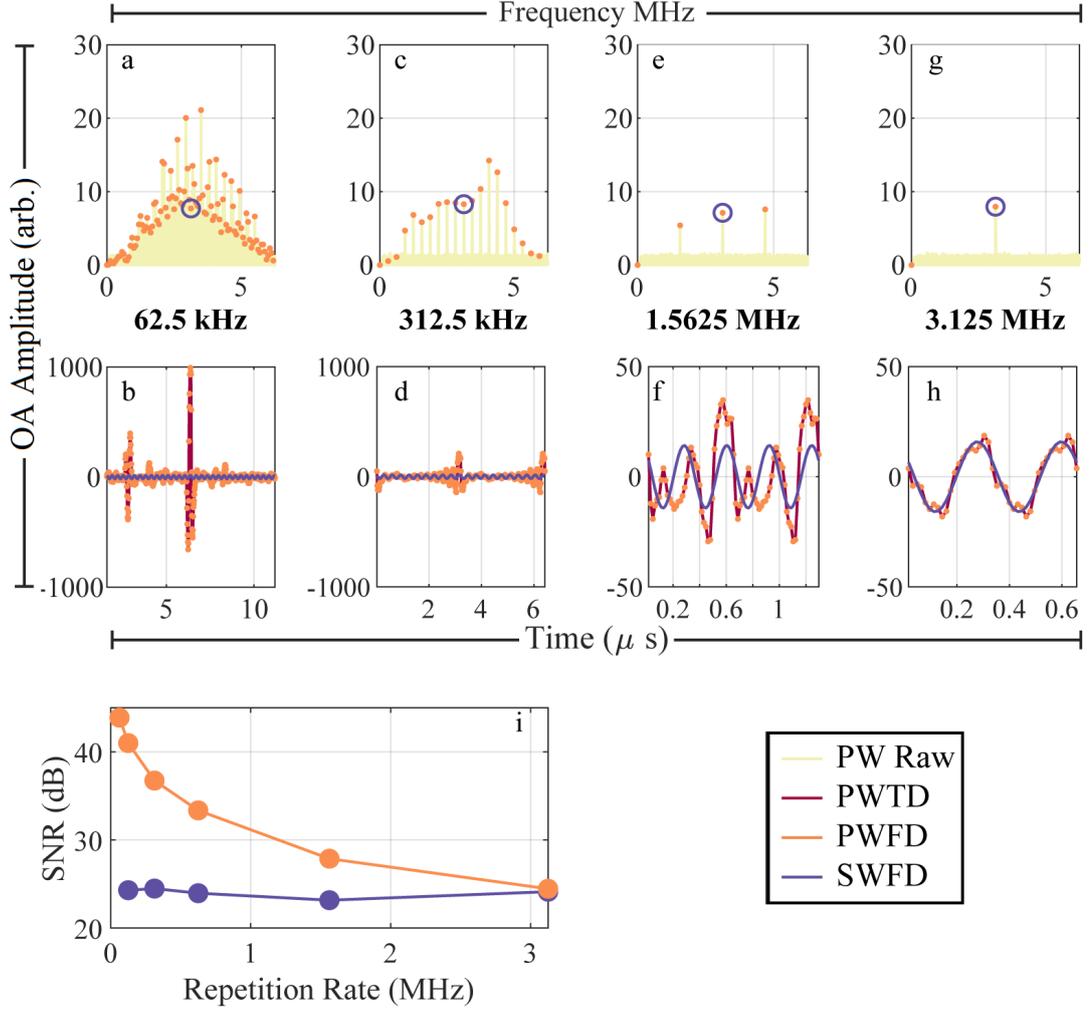
Figure 4.1: **Optoacoustic response of *phantom 1* due to pulse wave illumination in *Setup 1* with $\tau_p = 160$ ns and $\bar{P} = 100$ mW.** a: optoacoustic response in frequency domain with $f_{rep} = 62.5$ kHz (light yellow). PWFD components highlighted in orange. The SWFD component at 3.125 MHz marked by blue circle. b: Inverse Fourier transform of frequency components shown in a. PWTD added for reference (red). c: As a, with $f_{rep} = 312.5$ kHz. d: inverse Fourier transform of frequency components from c. e: As a, with $f_{rep} = 1.5625$ MHz. f: inverse Fourier transform of frequency components from e. g: As a, with $f_{rep} = 3.125$ MHz. h: inverse Fourier transform of frequency components from g. i: SNR of PWFD and SWFD as a function of repetition rate.

for reference (fig. 4.1d). The SNR of both signals was calculated (fig. 4.1i). 125 frequency components were available to provide a depth of field of $DoF \approx 6$ mm. It is apparent that as the repetition rate is increased, the depth of field and the signal amplitude have drastically decreased, while fewer frequency components become available. The same trend can be observed when the repetition rate is further increased to 1.5625 MHz (fig. 4.1e-f), yielding 20 available frequency components and $DoF \approx 1.2$ mm using a pulse energy of 64 nJ. Finally, the repetition is set to

3.125 MHz and the pulse energy to 32 nJ, which corresponds to a duty cycle of 50% (fig. 4.1g). The depth of field corresponded to $DoF \approx 600\,\mu m$. Therefore, the frequency components used for PWTD and PWFD are identical. Consequentially, the time domain signal (fig. 4.1h) and the reconstructed SNR (fig. 4.1i) are also identical.

Figure 4.1i clearly shows that SNR of PWFD decreases when the repetition rate is increased. Therefore, the increase in number of energy transient does not compensate the decrease in steepness of the energy transient. The SNR achieved by SWFD does not show a strong dependency on the repetition rate. This is logical, as the pulse duration and therefore the frequency content of the excitation waveform was kept constant for all repetition rates.

Theoretical SNR comparison between PWTD and PWFD

To provide a solid background for the equivalence of PWFD and PWTD, a computer simulation of a pulse wave was conducted. 1000 Gaussian pulses with 20 ns full width half maximum (FWHM) pulse duration were simulated at a repetition rate of 200 kHz. Thereafter, the time domain derivatives of the signal were calculated to simulate the optoacoustic effect of a very small absorber. The result was superimposed with additive white Gaussian noise (AWGN) to simulate the limited SNR of optoacoustic measurements. The noisy signal was then processed with the algorithms described in section 2.7 and 2.9 (fig. 4.2a). To study the effect of different measurement conditions, the pulse wave was generated for different initial SNR values of 0 dB, 5 dB and 10 dB. The SNR of the signal resulting from PWFD and PWTD processing was calculated for different numbers of averages, ranging from 10 to 1000 averages in steps of 10 (fig. 4.2b). The SNR of the output signal scales with the square root of the number of pulse averages. Nevertheless, the initial SNR is the fundamental parameter that determines the output SNR. This is true for any number of averages. Exemplary signals for 10, 100 and 1000 averages are shown in fig. 4.2c-h. The result of the PWFD and PWTD domain data share the same waveform. This is in good agreement with the discussion presented in section 2.9 and 2.11 which indicated that the same signal quality can be achieved using PWFD compared to PWTD.
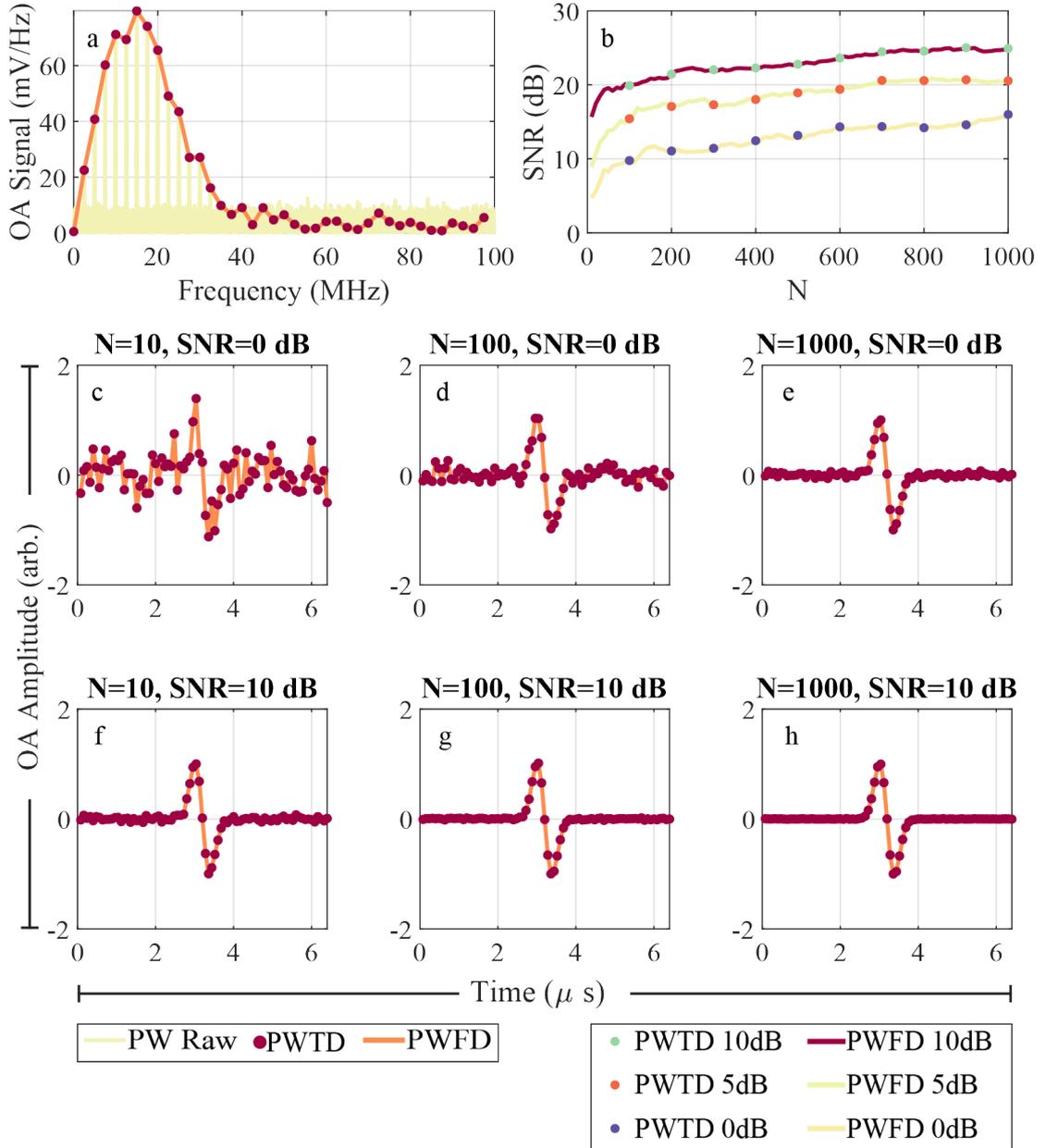
Figure 4.2: **Simulated OA response of pulse wave in PWFD and PWTD for various measurement conditions.** a: Illustrative example of raw data and frequency components. b: SNR of PWFD and PWTD for different initial SNR and different number of averages. c-h: Time domain signal of PWFD and PWTD for different number of averages and initial SNR.

Measured SNR comparison between PWTD and PWFD

The simulated pulse wave strongly suggests that the resulting waveform and SNR is the same, regardless whether the data is processed using PWFD or PWTD (fig. 4.2). To confirm this result with an experimental measurement, *Imaging Setup 3* was used to illuminate *phantom 2* and generate a pulse wave consisting of 1000 pulses featuring 8 ns pulse duration at 200 kHz repetition rate and approximately

200 nJ pulse energy. Using a sampling rate of $200\,\mathrm{MS\,s^{-1}}$, a total number of $N_f = 500$ frequencies are acquired. Assuming a speed of sound of $v_s = 1500\,\mathrm{m/s}$, the depth of field would be $DoF_z = 7.5\,\mathrm{mm}$. The resulting optoacoustic response was acquired and underwent PWFD and PWTD processing for different number of averages (fig. 4.3).
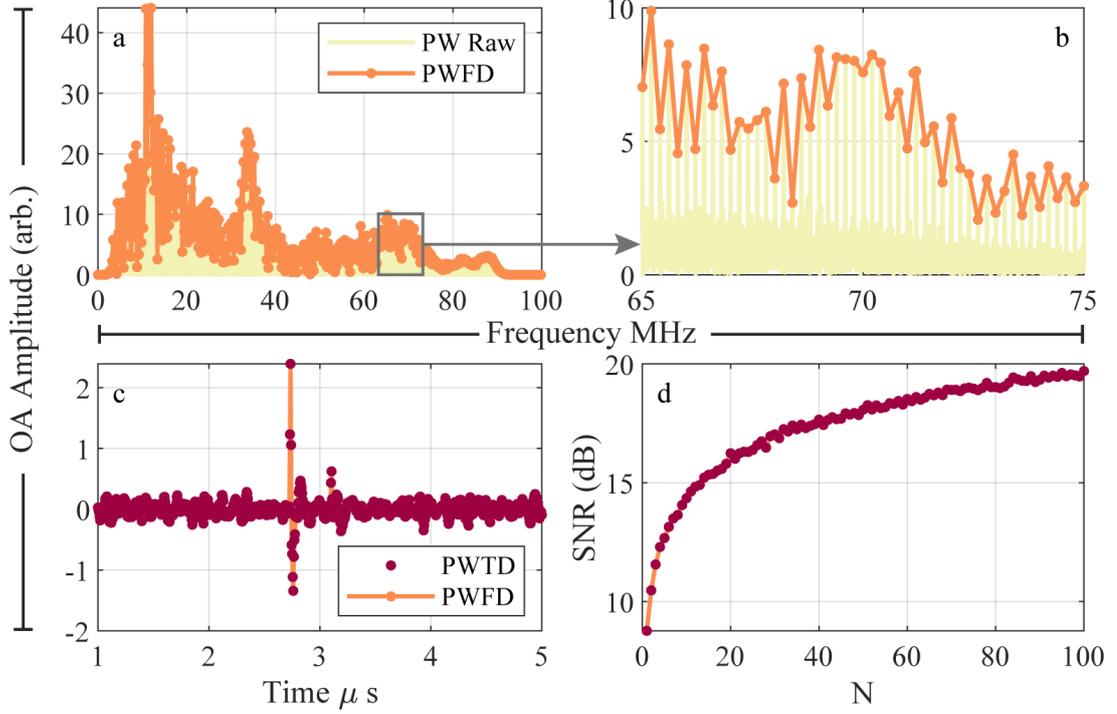
Figure 4.3: **Measured OA response of pulse wave processed PWFD and PWTD.** a: Data of 100 pulses presented in the frequency domain, overlayed with extracted frequency components. b: zoom in on small interval of a. c: Example of acquired pulse in the time domain. d: Evaluation of SNR as a function of the number of pulses averaged.

Fig. 4.3a shows the raw data of 100 acquired pulses in the frequency domain together with the extracted frequency components and a zoom on a small region (fig. 4.3b). The frequency components were converted to the time domain by the inverse fast Fourier transform algorithm (fig. 4.3c). The data was superimposed with the coherent time averaged raw data for reference. The SNR in the time domain after PWFD and PWTD processing is shown as a function of the number of averages (fig. 4.3d). For any number of averages, PWTD and PWFD feature the same SNR. The waveform of PWFD in time domain precisely follows that of PWTD. This is in agreement with the results presented in figure 4.2 and the theoretical predictions discussed in section 2.9 and 2.8.

SNR comparison between SWFD and PWFD in various measurement conditions

To evaluate the performance of PWFD under various measurement conditions, *Signal Evaluation Setup 2* was used to acquire the optoacoustic signal of a pulse wave and a single wave and processed them in the three discussed modalities. *Phantom 1* was used as a test target. The setup was not changed between measurements. Thus, the results reflect the potential of each modality under the same experimental parameters. All measurements were acquired with the same *average* laser power of 100 mW. The measurement was started with the manual stage in the top position. For 10 ms, a pulse wave consisting of 25 ns long pulses at 2 MHz repetition rate was send to the diode laser by the function generator, yielding a pulse energy of 50 nJ. The resulting optoacoustic signal was acquired at 62.5 MS/s. Immediately afterwards, a single wave at 24 MHz was send to the diode laser and the optoacoustic signal was acquired again. Upon completion, the stage was lowered by 1 mm and the process was repeated, until the stage has arrived at its lowest position. After the measurement series, 0.5 mL of intralipid emulsion was added to the distilled water used as a coupling medium for the ultrasound. Under these conditions the measurement series described above was repeated. This process was rerun until the scattering coefficient has reached $\mu_a = 100 \, \text{cm}^{-1}$ which mimics the scattering properties of biological tissue. Thereafter, *phantom 1* was removed from the setup and replaced with the submersible beam profiler presented in section 3.8. Subsequently, the diode laser was operated at minimum power and the CMOS camera was used to measure the area illuminated. This measurement was performed for all stage positions used for the described measurement series.

The used digitizer shows a slight frequency offset. This has to be taken into account before further processing. The actual sampling rate was measured using the known frequency of the single wave and found to be $62.499 \, \text{MS s}^{-1}$. To account for this, two time vectors for the acquired data were generated, the first one corresponding to the actual and the second one to the desired sampling rate of $62.5 \, \text{MS s}^{-1}$. Then, a linear interpolation of the acquired data from the first to the second time vector was conducted.

The unprocessed data acquired is shown in 4.4a. The pulse wave is highlighted by the dashed red lines. The SNR in both cases was too low and no optoacoustic signal could be seen. This raw data was converted to the frequency domain using the FFT (fig. 4.4b). In the frequency domain, the information carrying frequency components were easily identified and isolated (fig. 4.4c). As discussed in section 2.9, the envelope of these frequency components corresponds to the frequency spectrum of a single pulse. The frequency components were converted to the time domain using the inverse fast Fourier transform algorithm (fig. 4.4d) and the optoacoustic signal can be seen clearly. Consequently, the SNR of each signal was calculated in the time domain. The data was analysed as a function of the number of averages N_{avg} (i.e. the deposited energy, figure 4.4e). Since PWFD and PWTD share the same pulse shape, they also featured the same SNR. The SNR of SWFD was weaker for all studied cases. Furthermore, the SNR displayed a square-root dependency of the deposited pulse energy.
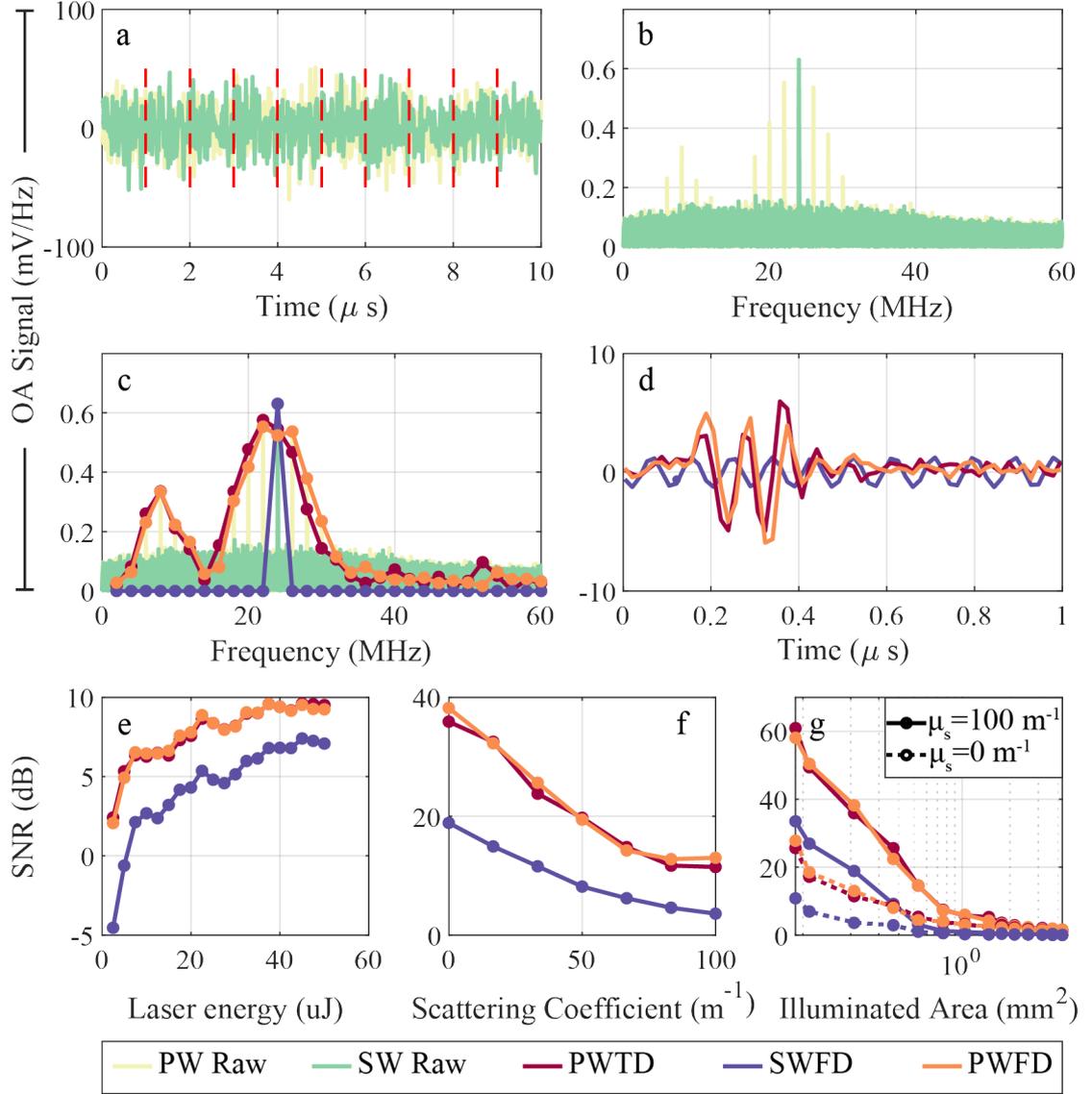
Figure 4.4: **Elaboration of signal processing and results of modality evaluation measurements.** a: Raw pulse wave and single wave data. Red dashed lines show individual pulses. b: data from a in to the frequency domain. c: Frequency components of raw data extracted. The frequency spectrum of PWTD was added for reference. d: Frequency components converted to the time domain. PWTD data is shown for reference. e: achievable SNR illustrated as a function of total deposited laser energy (i.e number of averages). f: achievable SNR presented as a function of the scattering coefficient. g: achievable SNR shown as a function of illuminated area for no scattering and $\mu_s = 100\,\mathrm{cm}^{-1}$

.

In the presence of scattering, the SNR showed an exponential decay (fig. 4.4f). When studying the effect of illumination on the achievable SNR, a clear dependency between to illumination spot size was found (fig. 4.4g). A good agreement between the SNR achieved in PWFD and PWTD was found, while the SNR achieved using

SWFD was lower for all considered cases.

Effect of pulse duration on SNR in PWTD

The data presented in figure 4.5 was acquired by Mathias Steffner during his master thesis under the author's supervision.

To establish a relationship between achievable SNR and pulse duration, *Evaluation Setup 1* was utilized together with *phantom 1*. The phantom was exposed to a pulse wave consisting of 1000 pulses at a repetition rate of $f_{rep} = 62.5\,\text{kHz}$ and a pulse duration of $\tau_p = 160\,\text{ns}$. The resulting signal was passed through a bandpass filter and processed in PWTD and the SNR of the resulting signal was calculated. Upon completion, the pulse duration was increased by 10 ns and the measurement was conducted again. This process was repeated until the pulse duration reached 5.2 µs. Figure 4.5a shows the pulse at $\tau_p = 300\,\text{ns}$ duration at different bandwidth. None of the shown pulses have reached their maximum amplitude. Figure 4.5b shows the pulse at $\tau_p = 600\,\text{ns}$ duration. The pulse corresponding to a bandwidth of 10 MHz has reached its maximum. Figure 4.5c shows the pulse at $\tau_p = 2\,\mu\text{s}$ duration, in which the pulse corresponding to a bandwidth of 3 MHz bandwidth has reached its maximum. Figure 4.5d shows the pulse with $\tau_p = 5.2\,\mu\text{s}$ were the rising and falling edge at each bandwidth is clearly separated, revealing the substructure of the edges.

Unlike to be expected from the discussion presented in section 2.1, the shortest pulse duration did not yield the highest signal strength. The signal SNR as a function of the pulse duration for different bandpass filters was determined (fig. 4.5e). The maximum SNR was achieved when the pulse duration corresponded to the inverse of the systems available bandwidth (fig. 4.5f).
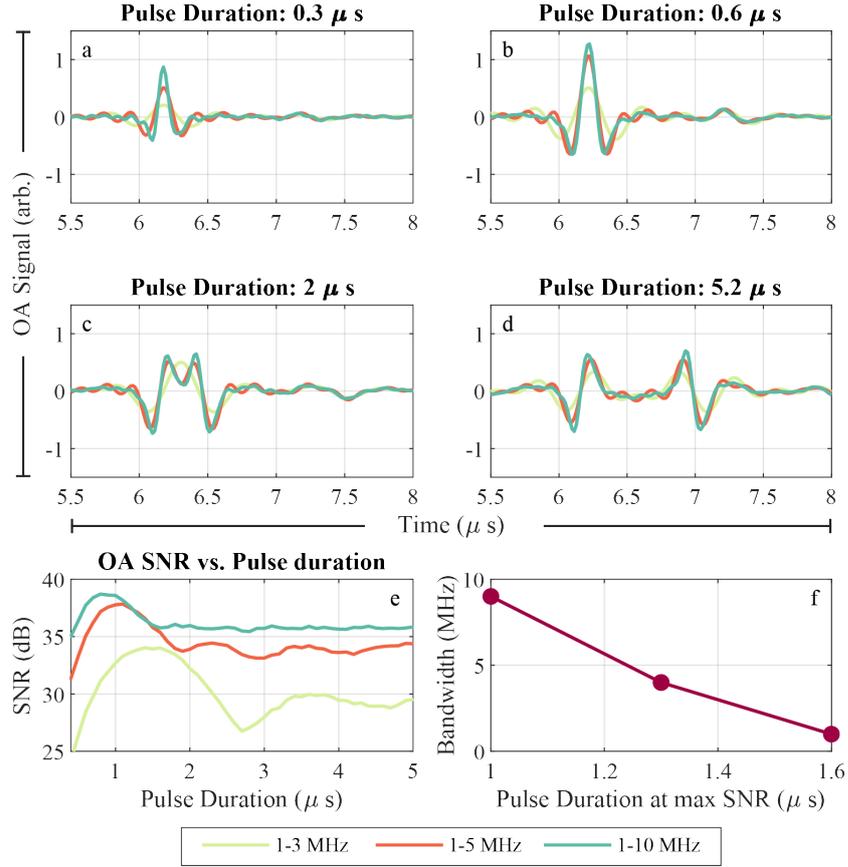
Figure 4.5: **SNR vs. pulse duration for different signal bandwidth**. a: Optoacoustic signal for $\tau_p = 300\,\text{ns}$. b: Optoacoustic signal for $\tau_p = 600\,\text{ns}$. c: Optoacoustic signal for $\tau_p = 2\,\mu\text{s}$. d: Optoacoustic signal for $\tau_p = 5.2\,\mu\text{s}$. e: SNR for three different bandwidths shown as a function of pulse duration. f: Pulse duration featuring the maximum SNR as function of signal bandwidth.

4.2 Evaluation of SW-PWFD mesoscopy

In section 4.1, the equivalence between PWFD and PWTD and the potential to generate optoacoustic signals efficiently has been demonstrated. In this section, the imaging setups that have been presented in section 3.5 and 3.6 will be evaluated. Different parameters will be explored and the imaging performance will be characterized using various phantoms and measurements conducted of the skin of two adult volunteers. This section will focus on demonstrating the potential of SW-PWFD imaging, while the next section, will discuss the opportunities of MS-PWFD.

Fluence correction of SW-PWFD mesoscopy

To demonstrate the imaging performance of *Mesoscopy Setup 3*, a mesoscopic raster scanning of *phantom 3* was conducted of a field of view of $(X, Y) = (10\,\text{mm}, 10\,\text{mm})$ using a step size of $\delta x = 10\,\mu\text{m}$ and the laser repetition rate

was set to $f_{rep} = 200\,\text{kHz}$ and the number of averages to $N_{avg} = 100$. The measurement time was approximately 45 minutes, the total acquisition time was $t_{acq} = N_p \cdot N_{Avg}/f_{rep} = 500\,\text{s}$, about 8.3 minutes. The remaining 36 minutes were required to transfer data from the data acquisition system to the RAM memory of the computer. In summary, a total of $N_p = 10^6$ positions at a depth of field of $DoF_z = v_s/f_{rep} = 200\,\text{kHz} = 7.5\,\text{mm}$ and $N_f = 500$ frequency components were acquired. The data was converted to the time domain using the inverse fast Fourier transform algorithm and passed on the filtered back-projection algorithm. The maximum intensity projection of the reconstructed data is shown in figure 4.6a.
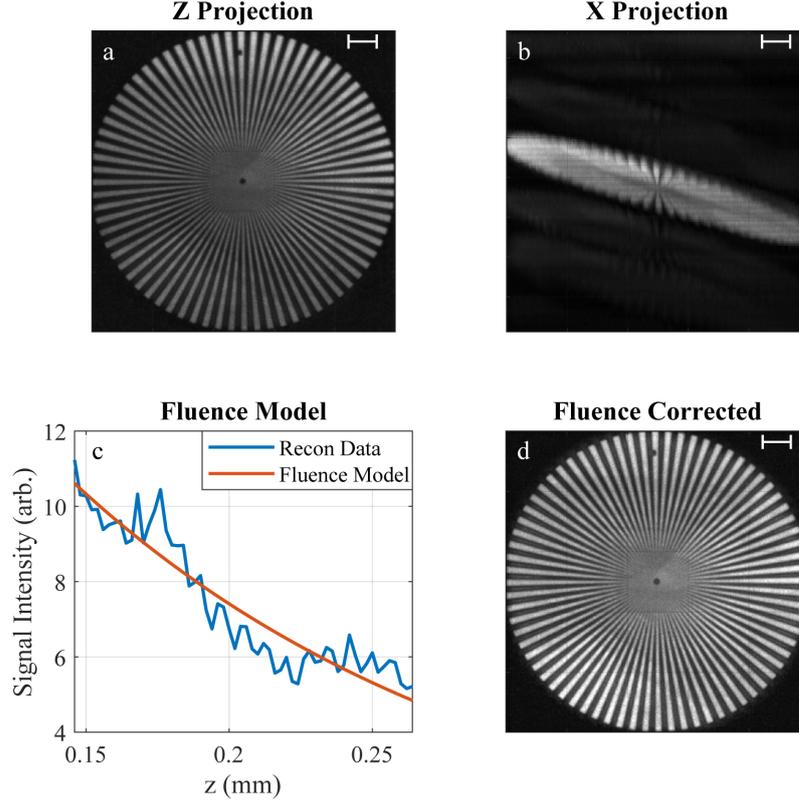
Figure 4.6: **Reconstructed image of *phantom 3* acquired using *SW-PWFD mesoscopy setup 3*.** a: Maximum intensity projection along the z axis. b: Maximum intensity projection along the x axis. c: Voxel intensity after reconstruction and threshold in the interval between $z = 150\,\mu\text{m}$ and $z = 250\,\mu\text{m}$ (blue) and exponential fit to data (orange) is illustrated. d: Maximum intensity projection from a, after fluence has been corrected by the model shown in c. Scalebar $= 1\,\text{mm}$.

Although the absorption of the phantom was homogeneous, the reconstructed optoacoustic signal was larger in the top right corner of the image than the bottom left. This was the consequence of the phantom not being exactly in the x-y plane of the imaging system (fig. 4.6b). Instead, the left side of the phantom was elevated about $100\,\mu\text{m}$ above the right side. To understand the causes for this behaviour, the intensity of a given voxel in the interval between $z = 150\,\mu\text{m}$ and $z = 250\,\mu\text{m}$

was plotted against their signal intensity. A threshold has been applied to reject noise (fig. 4.6c). An exponential fitting function has been applied to the data. This function was used as a fluence model. Figure 4.6d shows the same data presented in figure 4.6a after correction using the exponential fluence model by dividing the value of each voxel by the value provided by the exponential fit. A clear improvement in the homogeneity of the reconstructed optoacoustic signal strength, in good agreement with the actual absorption coefficient of the phantom, can be reported.

Frequency response correction in SW-PWFD mesoscopy

Wideband transducers such as the one used in *SW-PWFD mesoscopy setup 3*, typically feature a very large bandwidth, explaining the high resolution of mesoscopic images. The contribution of different frequency bands to the final image quality is not equal. Most of the signal energy is in the lower end of the spectrum. High spatial information is contained in high frequency signals. To evaluate this, the data presented in fig. 4.6d was filtered using a 15–90 MHz bandpass filters (fig. 4.7a) before reconstruction. The process was repeated using a 30–90 MHz bandpass filter (fig. 4.7b) and a 50–90 MHz bandpass filter (fig. 4.7c). The high frequency data was much sharper than the the entire spectrum shown in fig. 4.7a. Yet, the low frequency data overlays the fine structures. The cumulative signal energy of a typical optoacoustic signal from figure 4.7a was determined (fig. 4.7d). The frequency range containing 50% of the optoacoustic energy was identified as 0–35.5 MHz. Figure 4.7e shows the spectrum of the optoacoustic signal and indicates the frequency spectrum of 5–35 MHz and 35–90 MHz to be used in the color coded image (fig. 4.7f). The image combines the high signal quality presented in 4.7a with the high resolution seen in figure 4.7b and c.
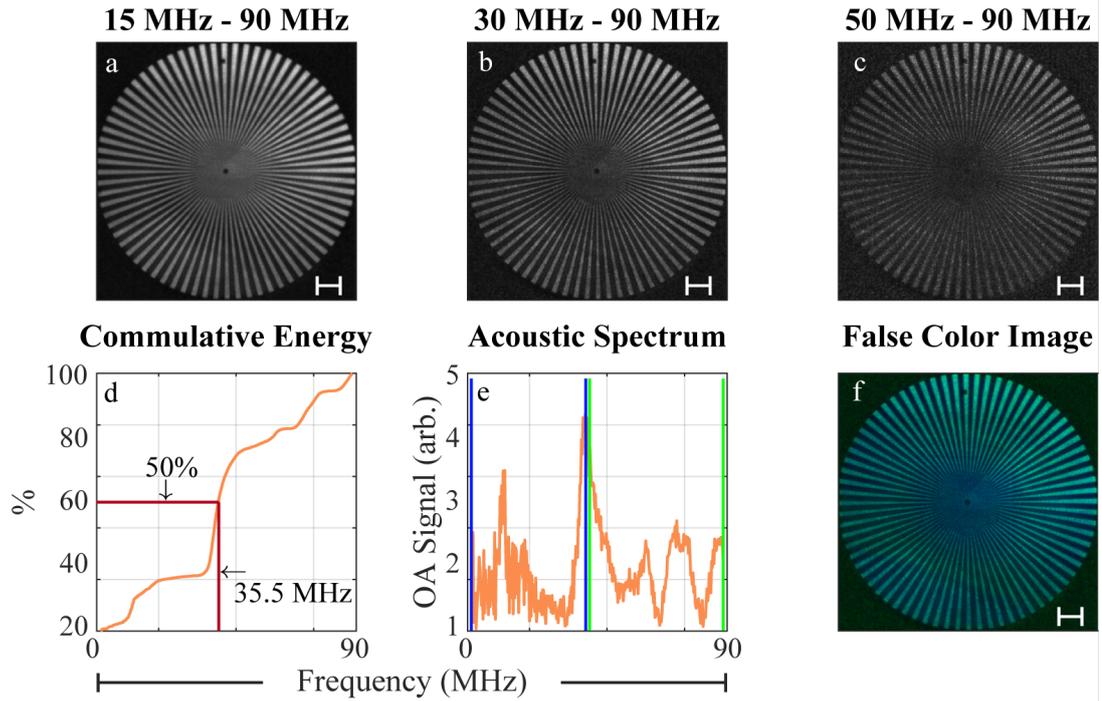
Figure 4.7: **Effect of bandwidth of optoacoustic signal on SNR and resolution demonstrated on *phantom 3* using *SW-PWFD mesoscopy setup 3*** a: Maximum intensity projection (MIP) of reconstructed data of *phantom 3* along z-axis bandpass filtered to 15–90 MHz before reconstruction. b: like a, but a 30–90 MHz bandpass filter was used. c: like a, but bandpass filtered to 50–90 MHz. d: Cumulative energy of typical optoacoustic signal taken from a before reconstruction. Frequency range that contains 50% of the optoacoustic signal is indicated. e: Same data as shown in d, but not cumulative. The frequency bands containing 50% optoacoustic energy determined in d are highlighted in blue (lower frequencies) and green (higher frequencies). f: color coded image of data presented in a, 5–35 MHz = blue, 35–90 MHz = green, combining the high SNR seen in a together with the high resolution seen in b. Scalebar = 1 mm.

Image quality evaluation as function of step size

The acquisition time in PWFD was fundamentally determined by the number of *A-scans*, the repetition rate of the pulse wave and the step size. Hence, it is important to determine the optimal values of N_{avg}, f_{rep} and δx in order to achieve the shortest possible measurement time without sacrificing image quality. To do so, a SW-PWFD mesoscopy scan of *phantom 4* using SW-PWFD mesoscopy setup 3 has been conducted. The acquired field of view was 4 mm by 4 mm, the step size used was $\delta x = 10 \, \mu m$ and the repetition rate was $f_{rep} = 200 \, kHz$. The acquired data underwent PWFD processing followed by time domain filtered back projection. and the maximum intensity projection along the z axis is determined (fig. 4.8a). Next, every second position acquired has been removed from the raw data. This yields an effective step size of 20 μm. This data underwent the same processing as

the previous set, (fig. 4.8b). The process was repeated by removing every 4th, and 5th A-scan to generate a dataset corresponding to a step size of 40 µm (fig. 4.8c) and 50 µm (fig. 4.8d).
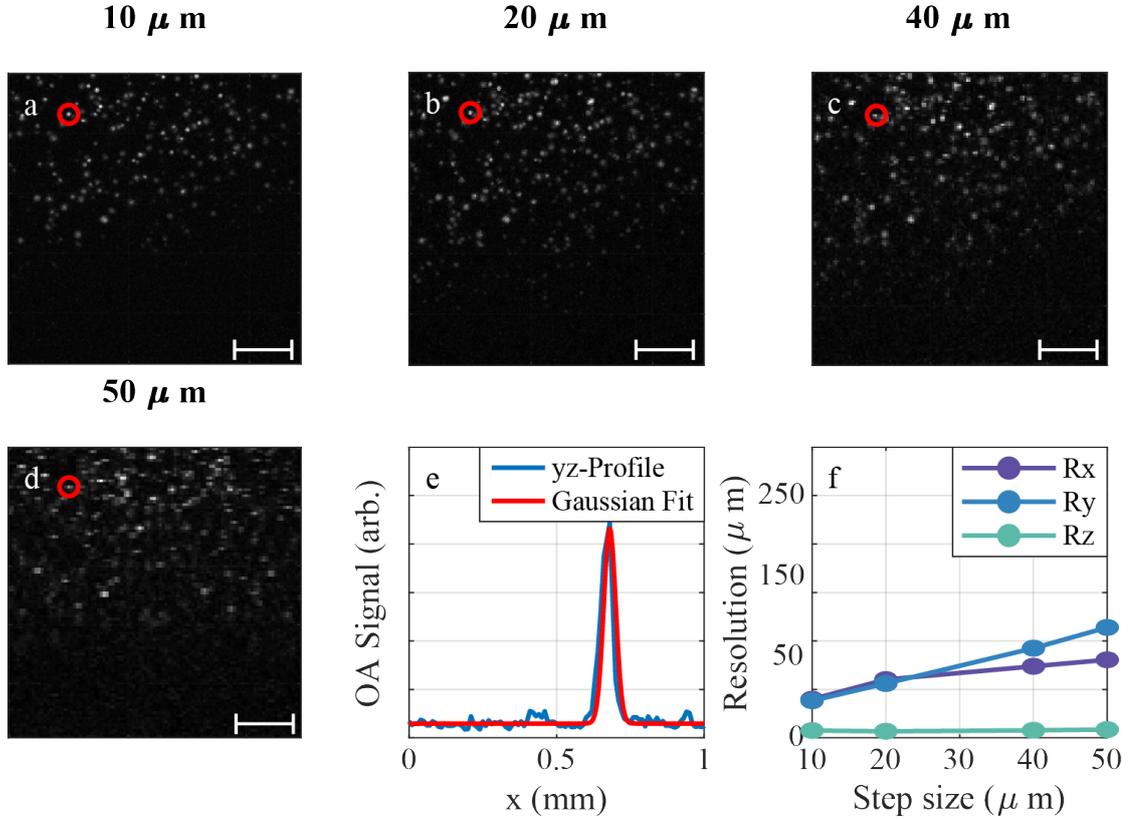
Figure 4.8: **MIP along z axis of mesocopic scan in SW-PWFD of phantom 4.** PWFD mesoscopic scan of phantom 4 simulating different step sizes, by removing projections from the acquired data before reconstruction. The resolution was determined by fitting a Gaussian function to the feature marked by the red circle. The resulting FWHM resolution in the x, y and z direction is shown on the bottom right. Scalebar = 1 mm.

To quantify the achievable resolution as a function of the step size, a point yielding a high SNR (marked in figure 4.8 by the red circle) was selected. A cut in the x, y and z direction has been made through the point and a Gaussian function has been fitted to the resulting data. This process (along x) is shown in figure 4.8e. The dependency between step size and resolution in the x, y and z direction has been determined (fig. 4.8f).

The z resolution shows continuously high values of 10 µm, which compares favourably to the theoretical limit of $\delta_z = v_s/Fs = 1500\,\mathrm{m\,s^{-1}}/200\,\mathrm{MS\,s^{-1}} = 7.5\,\mu\mathrm{m}$. In the x and y direction, some dependency between the step size and resolution has been found. Up to 20 µm, the same values for R_y and R_x are found. For larger step sizes, R_x deteriorates compared to R_y. This may be due to motion artefacts, since the stages were moving in the R_x direction during acquisition. In conclusion, any increase in step size beyond the feasible minimum of 10 µm results in a decrease in

resolution. Therefore, for the following measurements, the step size was chosen to be 10 μm and the resulting, relative large acquisition times were accepted.

Image quality evaluation in SW-PWFD as function of number of averages

All procedures with animals and humans were approved by the District Government of Upper Bavaria. Data acquired with assistance from Antonio Stylogiannis.

The number of averages is one of the main factors that dictate the image quality and the acquisition time. To determine the ideal number of averages, a mesoscopic scan using *SW-PWFD mesoscopy setup 3* on the right forearm of volunteer 1 using the *skin positioning setup* described in section 3.10 was conducted. The chosen field of view was 4 mm by 4 mm to keep the measurement time short and minimize motion artefacts. The repetition rate was $f_{rep} = 200$ kHz and 100 pulses per projection were acquired. Unlike in the measurement previously presented, the acquired raw data was not processed using the PWFD algorithm immediately. Instead, the raw data was saved on a fast solid state disk (tab. 3.1). After the scan has been completed, N_{avg} pulses of the raw data have been passed on to the PWFD algorithm. The resulting data underwent filtered back-projection reconstruction and the fluence correction model (fig. 4.6) has been applied. To understand the effect of the number of averages or deposited energy on the image quality, images were constructed using different values of N_{avg} varying between 10 and 100 averages (fig. 4.9a-f).

Previous measurements have shown that color coding different acoustic frequency bands allows to enhance the resolution of the reconstructed data while maintaining a high SNR (fig. 4.7). Therefore, the raw data was split in two frequency spectra before reconstruction, 5–35 MHz in blue, 35–70 MHz in green (fig. 4.9). The deposited energy corresponds to the pulse energy (assumed to be 200 nJ) multiplied by N_{avg}. To quantify the image quality as a function of E_{dep}, the resolution achievable at a given depth below the skin surface has been calculated for each image. This was done by identifying a blood vessel at the lower end of the image and identifying its full width half maximum along the z axis, in the same way the resolution was calculated in section 4.8. This was done for the low and the high frequency band (fig. 4.10a). The contrast to noise ratio (CNR) of the reconstructed data has been calculated. The noise of the image by calculating the standard deviation of the area located above the skin. The maximum signal was calculated by finding the highest peak -to-peak value over the entire image. This was done for both the low frequency and the high frequency spectra (fig. 4.10b). The data does not support a strong relationship between N_{avg} and the resulting resolution. Hence, high resolution imaging can also be performed with a low number of averages. The presented CNR data shows a square-root trend as already known from data presented in figure 4.3 - 4.4. Therefore, a high number of averages enables high contrast imaging. The exact number of averages must be picked for each application, depending on its optical properties. For *in vivo* samples, N_{avg} was chosen to be 100.
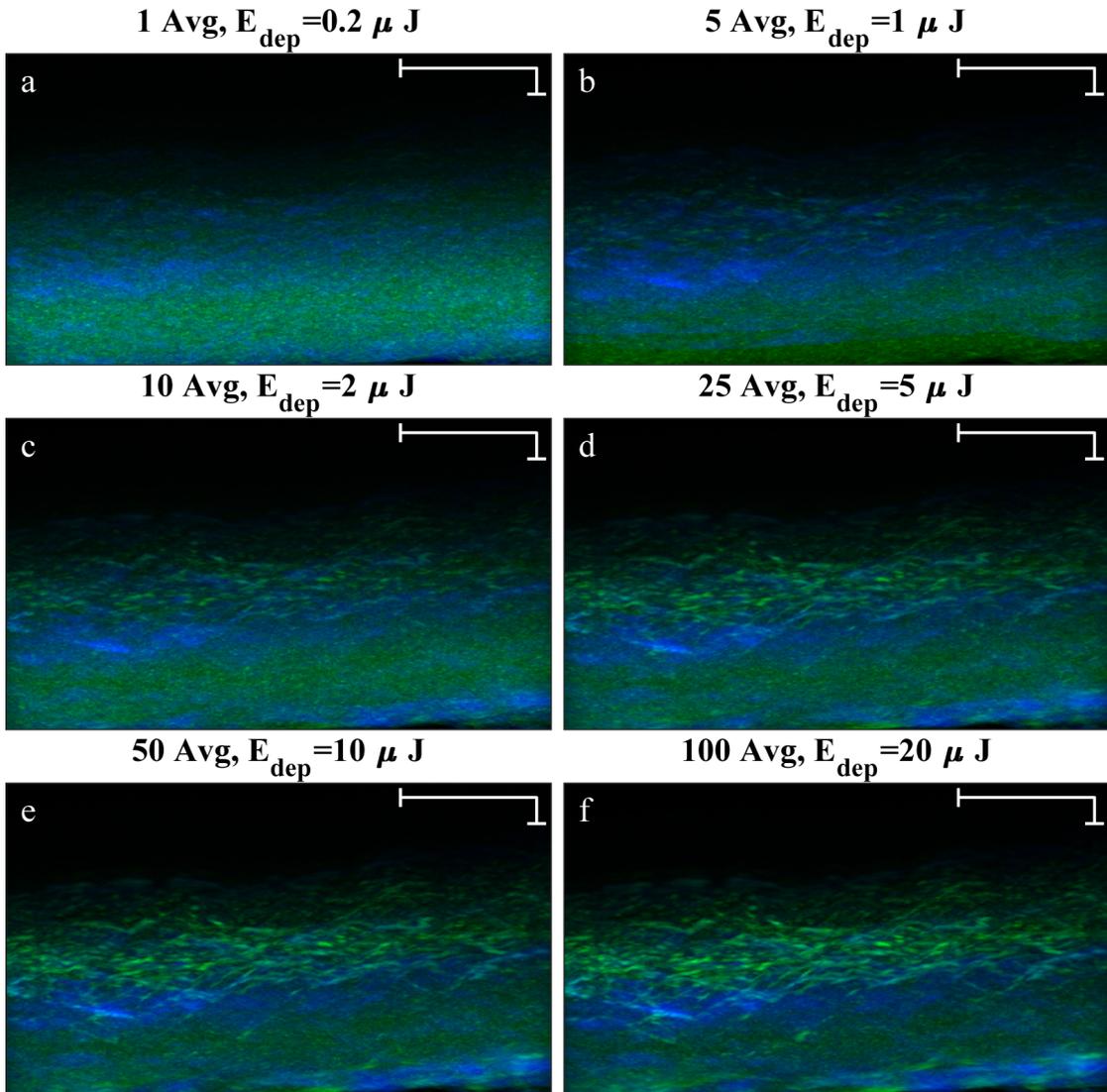
Figure 4.9: **SW-PWFD mesoscopic scan of right forearm of volunteer 1 using different numbers of averages / deposited energies.** a: after 1 averages, only the bulk of the skin generates detectable signals. b: 5 averages reveal small vasculature in high frequencies. c,d: The vessels become more pronounced after 10 and 25 averages, while the low frequency data shifts to lower skin layers. e: After 50 averages, no substantial increase in the upper skin layers is observed. f: further structures in lower layers become visible at 100 averages. Before reconstruction, the signal was separated into two frequency spectra. 5–35 MHz is shown in blue, 35–70 MHz is shown in green. Vertical scale bar: 100 µm, horizontal scale bar: 1 mm
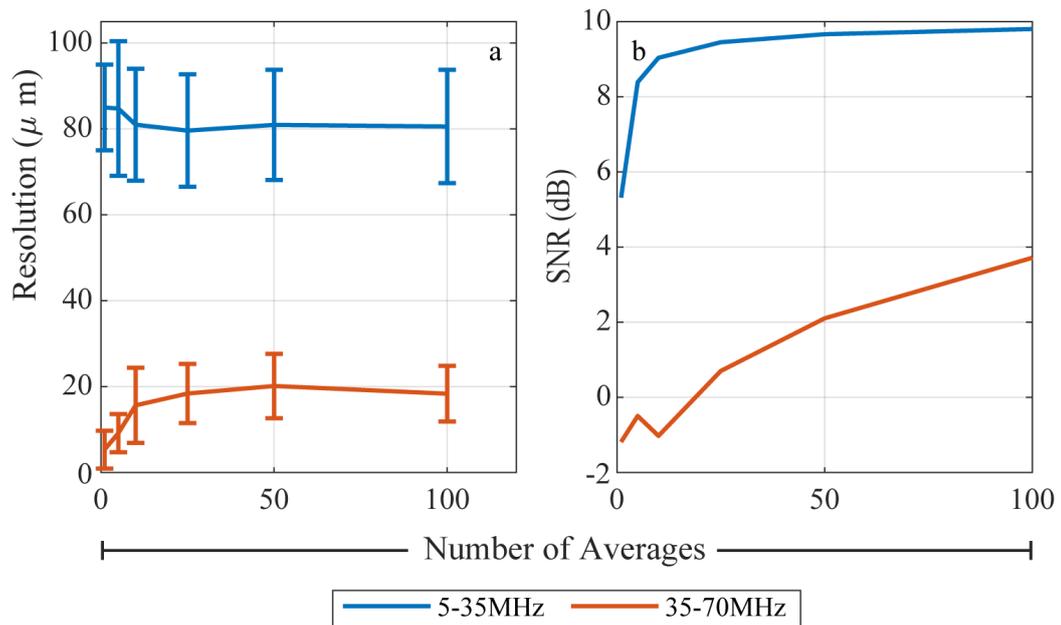
Figure 4.10: **CNR and resolution achievable in human skin for different number of averages.** Left: FWHM of small blood vessel identified below surface for different number of averages / deposited energy. Data is shown for both frequency spectra. Right: Contrast to noise ratio for both frequency bands as function of deposited energy.

4.3 Evaluation of MS-PWFD mesoscopy

It has been demonstrated that PWFD and PWTD are equivalent in terms of depth of field and achievable SNR. Unlike PWTD, PWFD allows for frequency multiplexing. Using several light sources modulated to different repetition rates, the optoacoustic response from each laser can be measured simultaneously. Hence, multispectal imaging without any reduction in acquisition time is possible. The performance is evaluated in the upcoming section.

Introduction to MS-PWFD mesoscopy

The data presented in figure 4.11 was acquired by Antonio Stylogiannis under the authors supervision.

To illustrate the principle of *MS-PWFD Mesoscopy Setup 4* was used to acquire a signal from *phantom 2*. No raster scan was performed during this measurement. The repetition rate of the four lasers were set to $200\,\text{kHz}$, $200.125\,\text{kHz}$, $200.25\,\text{kHz}$ and $200.375\,\text{kHz}$, respectively, corresponding to $f_{0,\lambda} = 200\,\text{kHz}$ and $\Delta f = 125\,\text{Hz}$. This repetition rates were used for all MS-PWFD measurements presented in this thesis. The raw data acquired during this measurement has been saved and Fourier transformed (fig. 4.11a). Furthermore, the digital demodulation algorithm described in section 2.10 has been used to extract the frequency components of the four excitation lasers. The frequency components for a small interval of 20–$25\,\text{MHz}$ are also shown in figure 4.11a. Only the frequency components of the first laser fell exactly on the Fourier transform of the raw data, because the repetition rate of the other three lasers did not match a whole divider of the sampling rate. The odd repetition rates of the other three lasers introduces non-periodic artefacts to the signal making the fast Fourier transform unsuitable to extract frequency components in MS-PWFD. Furthermore, the inverse Fourier transform of each signal has been calculated (fig. 4.11 b-e) to show that waveform corresponding to the optoacoustic signal generated by each leaser independently could be reconstructed.
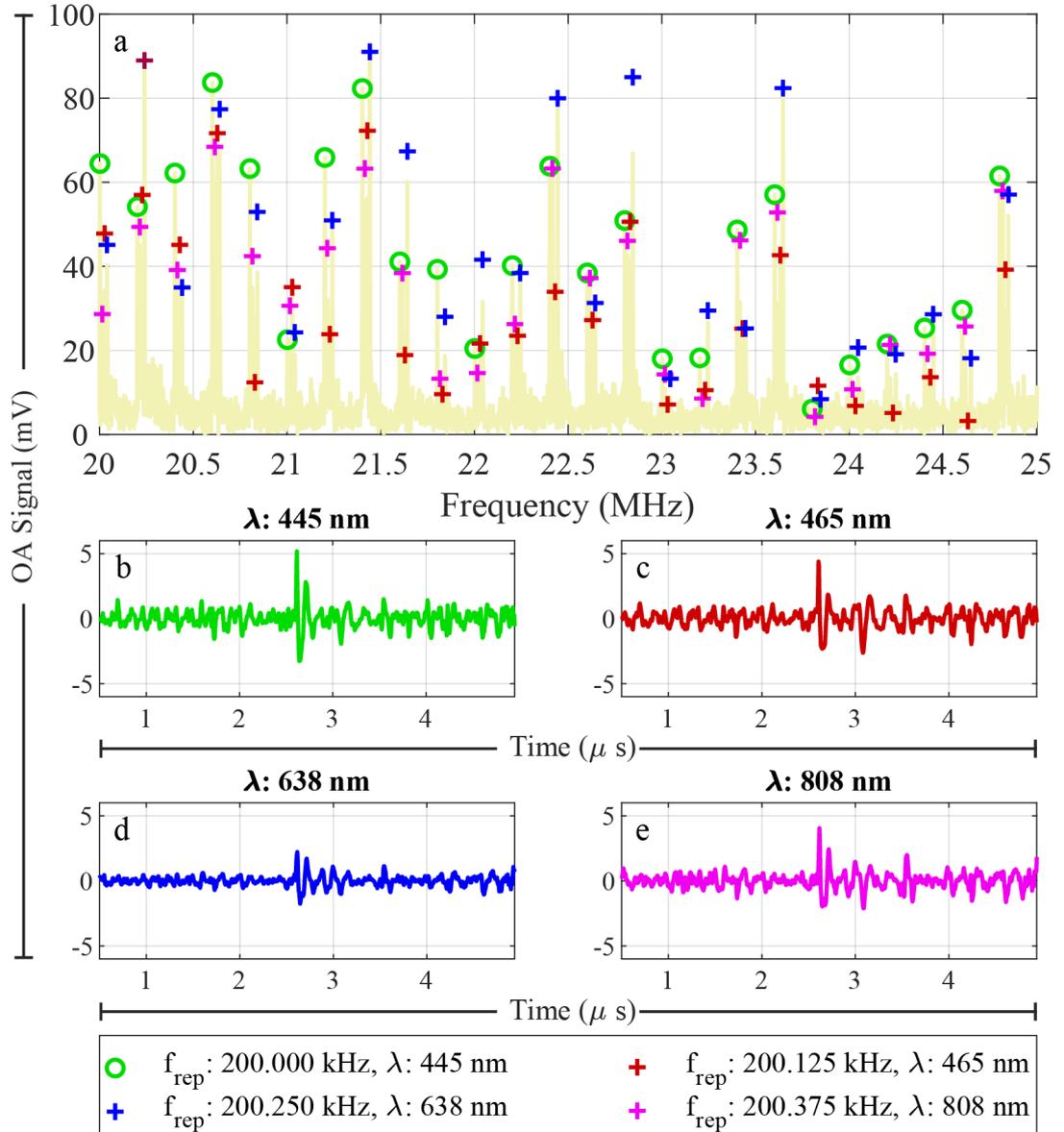
Figure 4.11: **Raw spectra of MS-PWFD with extracted frequency components utilizing four lasers.** a: Acquired raw data together with frequency components extracted by digital demodulation. b-e: Inverse Fourier transformation of each set of frequency components.

Resolution of MS-PWFD mesoscopy

To determine the resolution of *MS-PWFD Mesoscopy Setup 4, phantom 3* was scanned over a field of view of 4 mm and acquiring 100 averages. The frequency data for each laser was extracted, inverse Fourier transformed and the back-projection algorithm was applied (fig. 4.12a-d). One microsphere yielding a strong optoacoustic signal was identified, and the resolution of the system in x, y and z direction for each laser was determined as shown in figure 4.8. The microsphere under investigation is marked with a red circle. Figure 4.12e-f shows the achieved resolution using the circled microsphere for each laser along the x direction. Figure4.12i-l shows the same along the y, and finally figure 4.12m-p along the z direction. Similar resolution are achievable as in MS-PWFD for all utilized lasers than in SW-PWFD when using only one laser.

Evaluation of of human skin imaging using MS-PWFD mesoscopy

All procedures with animals and humans were approved by the District Government of Upper Bavaria. Data acquired with assistance from Alice Solda and Antonio Stylogiannis.

The skin of the right lower arm of volunteer 2 was scanned over a field of view of 4 mm by 4 mm using $\delta x = 10\,\mu m$, $f_{0,\lambda} = 200\,kHz$, $\Delta f = 125\,Hz$ and $N_{avg} = 100$. The frequency components of each laser is extracted and reconstructed using back-projection (fig. 4.13). The high and low frequency data presented in figure 4.13a-b have been added together with a weighting factor, increasing the weight of high frequencies. The maximum intensity projection along the sagittal plane has been calculated (fig. 4.7). Detailed morphology is visible at 445 nm (fig. 4.13a) and 465 nm (fig. 4.13b). Furthermore, high frequencies are dominant in the upper skin layers, while low frequencies originate from low layers. Little useful information is presented in figure 4.13c at 638 nm and 4.13d 808 nm. Since most information is available at 445 nm and 465 nm, the images at these two wavelength are color coded in a false color image. The data acquired at 445 nm is coded in red and the data acquired at 465 nm is encoded in green

Different projections of the acquired data is shown in figure 4.14. The sagittal view shows that the upper layers of the skin are highly absorbing at 445 nm, while lower layers including small blood vessels are more strongly absorbing at 465 nm (fig. 4.14a). Projecting the data transverse reveals further skin structures. In the upper region covering -360–$-60\,\mu m$ below the focus plane of the transducer, the morphology of superficial skin layers can be visualized (fig. 4.14c). In the deeper layers of -60–$570\,\mu m$, small blood vessels can be seen. Furthermore, variations in absorption between 445 nm and 465 nm are apparent, which may indicate fluctuations in the oxygen saturation of the hemoglobin within the vessels (fig. 4.14d).
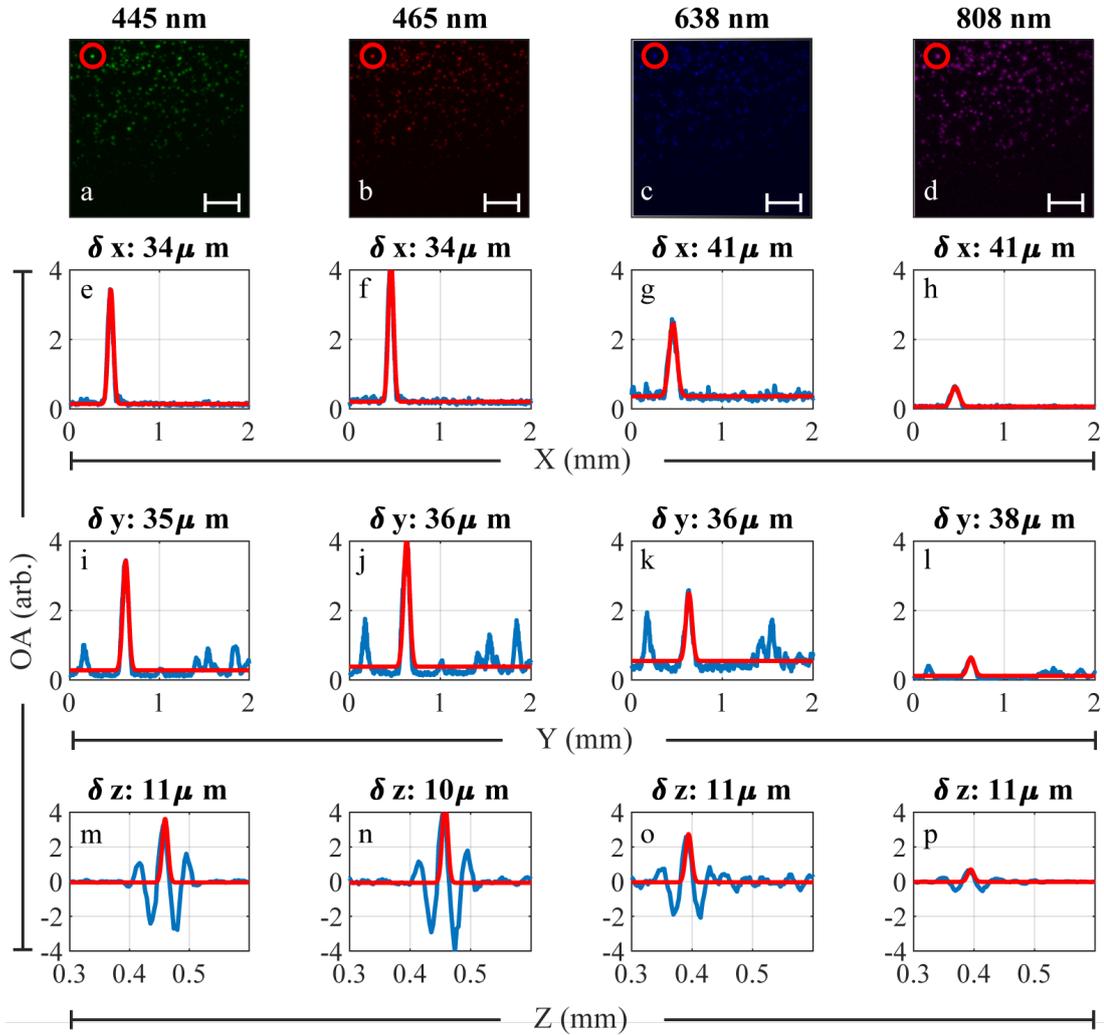
Figure 4.12: **Resolution of MS-PWFD evaluated using *MS-PWFD Mesoscopy Setup 4* on *phantom 3*.** a-d: MIP along the z axis of the reconstructed scan of each laser used to scan phantom 3 in MS-PWFD. e-h: Resolution in x direction of each laser in MS-PWFD. i-l: Resolution in y direction of each laser in MS-PWFD. m-p: Resolution in z direction of each laser in MS-PWFD. Scalebar: 1 mm.
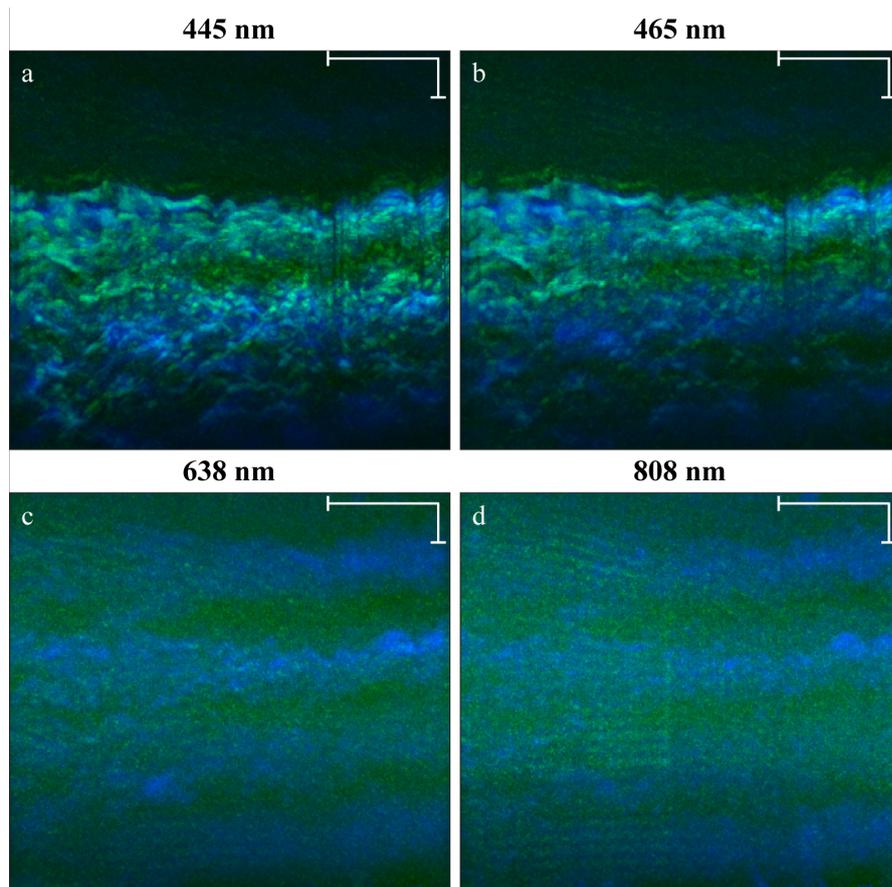
Figure 4.13: [**MIP of skin of volunteer 2 acquired using *MS-PWFD Mesoscopy Setup 4* at different wavelengths.** Skin acquired using the respective laser wavelength. Acoustic frequencies in the range of 5–35 MHz encoded in blue, frequencies in the range of 35–70 MHz encoded in green. Vertical scale bar: 100 µm, horizontal scale bar: 1 mm.

95
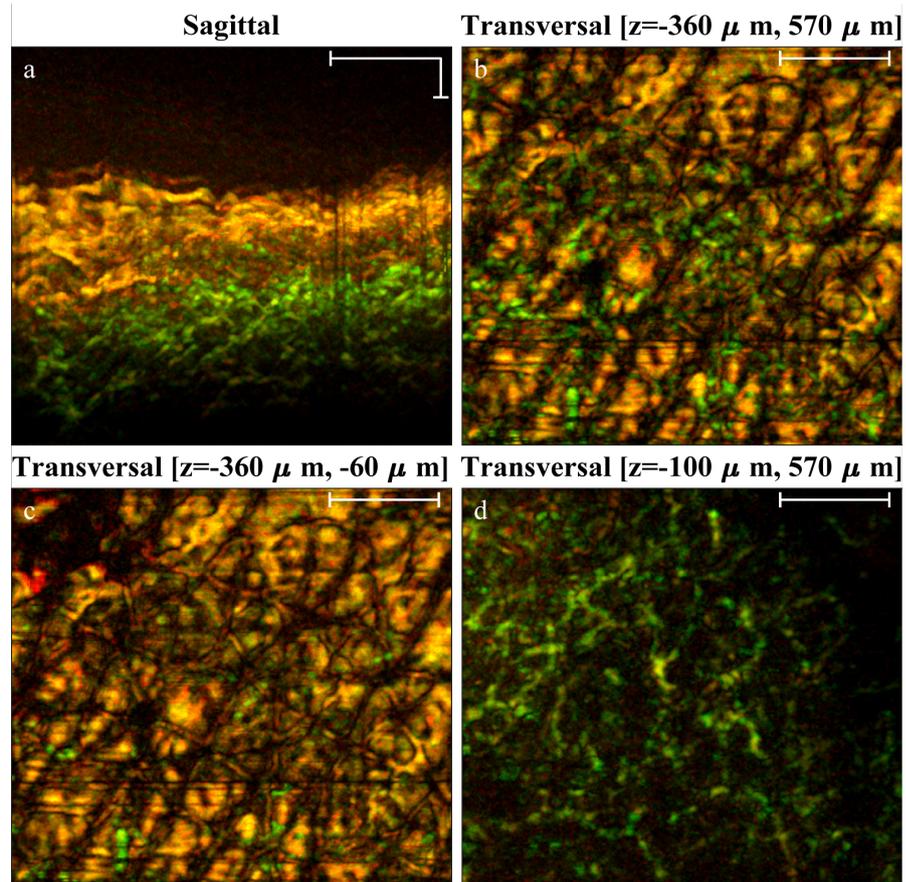
Figure 4.14: **False color overlay of two wavelength of skin of volunteer acquired using *MS-PWFD Mesoscopy Setup 4*.** False color overlay of the 445 nm (red) and 465 nm (green) laser. a: sagittal MIP through the entire skin. b: transverse MIP of the same data. c: transverse MIP of upper skin layers, resolving skin morphology. d: transverse MIP of lower skin layers, showing vascular structure. Vertical scale bar: 100 µm, horizontal scale bar: 1 mm.

Evaluation of medical applications of MS-PWFD mesoscopy

Optoacoustic mesocopy has demonstrated usefulness in clinical settings. To do this, MS-PWFD must provide reproducible results. A scan of the right lower arm of six healthy volunteers was conducted. The age and gender of the volunteers is listed in table 3.7. A field of view of 4 mm by 2 mm was scanned at each volunteer using the *MS-PWFD mesoscopy setup 4*. The resulting data of each laser was reconstructed using the time domain filtered back projection algorithm. The data acquired at 445 nm and 465 nm was used to generate a false color map of the skin. The MIP of this false color map along the y axis for each volunteer is shown in figure 4.15.
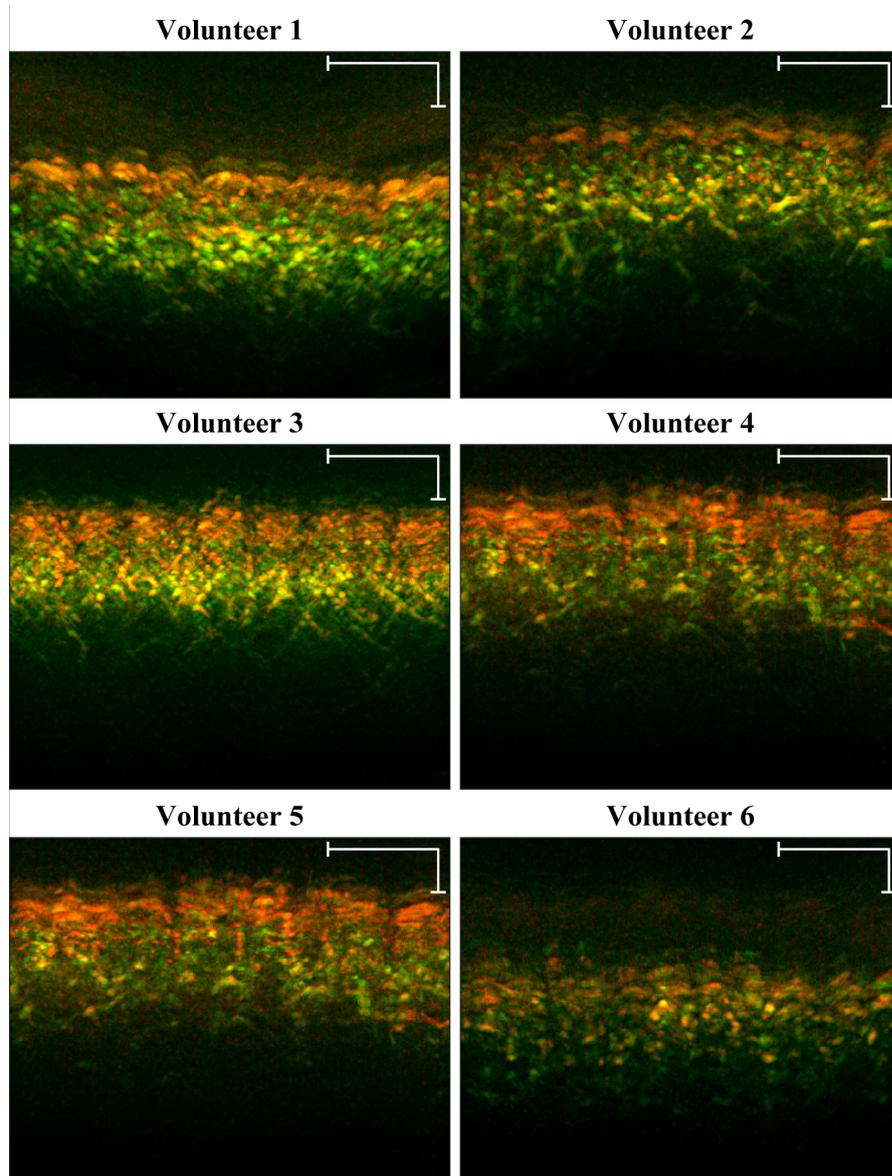
Figure 4.15: **MS-PWFD scan of skin on lower right arm of six different volunteers.** The data acquired at 445 nm and 465 nm have been color coded so that green reflects the intensity of 445 nm and red that of 465 nm. Vertical scale bar: 100 µm, horizontal scale bar: 1 mm.

4.4 Visibility study of common contrast agents

All procedures with animals and humans were approved by the District Government of Upper Bavaria. Data acquired with assistance from Antonio Stylogiannis and Uwe Klemm.

An important tool for biological applications is the visualization of contrast agents. They allow to label biological and physiological processes within the model organism. The ability to image these contrast agents at high spatial resolution allows conclusions about the underlying biological process to be drawn. A vast number of contrast agents has been developed for various applications. The presented system is able to visualize absorption optoacoustically at four different wavelengths. Two are in the blue part of the visible spectrum (445 nm and 465 nm) and are useful to monitor oxygenation in small blood vessels. The other two wavelengths lie in the far red (638 nm) and near infra-red (808 nm). At these wavelengths, the absorption of biological chromophores is very low compared, yet numerous contrast agents are available with strong absorption in this wavelength region as discussed in section 1.3. Therefore, three contrast agents Alexa Fluor 780, DiD and Indocyanine green (ICG) have been selected as they are most absorbing in the range of 650–850 nm. They can be imaged at great penetration depth and at the same time feature little background from biological chromophores.

To understand if contrast agents provide sufficient SNR to be detected at high resolution within the model organism, their absorption was studied using a microfluidic chips, as small vessel mimicking phantom. To study the suitability of TOPAS covered microfluidic chips as phantoms for mesoscopic imaging, a hole with approximately 5 mm diameter was punched in a sheet of 145 µm thick TOPAS foil. Next, a 10 µm thick nylon suture was spanned across the hole. The sheet was than suspended 5 mm above the bottom of a Petri dish, with the suture facing down (fig. 4.16a). This way, part of the suture was visible from the top through the TOPAS foil while another part was visible through the hole. A black marker was used to mark the position of the hole. The Petri dish was filled with water for acoustic coupling, and a SW-PWFD mesoscopic scan was conducted over a region that includes the suture covered by TOPAS and suture not covered by TOPAS.

The acquired data of the suture was split into two regions, with TOPAS and without TOPAS and bandpass filtered to 10–90 MHz. The signals along the suture in each region were averaged to create a higher SNR signal (fig. 4.16b). Assuming that no excitation light is absorbed by the TOPAS, some of the created ultrasound is absorbed by TOPAS. In addition, TOPAS features a higher speed of sound than water, therefore the ultrasound traveling through TOPAS arrived earlier than the ultrasound traveling through water only. Subsequently, a fast Fourier transformation of the presented data has been conducted (fig. 4.16c). The attenuation of the TOPAS increase with frequency. The frequency dependent attenuation could be calculated by dividing the two curves (fig. 4.16d). For frequencies below 30 MHz, the attenuation was relatively constant at −2 dB, yet it increased to −7 dB at 90 MHz.

In conclusion, low frequencies generated by larger objects were less affected by TOPAS than high frequencies created by small objects. Therefore, the size of
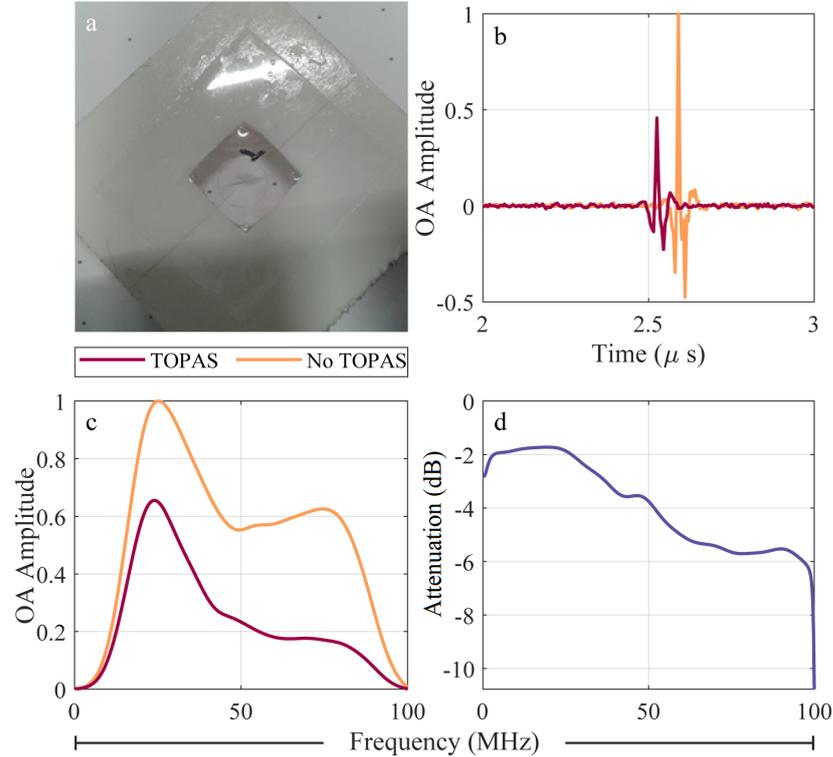
Figure 4.16: **Effect of a** $145\,\mu m$ **thick layer of TOPAS on optoacoustic signal in PWFD.** a: Optoacoustic response of $10\,\mu m$ nylon suture when covered (red) and not covered (yellow) by TOPAS layer. b: Frequency spectrum of a. Frequency dependent attenuation by comparing the frequency response in b.

the channel in the microfluidic chip was chosen as big as feasible. This way, more ultrasound was generated in lower frequencies that suffer less attenuation. This is why for the subsequent experiments, a microfluidic chip with $100\,\mu m$ channel size was chosen.

The contrast agents of interest were injected into the microfluidic chip. Next, the chip was mounted inside a Petri dish with the TOPAS foil facing towards the imaging system. Reference marks were applied to the TOPAS layer using a waterproof red marker, since it is expected to be visible at $445\,nm$ and $465\,nm$, but not effect the measurement at $638\,nm$ and $808\,nm$. The microfluidic chip was submerged in distilled water for acoustic coupling and a MS-PWFD mesoscopic scan was conducted of each channel containing a different contrast agent. The resulting data was reconstructed using the back-projection algorithm (fig. 4.17).

The optoacoustic spectrum of Alexa Fluor 780 shows a distinct peak at $808\,nm$, while a small increase in absorption is visible at $445\,nm$ (fig. 4.18a-d). DiD features measurable absorption at $638\,nm$ only, which falls short of the Alexa Fluor 780 absorption (fig. 4.18e-h). Finally, ICG features weak absorption at all wavelength, but does yield an obtainable signal at $445\,nm$ and $808\,nm$ (fig. 4.18i-l). The acquired optoacoustic absorption measurements were compared with literature
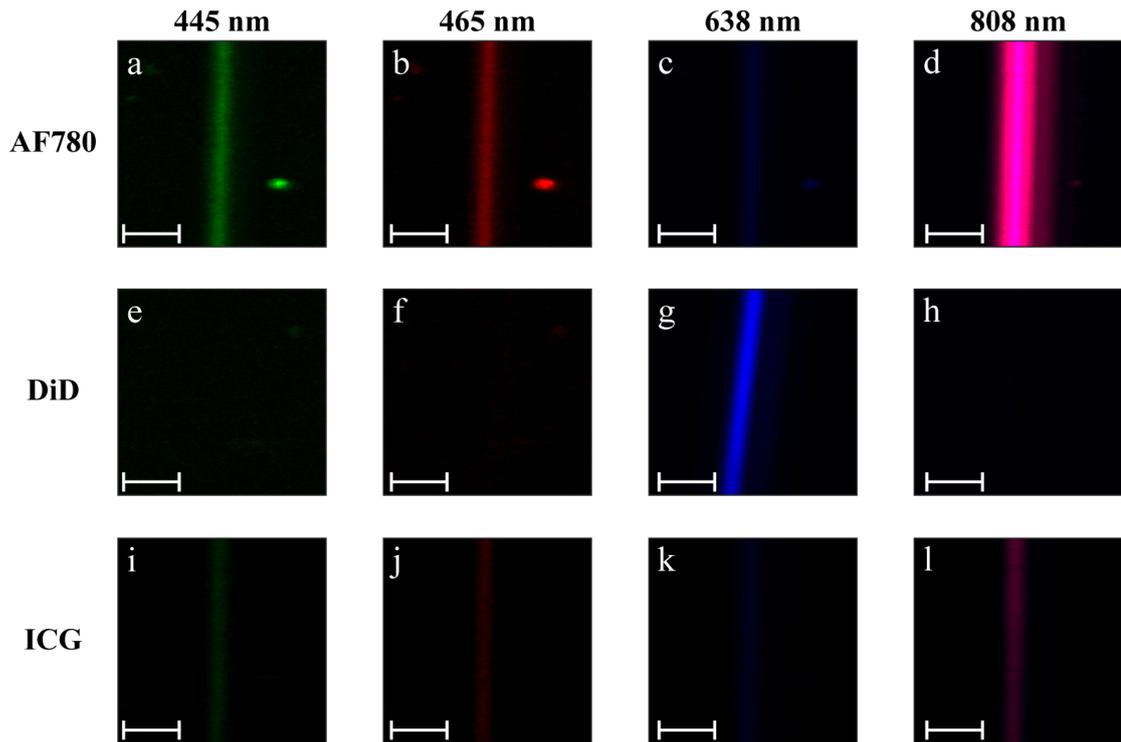
Figure 4.17: **Optoacoustic response in MS-PWFD of common fluorescent and non fluorescent dies measured in microfluidic chip.** Top row: optoacoustic response of Alexa Fluor 780 at the four measurement wavelength. Middle row: optoacoustic signal of DID, bottom row: optoacoustic signal of ICG. Scale bar: 1 mm.

values. An excellent agreement for Alexa Fluor 780 can be reported (fig. 4.18, left). Unfortunately, literature data was not available for all wavelength for DiD and ICG. For the available data, DiD shows good agreement (fig. 4.18, center). The measured data of ICG however, does not feature the literature data at 638 nm and 808 nm (fig. 4.18, right).
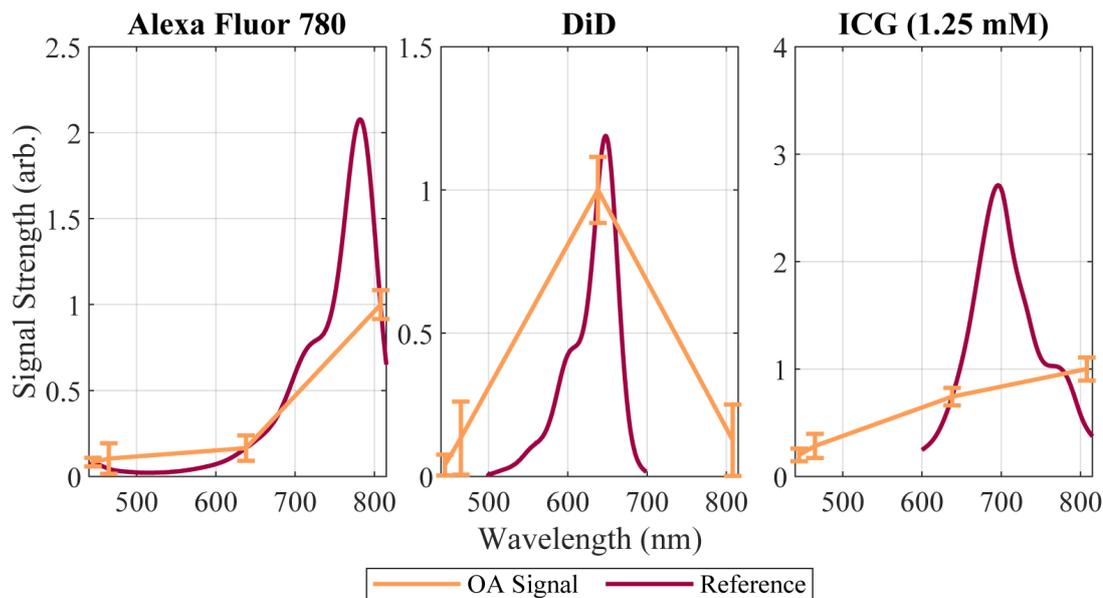
Figure 4.18: **Spectral optoacoustic response in MS-PWFD of common contrast agents.** Measured optoacoustic response was overlayed with literature values of the absorption (when available). Error bars correspond to one standard deviation of noise in image.

4.5 Perfusion measurement of micro vasculature using ICG

Changes in blood perfusion in small vessels is a key symptom to vessel degenerative diseases such as diabetes and arteriosclerosis [192–195]. ICG injections are an established method to examine the perfusion in clinical contexts. This section will show the suitability of ICG injections to visualize perfusion of small vessels, demonstrated in the ear of a CD-1 mouse using MS-PWFD mesoscopy.

The mouse was prepared as described in section 3.10. A multispectral mesoscopic scan of 4 mm by 4 mm was conducted, which covered a part of the mouse ear including vessels of different sizes. The small field of view was chosen to ensure the scan time was lower than the circulation half life of ICG. The raw data was reconstructed using the back-projection algorithm (fig. 4.19a-d). A cross section of figure 4.19d along the purple line is shown in 4.19e. Due to the high absorption of hemoglobin at 445 nm and 465 nm, the vasculature is well visible at these wavelengths. No significant features are visible in figure 4.19e. As the hemoglobin absorption drops steeply after 600 nm, no signal could be recovered at 638 nm and 808 nm.

Immediately after completion of the previous scan, the same scan was initialized again. After about 15 s of scan time, 15 µL of ICG solution with a concentration of 5 mg of ICG per mL, equal to 75 µg were injected into the animals tail vein. The scan was completed and processed the same way as the previous scan. The results have been visualized in figure 4.19f-i. Again, a cross sectional cut along the purple line in figure 4.19i is shown in 4.19j. While the vasculature is still well visible at
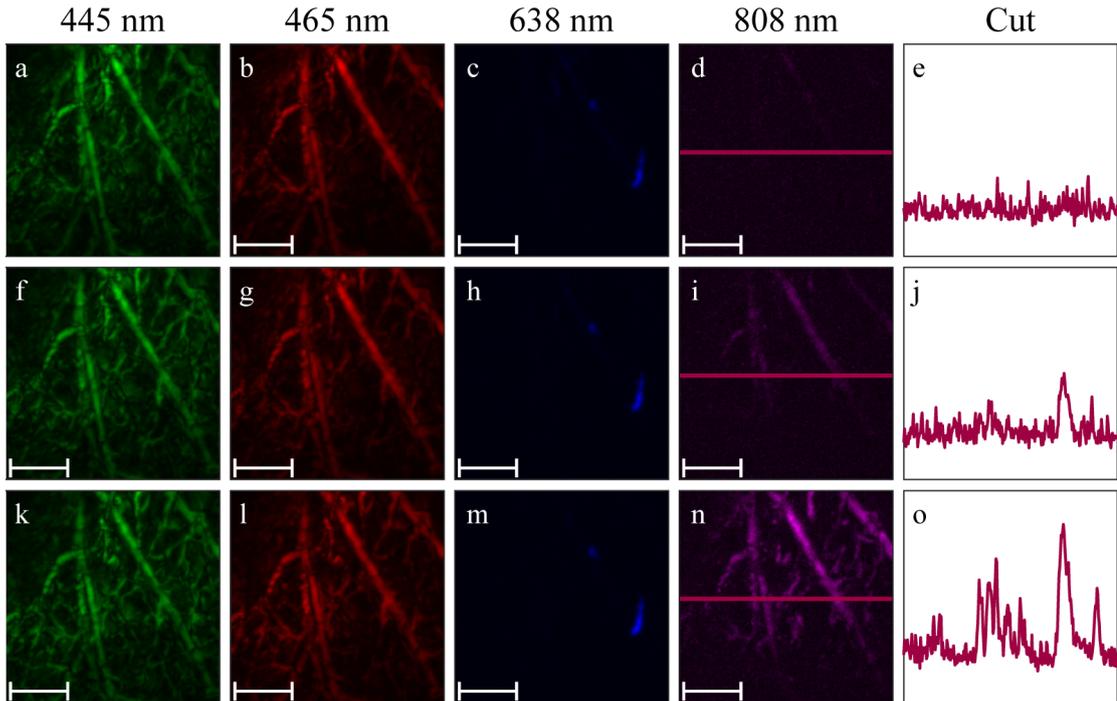
Figure 4.19: **MS-PWFD scan of mouse ear before and after intravenous injection of ICG.** a-d: Reconstructed images at four wavelength of MS-PWFD scan before ICG was injected. f-i: MS-PWFD scan after were 75 μg of ICG was injected. k-n: MS-PWFD scan after were 250 μg of ICG was injected. e,j,o: cross section along line shown in 808 nm image. Scale bar: 1 mm. The smallest vessel visualized with ICG is measured to be 72 μm (FWHM).

445 nm and 465 nm, the ICG is generating a measurable signal within the larger vessels at 808 nm, which is close to its peak absorption wavelength of ICG. No signal change is apparent at 638 nm.

The mouse was kept under anaesthesia for further 10 minutes, to ensure all ICG has decomposed. Then, another mesoscopic scan with the same scan parameters was started. After another 15 s, 50 μL of ICG solution equal to 250 μg were administered to through the tail vein. The scan was completed and processed, the results are presented in figure 4.19k-n. The cross sectional cut along the purple line in figure 4.19n is shown in 4.19o. Similar as to the previous measurements, the blood vessels can be visualized in the 445 nm and 465 nm channel and no signal from the vasculature is apparent at 638 nm. At 808 nm, the signal strength has increased to a point were small vessels can identified and hence monitored for their perfusion.

4.6 Blood oxygenation in small vessels using MS-PWFD

All procedures with animals and humans were approved by the District Government of Upper Bavaria. Data acquired with assistance from Antonio Stylogiannis and Uwe Klemm.

Besides the ability to monitor functional processes through imaging contrast agents *in vivo*, the presented MS-PWFD system provides wavelength appropriate for hemoglobin imaging. Oxygenated and non-oxygenated hemoglobin do not share the same spectral properties. The available wavelength 445 nm and 465 nm are not only strongly absorbed by hemoglobin, but the ratio of absorption of the two wavelength differ significantly for oxygenated and deoxygenated blood. Hence, by comparing the absorption of the two wavelength, the oxygen saturation of the blood within a vessel can be estimated. Combined with the ability to detect contrast agents at other wavelength, this provides the novel possibility to correlate metabolic and functional processes *in vivo* simultaneously at unprecedented resolution.

A CD1 mouse was anaesthetised and placed in the mouse holder as explained in section 3.10. Next, a MS-PWFD scan over 10 mm by 10 mm field of view of the mouse ear was conducted at $\delta x = 10 \, \mu m$, $f_{0,\lambda} = 200 \, kHz$, $\Delta f = 125 \, Hz$ and $N_{avg} = 100$. The acquired data was reconstructed using back-projection (fig. 4.20a-d). A false color overlay of figure 4.20a and 4.20b is shown in 4.20i. 445 nm is represented by red and the absorption at 465 nm by green. A cross section along the purple line shown in figure 4.20i for each laser has been acquired and is shown in 4.20k.

Subsequently, the animal was euthanized using an overdose of Ketamin/ Xylazin. The substance is not expected to change to optical properties of hemoglobin. After five minutes, another mesoscopic scan of the mouse ear was conducted. As the animal is now dead, the blood in its vessels is expected to be fully deoxygenated. The data is again processed using back projection and is shown in figure 4.20e-h. The images in figure 4.20e and 4.20f were used to create a false color overlay, were the absorption at 445 nm is represented by red and the absorption at 465 nm by green. The images are presented in the bottom half of figure 4.20j. The cross section along the purple line shown in figure 4.20j is presented in 4.20l.

In a mouse ear, arteries carrying oxygen rich blood and veins containing oxygen depleted blood usually run in parallel. Such structures can easily be identified in the presented data. *In vivo*, the absorption of arteries and veins are expected to differ at the two wavelength. This is represented by them having different colors in the false color image. After euthanization, the absorption is expected to be equal in all vessels, hence they should all have the same color. This is what is seen in the *ex vivo* image presented in figure 4.20j.
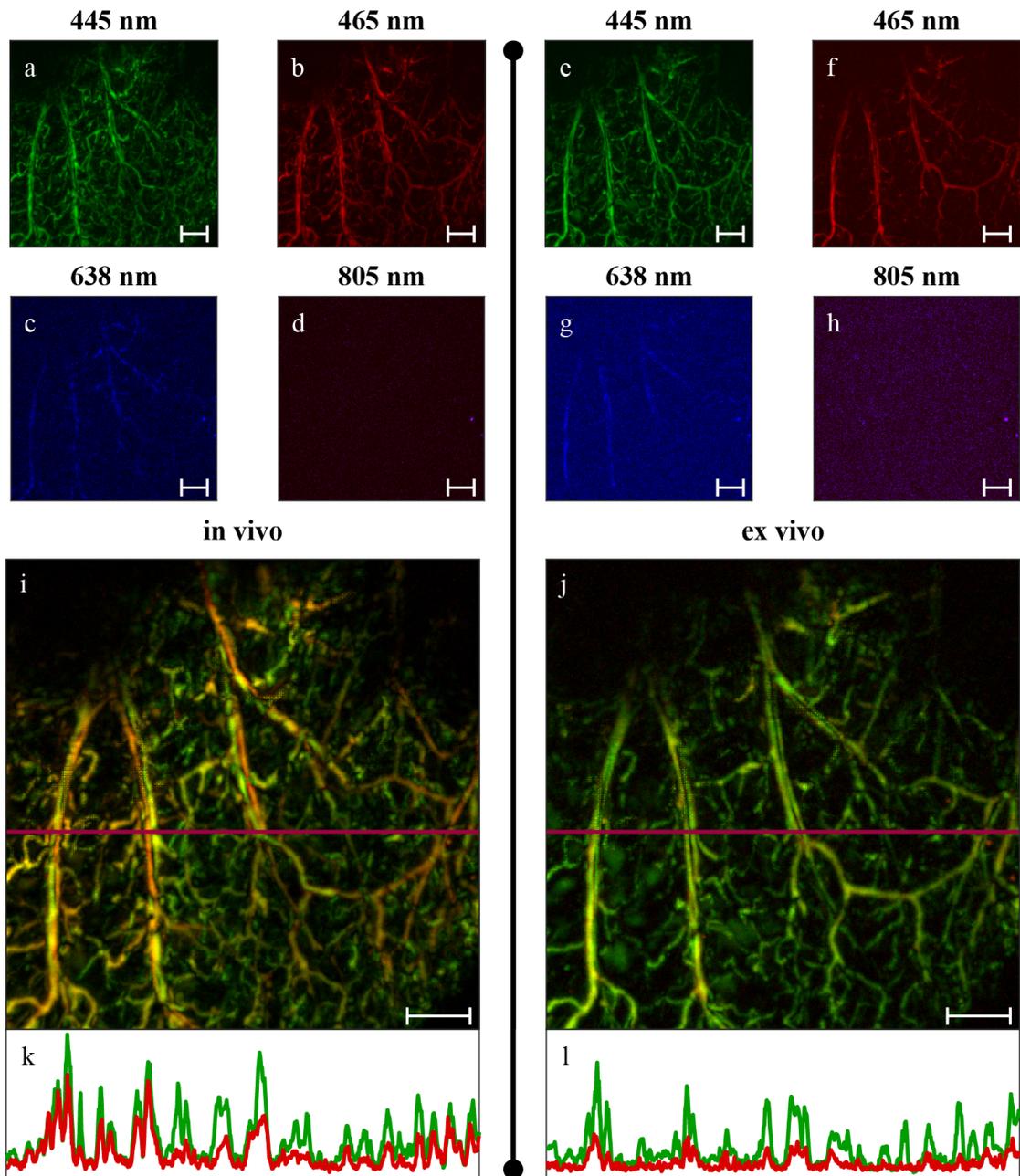
Figure 4.20: **Mesoscopic image in MS-PWFD of mouse in vivo and after euthanization.** a-d: reconstructed images of four wavelength of *in vivo* mouse ear. e-h: reconstructed images at four wavelength after euthanization. i: color coded overlay of the *in vivo* images. j: color coded overlay of the images after euthanization. 445 nm (green) and 465 nm (red), scale bar: 1 mm.

Image improvement through vesselness filter

Different techniques have been introduced to identify and characterize vessels of various sizes and position in the body. They all suffer from similar problems related to the optical properties of living tissue. In result, most vessel imaging modalities provide images with limited signal quality at shallow penetration depth.

A mathematical bases to describe blood vessels has been established [179]. In result, data can be filtered with respect to these features. The result is vessel-enhancement in images beyond the point provided by the image quality. A commonly expressed concern is, that the algorithm misinterprets structures as vessels which have a different origin. These could be of biological nature or measurement artefacts. In addition, filtering vessels may change to quantitative content, reducing the potential for functional imaging presented in section 4.6.

To assess the potential of vesselenss filtering for MS-PWFD, the *in vivo* data acquired in section 4.6 at 445 nm and 465 nm has been processed using different settings of the vesselness filter. The unprocessed data is shown in the top row of figure 4.21. A false-color overlay of the data is shown on the right. Below, the data processed at different settings of the vesselness filter is shown. A false color overlay for each color setting is also shown on the right.

The effect of the filter is clearly visible, by reducing the size of identified vessels and enhancing the contrast-to-noise ratio. Furthermore, the allocation of arteries and veins has not changed when changing the settings of the filter. This implies that the vesselness filter does not effect the reliability of MS-PWFD for characterization and oxygenation measurements of small blood vessels.
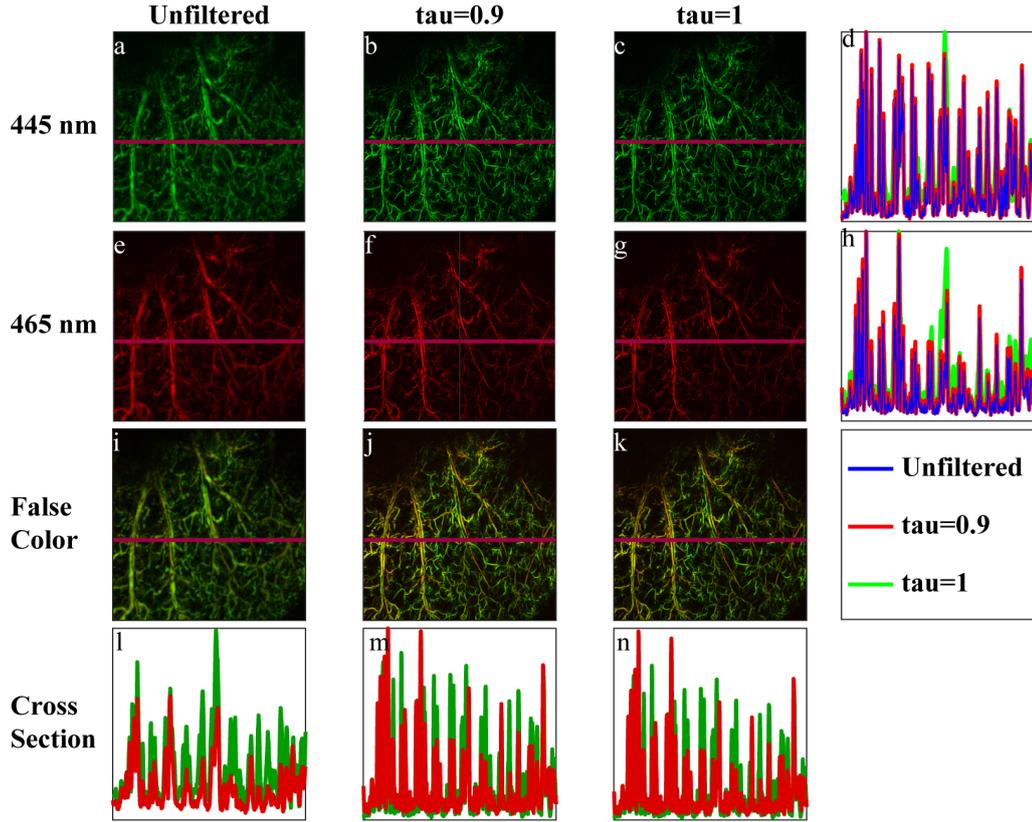
Figure 4.21: **Effects of different vesselness filter settings on mesoscopic image in MS-PWFD of mouse in vivo .** a-d: 445 nm and 465 nm data without filtering. Overlay on the right. e-h: Data as above after vesselness filter with $\tau = 0.9$ was applied. i-k: Data as above after vesselness filter with $\tau = 1$ was applied.

4.7 Visualization of circulating tumor cells (CTC)

All procedures with animals and humans were approved by the District Government of Upper Bavaria. Data acquired with assistance from Antonio Stylogiannis, Uwe Klemm and Pia Anzenhofer.

B16F10 is a cell line of melanoma cancer. Being a mutated epithelia cell, they express melanine. Melanine does not feature the same drastic decrease in absorption compared to hemoglobin at higher wavelength. Therefore significant contrast between the two chromophores exists in the red and NIR region. To study whether B16F10 cells can be visualized with *MS-PWFD Mesoscopy Setup 4*, a phantom featuring B16F10 cells embedded in agarose, similar to *phantom 4* described in section 3.9 has been prepared. B16F10 cells have been cultivated until a population of about 10^6 cells has been reached. A 30 mm Petri dish was filled with agarose up to 1 mm below the upper edge. A small aliquot of low melting agarose was mixed with phosphate-buffered saline with twice the nominal amount of agarose. Next, the concentration of B16F10 cells was adjusted to $1 \times 10^6 \, \mathrm{mL}^{-1}$,

corresponding to $1000\,\mathrm{mm}^{-1}$. Subsequently, $0.5\,\mathrm{mL}$ of each liquid were mixed together to generate a suspension of B16F10 cells in low melting agar at a density of $500\,\mathrm{mm}^{-1}$. This suspension was poured onto the bed of normal agarose already present in the Petri dish. The suspension was allowed to solidify and prepared for imaging by placing the 30 mm Petri dish inside a 70 mm Petri dish that was filled with distilled water for acoustic coupling. Finally, a *MS-PWFD* mesoscopic raster scan over the phantom using a field of view of 5 mm by 5 mm was conducted. The resulting data from each laser was reconstructed independently using the time domain back projection algorithm (fig. 4.22a-d).
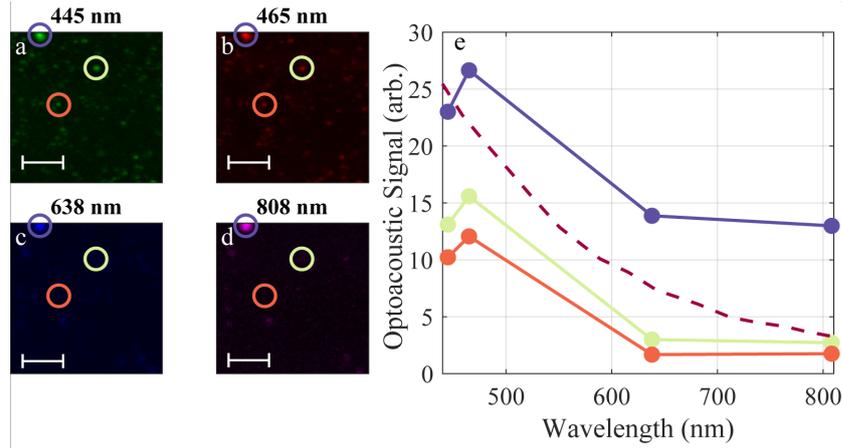
Figure 4.22: **B16F10 embedded in agarose for imaging with *MS-PWFD Mesoscopy Setup 4*** a-d: MIP along z axis at the four acquired wavelength. What appears to be the B16F10 can be seen as dots. Four potential cells were selected (colored circles). e: spectrum of the cells within the colored circle. The color of the circle matches the color of the line. Absorption spectrum of melanin added for reference as dashed line.

Four pixels with significant signal strength have been identified in the first image (marked by colored circles). Subsequently, the intensity at each wavelength of the given pixel is plotted (fig. 4.22e). The spectra of melanin taken from figure 1.9 is plotted as a dashed line for reference. The color of the circle corresponds to the color of the line in figure 4.22e. The acquired spectra of the peaks share a similar spectral profile to melanin, suggesting that the peaks actually are B16F10 cells.

After the visibility of B16F10 cells using the *MS-PWFD* system has been established, an *in vivo* experiment to investigate the visibility of B16F10 in vasculature was conducted. A CD-1 mouse was prepared for imaging as detailed in section 3.10. Initially, a 10 mm by 10 mm was performed and the data at 638 nm and 808 nm was reconstructed (fig. 4.23a-b). Subsequently, $2 \cdot 10^6$ B16F10 cells from the same population as used in figure 4.22 were administered to the mouse through the tail vain catheter. Next, the same *MS-PWFD* scan was performed again. The reconstructed data is shown in figure 4.23c-d. Distinct differences in the 638 nm channel can be seen, while no differences at 808 nm are apparent. This indicates
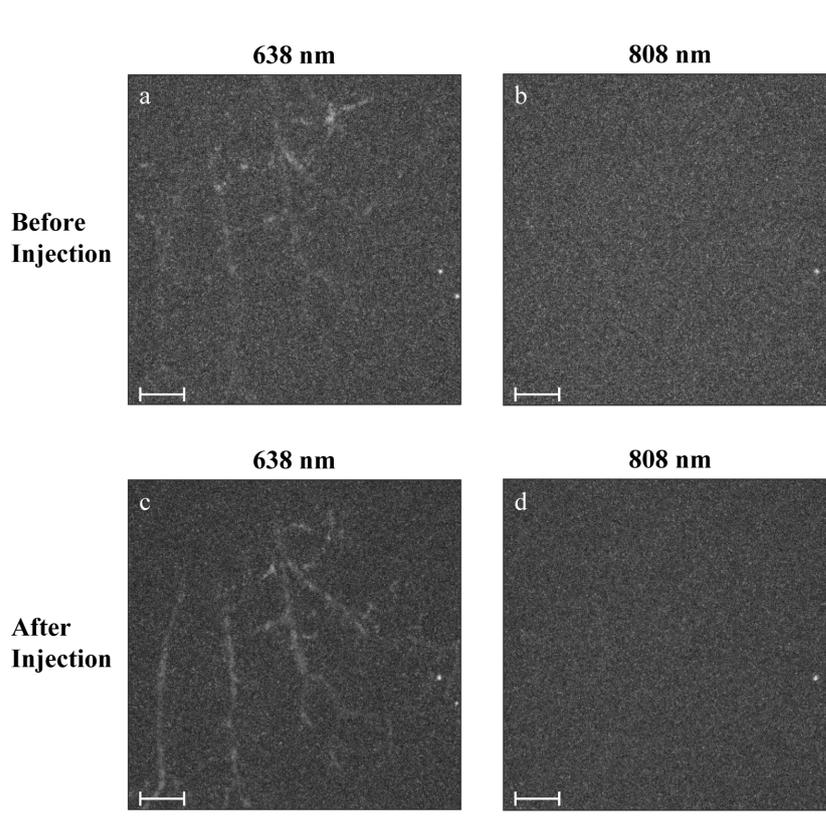
Figure 4.23: **MS-PWFD of mouse ear, before and after intravenous injection of 10^6 B16F10 cells.**a,b: maximum intensity projections of reconstructed data from a *MS-PWFD* of a mouse ear *in vivo*. c,d: same scan as above after 10^6 B16F10 cell were administered to the animal through a catheter inserted into the tail vein. Scalebar: 1 mm.

that circulating tumor cells can be visualized in the vasculature of the test subject using the 638 nm laser.

4.8 Evaluation of switchable proteins in MS-PWFD

Protein samples were provided by Andre Stiel.

Switchable proteins posses two states, one in which they present fluorescence and one in which they present a different spectrum or no fluorescence. The switching itself is triggered by illuminating the protein with light at a particular wavelength. As this allows to conduct reference measurements with the protein "switched off" and compare it to measurements with the protein "switched on" to eliminate background, switchable proteins have attracted much interest in the recent past [180]. The kinematics of switchable proteins is not yet fully understood. However, it takes a substantial light flux to quickly and reliably switch them from one state to the other. Commonly, high energy pulsed lasers are used for these applications. In this section, the possibility to switch proteins reliably using the *MS-PWFD Mesoscopy Setup 4* is investigated [181].
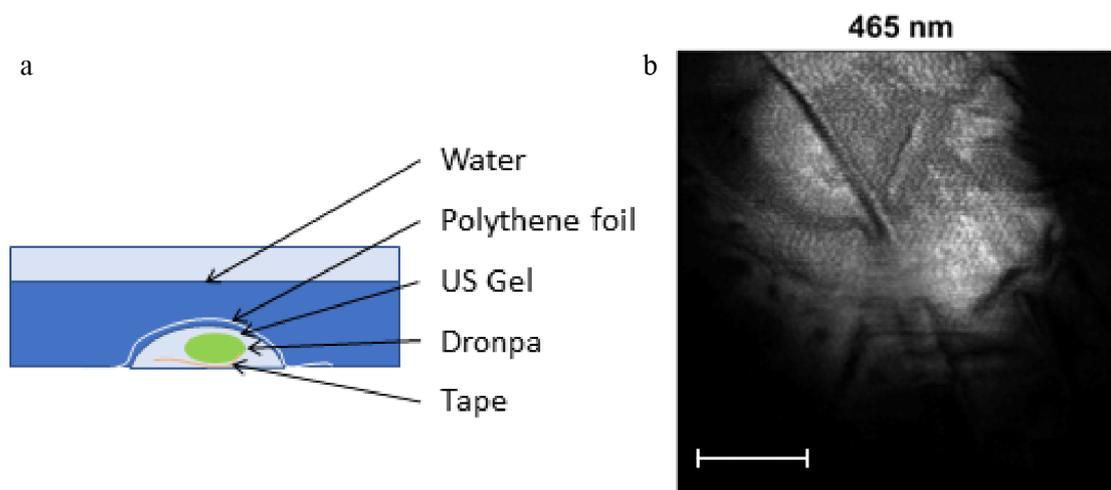
Figure 4.24: **Experimental setup of Dronpa-M159T measurement and MS-PWFD scan of Dronpa-M159T sample at** $465\,\text{nm}$**.** a: since Dronpa is highly water solvable, it was kept from the coupling water using a polythene foil. The sample diameter was about $2\,\text{mm}$. b: Reconstructed MIP of MS-PWFD scan using the $465\,\text{nm}$. The pixel featuring the highest signal was used for the subsequent measurements. Scalebar: $1\,\text{mm}$.

A small aliquot of Dronpa-M159T was mixed with acrylamide to provide a high absorbing sample. As Dronpa-M159T is highly water solvable, it could not be placed in a water bath as done during previous measurements. Instead, it was embedded in a stain of ultrasound-gel, and covered with one layer of polythene foil. The foil in turn was covered with distilled water to provide ultrasound coupling to the transducer (fig. 4.24a). Subsequently, a *MS-PWFD* raster scan of the sample was performed. Since Dronpa-M159T shares its absorption spectrum with GFP,

strong absorption at 465 nm was expected (fig. 4.24b). The point with the highest absorption was chosen for the subsequent measurement.

Using the 465 nm laser diode, 10^6 pulses at a repetition rate of 500 kHz were acquired. While this data was transferred from the acquisition units memory to the measurement PC, the laser was deactivated, which took about five seconds. This measurement was repeated six times. Of the acquired 10^6 pulses, 1000 pulses at a time were processed according to the *PWFD* algorithm. The optoacoustic signal content of the resulting pulse was calculated. This process was repeated for the next set of 1000 pulses of the measurement. The evolution of the pulse energy as a function of time is shown in figure 4.25.
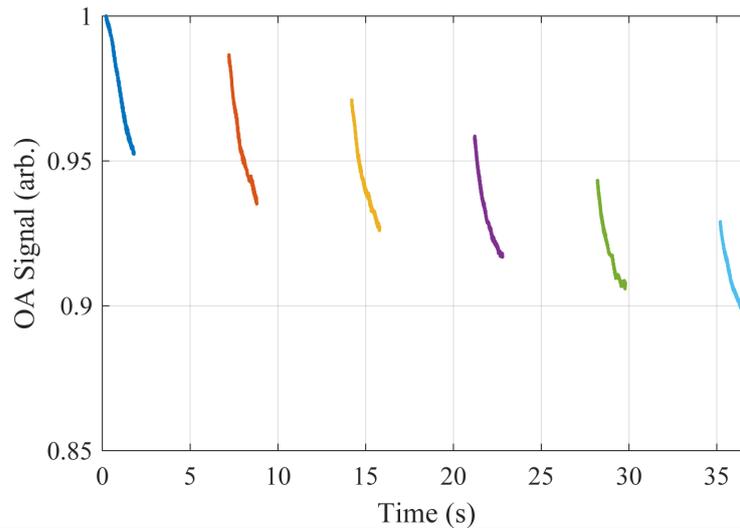
Figure 4.25: **Optoacoustic response of Dronpa-M159T in MS-PWFD at 465 nm.** The optoacoustic response of Dronpa-M159T as a function of time. Six subsequent measurements were performed. Each measurement consists of 10^6 pulses at a repetition rate of 500 kHz. Accordingly, one measurement took 2 s Between the individual measurements, the laser was inactive for 5 s

To determine the switching time of Dronpa-M159T using the *MS-PWFD Mesoscopy Setup 4* , a exponential decay function was fitted to each curve. In addition, the recovery ratio between the final data point of each measurement and the first data point of the subsequent measurement was determined. The results are presented in table 4.1.

The data suggests that *MS-PWFD Mesoscopy Setup 4* can be used to switch Dronpa-M159T from one state to the other using the 465 nm laser diode. However, the switching times are extremely long which may limit the usability of the method in biological contexts.

Table 4.1: Switching time of Dronpa-M159T.

Pulse	Recovery (%)	Time constant (s)
1	-	29.9
2	96.7	32.3
3	96.2	37.3
4	96.9	38.9
5	97.1	43.8
6	97.7	50.1

Chapter 5

Discussion and conclusion

By presenting the novel optoacoustic modality PWFD, a hybrid domain between frequency domain and time domain optoacoustics was introduced. Both modalities have their individual strengths and weaknesses. In chapter 4, PWFD was characterized with respect to existing modalities. To ensure that the obtained results were comparable, the same experimental setup for measurements in all modalities was used. Next, the imaging performance and possible applications of PWFD were analysed. Imaging phantoms with well understood characteristics were utilized. To demonstrate medical value and applicability, the skin of a number of volunteers was imaged with MS-PWFD and compared to existing time domain optoacoustic mesoscopy methods. To highlight biological value, studies on CD-1 mice have been conducted. MS-PWFD was used to visualize intrinsic properties of the specimen, such as blood vessel morphology and blood oxygenation. Furthermore, contrast agents and CTCs were added before imaging. Intrinsic and injected substances were measured at different wavelengths and the data was acquired simultaneously. Therefore, MS-PWFD was able to address biological and medical questions holistically.

5.1 Optoacoustic signal comparison of different modalities

Various measurements have been conducted that illustrate the difference in optoacoustic signal generation efficiency of different modalities. This section will give a discussion how the experimental measurements presented in chapter 4 compares to theoretical predictions made in chapter 2.

SNR and depth of field comparison between SWFD and PWFD

Figure 4.1i shows that for the case of $f_{rep} = 3.215\,\mathrm{MHz}$, the SNR calculated for *PWFD* and *SWFD* was the same. When the repetition rate was decreased while keeping the pulse duration constant, the peak power of the pulses was increased to keep the mean power at $100\,\mathrm{mW}$. This corresponds to a gradual evolution from

a *single wave* to a *pulse wave*. The increase in peak power overcompensated the decrease in number of energy transient. Hence, the overall SNR increased with the repetition rate, unlike in equation 2.91,were the pulse peak power was assumed to be constant. The SNR, achieved by *SWFD* processing the frequency component at 3.215 MHz, presented a stable SNR independent of the repetition rate. Since the pulse shape was constant for all repetition rates, no change in the heating function $H_t(t)$ was expected. This matched equation 2.90 suggesting the signal amplitude to be a function of the excitation frequency f_0, which is kept constant at all acoustic frequencies. Furthermore, when decreasing the repetition rate, the non-ambiguous field of view increased. This outlines that optimizing the pulse energy within the limits given by the instrument (fig. 3.3) or by maximum permissible exposure (MPE limits [174]) is key to achieving high SNR, while optimizing the repetition rate is secondary.

SNR comparison between PWTD and PWFD

An elaborated study to compare PWTD and PWFD has been completed. Before any measurements were made, and to exclude all experimental influences, a computer simulation of PWFD and PWTD for different SNRs was performed using exact Gaussian pulses (fig. 4.2). This would allow for a precise comparison between experimental and theoretical results. The expected SNR matched that calculated in equation 2.89 and 2.91. This is a strong indication that the case discussed in equation 2.91 and 2.89 can be replicated in theoretical models.

Subsequently, another measurement was performed using *SW-PWFD Mesoscopy Setup 3* as presented in figure 4.3. The raw data was processed in both modalities and the resulting waveform and SNR were compared. Similar as in the theoretical model presented in figure 4.2, an exact agreement between *PWFD* and *PWTD* was found. This further underlines the equality between the two discussed cases.

Comparison between SNR in PWFD, PWTD and SWFD in different measurement conditions

Measurement 4.4 illustrates the relationship between the achieved SNR in *PWFD*, *PWTD* and *SWFD* as a function of integration time, scattering coefficient, and illuminated area. A fundamental similarity of signals acquired through PWTD and PWFD was observed. However, the measurement failed to provide an exact agreement between the two modalities. This may be due to the interpolation necessary to match the expected and the actual sampling rate of the system with the repetition rate of the pulse wave. Unexpectedly, the sampling rate featured a 1 kHz offset to the expected value of 62.5 MS/s. In order to evaluate the measurement using *PWFD* and *PWTD* techniques, a linear interpolation from the measured to the expected sampling rate was performed. The re-sampling by interpolation was done with no knowledge of the periodicity of the signal. Due to noise in the measurement, periodic features may have not been reconstructed during each iteration of the pulse. This disturbance to the periodicity of the signal

may yield in unexpected behaviour of the processing algorithms, which explains the difference between the *PWFD* and *PWTD* signal.

The SNR generated by *SWFD* was lower than generated by *PWTD/PWFD*. As elaborated in section 2.11, under equal circumstances, *SWFD* is expected to generate a SNR that is a factor of $2\pi \cdot \sqrt{e}$ higher than that of *PWFD*. However, this is only true if the condition $\tau_L = 1/f_0$ is fulfilled and Gaussian pulses are used. In the presented example, $f_{rep} = 2\,\text{MHz}$ and $\tau_L = 25\,\text{ns}$ and due to technical limitations of the used function generator, square pulses instead of Gaussian pulses were used. To keep the mean power of both signals constant at $\bar{P} = 100\,\text{mW}$, the peak power of the pulse wave was increased to:

$$H_0^W = \frac{\bar{P}}{(f_{rep} \cdot \tau_L)} = \frac{100\,\text{mW}}{25\,\text{ns} \cdot 2\,\text{MHz}} = 2\,\text{W}$$

in result, the peak power of each energy transient was increased by a factor of 20. According to equation 2.79 this will result in an increase in optoacoustic pressure by the same factor. In return, the number of energy transients in *PWFD* per given time interval were a factor of 12 lower than assumed in section 2.11. By referring to equation 2.91, this would yield a decrease in SNR by a factor of $\sqrt{12} = 3.46$ compared to the case described in section 2.11. Taking both effects into account, the SNR of *PWFD* compared to *SWFD* was expected to increase $20/3.46 = 5.77$ fold. Furthermore, the pulse duration was 25 ns (FWHM), yet the presented calculation assumes $\tau_L = 1/f_0 = 40\,\text{ns}$ corresponding to $FWHM = 40\,\text{ns} \cdot 2\sqrt{2\ln(2)} = 94.2\,\text{ns}$. This accounts for another 4-fold increase of the SNR of *PWFD* compared to *SWFD*. Finally, the pulses used for *PWFD* were not Gaussian as assumed in section 2.11. Instead, they featured a steeper rise, causing a further increase in SNR of *PWFD* as indicated by equation 2.14.

Effect of pulse duration on SNR in PWTD

The strength of the generated optoacoustic signal is a function of the rate of change of the illumination waveform (section 1.4). To generate maximum SNR at a given energy deposition, the most efficient waveform would be a rapid succession of rising and falling energy transients. This would however not allow for any spatial resolution through the depth of field, which dictates the maximum repetition rate to be $f_{rep} < v_s/DoF_z$. A remedy between the two contradicting requirements of signal generation efficiency and depth of field is to concentrate the maximum possible energy in a single pulse, whose repetition rate is defined by the desired depth of field. These considerations are based on the assumption that the entire generated signal can be detected. In practice, the experimental setup would feature a limited bandwidth. Hence, some of the signal generated by very short pulses may lie in frequency ranges undetectable by the setup. This may cause a stronger decrease in signal strength compared to the gain by the higher signal generation efficiency due to the sharper energy gradient. In figure 4.5 the achievable SNR using *Signal Evaluation Setup 2* is shown as a function of the pulse duration. The pulse duration varied between 300 ns and 5.2 µs. The optimum pulse duration correlated with

the systems bandwidth. This was demonstrated for different system bandwidths (fig. 4.5f). This behaviour can be explained by revisiting section 2.2. When the pulse duration was decreased, the bandwidth of the generated optoacoustic signal increased, together with the signal generation efficiency. However, due to the limited bandwidth of the system, a portion of the generated energy was located at acoustic frequencies not accessible by the measurement setup. In consequence, the detectable signal did not necessarily increase when the pulse duration was shortened. However, the presented measurement indicated an optimum, when the two counter-acting effects yielded the maximum possible SNR.

The pulse used for this measurement was not Gaussian, but featured a very steep rising and falling edge independent of the pulse duration. According to equation 2.10, an optoacoustic signal is only generated at the edges of the pulse. At the rising edge, a pulse with positive polarity is created, at the falling edge the pulse polarity is negative. Due to the bandpass-like filtering characteristic of the setup, both signals featured side-lobes, which interfered constructively to boost the signal strength. This defined the condition for pulse duration enabling maximum SNR. Depending on the bandwidth of the system, the distance between the side-lobes and the main lobe varied. Even though Gaussian pulses do not feature clearly separated rising and falling edges, like the rectangular pulses, the optoacoustic signal generation takes place at the edges, which experiences the same bandpass filtering due to the limited bandwidth. Therefore, it is likely that a similar effect would be observed with Gaussian pulses. However, using the hardware presented in this thesis, such a measurement was not possible reliably.

Possibilities to increase pulse energy

The greatest potential for improvement was identified by increasing the pulse energy of the laser diodes. This may be the most challenging aspect as an increase in pulse duration will rapidly cause catastrophic optical damage to the laser diodes [177]. Increasing the pulse current would be difficult because the currents rate of change is in the order of 20–30 A/ns. This means that small stray inductance, as such of the laser diodes packages which are commonly in the order of 5 nH, will cause an induced voltage of 100–150 V and drastically reduces voltage drops across the diode driving the pulse current [182]. Hence, the majority of the electrical pulse energy is dissipated, an effect that increases with a greater current of the pulse. Nevertheless, selecting a driving circuit with a higher compliance voltage may result in higher optical pulse energy. The utilized driver had a compliance voltage of 500 V, but was only operated at 300 V for safety considerations. A well designed circuit with adequate safety features may allow the circuit to operate closer to its compliance voltage. Furthermore, some vendors provide switches based on the avalanche effect that allow compliance voltages in excess of 1000 V [183]. While these do not feature the fast switching provided by the utilized circuit, exploring these possibilities may allow for stronger light pulses to be generated.

Non-periodic pulse wave excitation schemes

Using pulse wave excitation the repetition rate is limited by the time the ultrasound takes to travel from its origin to the detector. An additional time buffer for any echoes to fade must also be considered. For the presented system, this limits the practical repetition rate to about 200 kHz. However, at 200 nJ pulse energy the mean power of the laser diodes is only 40 mW while the compliance power rating of the 445 nm diode is 3.5 W. This would allow the repetition rate to be increased up to 17.5 MHz. However, the resulting depth of field would only be 85 μm.

To overcome the time-of-flight limitation, non periodic excitation pulse waves have been suggested [184, 185]. While originally implemented for ultrasound application, the concept can easily be transferred to optoacoustics [186]. The principal is the same as for pulse compression, which states that the excitation waveform itself does not necessarily have to be a single pulse to allow for high resolution imaging, as long as its auto-correlation is. Since the excitation waveform is still a pulse wave, it will feature high optoacoustic signal generation efficiency, but allow for higher repetition rates than would be possible with a constant repetition rate [187]. Since strictly orthogonal excitation patterns exist, simultaneous multispectral imaging could be demonstrated [188].

MS-PWFD Mesoscopy Setup 4 could readily be operated with Golay code excitation, which would allow for much faster image acquisition. However, the processing required to recover the optoacoustic signal from the acquired data is far more computationally expensive than the MS-PWFD algorithm used in this thesis. If the processing would be done on the fly to avoid large amounts of raw data to be saved, the acquisition time may increase significantly.

5.2 Evaluation of SW-PWFD mesoscopy

SW-PWFD Mesoscopy Setup 3 is a *PWFD* mesoscopy system featuring a focused 50 MHz transducer and laser diode based pulse wave illumination. According to equation 1.19, the resolution to be expected at 50 MHz and $NA = 1$ is:

$$R_x = 1.02 \cdot \frac{3\,\text{mm} \cdot 1450\,\text{m/s}}{50\,\text{MHz} \cdot 3\,\text{mm}} = 29.6\,\text{μm} \tag{5.1}$$

The studies presented in section 4.8 and 4.3 showed an achievable resolution of 34 μm or more. However, the resolution of the actual system usually fell short of the expected value. The reasons for this can be manifold. First, the optical pulse used for excitation is of finite duration. Therefore, lower frequencies were more emphasized than high frequencies, yielding a lower effective resolution. Next, the accuracy of the stages was limited. They feature a position encoder operating at 5 kHz. When moving at 10 mm s^{-1}, the position resolution was limited to ± 2 μm. Furthermore, the system was acquiring data while the stages are moving. When 100 pulses at 200 kHz were acquired, the acquisition took 0.5 μs in which the stages moved 5 μm. Together with the limited encoder resolution, this accounts for ± 7 μm position uncertainty, which is 25% of the expected resolution. Thus, the achievable resolution and the required step-size could not simply be determined by equation

1.19. Moreover, the reconstruction algorithm presented in section 2.3 assumed the sample to be homogeneously illuminated. Hence, any deviation from the assumption $H_r(r) = const.$ would drastically affect the quality of reconstruction. Providing homogeneous illumination was difficult because laser diodes only provide low brightness. This was addressed by designing the fiber illumination system presented in image 3.4. While this setup was expected to provide homogeneous illumination in the focus of the transducer, inhomogeneous illumination could not be avoided outside the focal plane.

Determining the ideal step size for *PWFD* mesoscopy

If the step size was too big, the system's resolution would be deteriorated and spatial aliasing effects may appear. If the step size was to small, the acquisition time increased unacceptably. To determine the optimum step size, a raster scan of *phantom 3* was performed. The step size was chosen to be 10 µm which was the lowest feasible value with the utilized stages. To determine how the resolution would deteriorate with increasing step size, every n*th* acquired data point was removed from the raw data before reconstruction, to simulate a raster scan taken at an n*th* times higher step size. The resulting data was reconstructed and a Gaussian function was fitted to a prominent feature of the resulting image (fig. 4.8). The dependency of the width of the fitted Gaussian (in three directions, R_x, R_y and R_z) clearly showed that the system's resolution was highly dependent on the step size. Even a small increase in the step size resulted in a drastic decrease in resolution. In consequence, all following *in vivo* measurements were conducted at a step size of 10 µm, accepting the resulting higher acquisition time. When there was need for quick acquisition, the size of the field of view was reduced to achieve acceptable measurement times (section 4.5).

Fluence correction in the image domain

To investigate the homogeneity of the illumination along the acoustic axis, a *PWFD* raster scan of *phantom 3* was performed because it was spatially large and features homogeneous absorption. The optoacoustic signal was expected to be of equal strength across the entire phantom (fig. 4.6). Additionally, the strength was dependent on the position of the absorber along the acoustic axis of the system. Even a small position offset of 100 µm resulted in a detectable change in optoacoustic signal strength. This effect could be accounted for using a fluence correction algorithm on the reconstructed image. Therefore, the dependency between position and illumination was determined (fig. 4.6c). This was used to correct the brightness of the reconstructed image as a function of the z position. While this method was viable to reduce the effect of fluence inhomogeneity, it could not reverse the diminished SNR in the reconstruction (fig. 4.6d). This was achieved by developing a fluence correction algorithm that acted on the raw data before reconstruction. A more sophisticated model would also benefit from precise knowledge of the light field. This could be accomplished using a beam profiler or similar methods.

Frequency color coding to enhance image quality

The low frequency regime of optoacoustic data contains more signal energy, yet the high frequency part features higher resolution (eq. 1.19). To combine the high signal strength with high resolution, different frequency bands could be color coded into the same image (fig. 4.6). To find the cut-off point in the power spectrum that contains 50% of the optoacoustic signal, a commutative plot of the spectrum of the optoacoustic signal was calculated and the 50% point identified, which lies at 35.5 MHz. This indicates that the lower third of frequencies contains half of the optoacoustic signal. The lower frequency band was color coded in blue, the higher in green. The fused image is shown in the bottom right of figure 4.7, which combines both resolution and signal strength and will be used to present optoacoustic data acquired from *in vivo* measurements.

When presenting multispectral data, color coding of the frequency bands was not feasible because the color channels were occupied by the multispectral information. In this case, adding the frequency bands together into a single image with different weighting factors for each frequency band was a viable alternative. In result, the high resolution features were still well visible in the presence of low frequency signals.

Optimizing integration time for *in vivo* applications

Besides the step size, the integration time (i.e. number of averaged pulses or deposited laser energy) has a fundamental influence on the image quality and on the acquisition time. The processed SNR depends substantially on the initial SNR (fig. 4.2). Therefore, it was important to establish this parameter using a realistic optoacoustic signal source. The data acquired by *PWFD* raster scanning of the skin of a volunteer was recorded without processing, to be evaluated offline simulating different integration times. Hence, the effect of the acquisition time on the image quality could be evaluated while keeping all other experimental parameters constant. To identify the optimum acquisition time, the size of a submerged blood vessel was determined and the contrast to noise ratio (CNR) was calculated (fig. 4.10). The achievable resolution did not fundamentally depend on the integration time. Nevertheless, limiting the bandwidth to higher frequencies showed a substantial improvement of the resolution which confirmed the measurements presented in figure 4.7. However, the CNR showed a square root dependency on the integration time (eq. 2.91). Therefore, the integration time should be chosen as long as possible under the given measurement conditions.

5.3 Evaluation of MS-PWFD mesoscopy

Signal separation in MS-PWFD

MS-PWFD mesoscopy was added as a natural augmentation to the *SW-PWFD* mesoscopy. Since a large number of averages $N_{avg} = 10^2 - 10^3$ were needed to achieve sufficient SNR, the integration time was larger than necessary to capture

a single pulse. In consequence, a large number of data points in the frequency domain carried no information. Using multiple lasers at different repetition rates allowed to populate some of these frequency bins with additional information, corresponding to the optoacoustic signal acquired at different optical wavelengths. Therefore, MS-PWFD presented a modality in which multispectral data could be acquired without affecting acquisition time or motion artefacts because the recording of all wavelengths occurred simultaneously. The concept is explained by an example measurement presented in figure 4.11. The signal from all four lasers overlapped in the raw data in the frequency domain. However, knowing which laser featured which repetition rate, the frequency components could be assigned to the according laser. The image also outlines the difficulties encountered in MS-PWFD, since the FFT algorithm expects a periodic input signal. A pulse wave is only periodic when the repetition period (the inverse of the repetition rate) is an integer multiple of the acquisition time. The acquisition time was chosen to be a multiple of the repetition period of the first laser. In consequence, only the frequency components of the first laser corresponds to the FFT of the raw data. The components of the other lasers deviated from the raw data because the repetition period is not an integer multiple of the acquisition time. Therefore, non-periodic artefacts are present at these frequencies, which spread the energy over multiple frequency bins instead of concentrating it into one single peak. Consequentially, the computationally more expensive demodulation algorithm introduced in section 2.10 was deployed. It mimicked the behaviour of a IQ demodulator on all desired frequencies simultaneously. By formulating the operation as a matrix multiplication, it was possible to implement the process in the GPU unit of the PC, which allowed the data to be processed in real-time. This reduced the amount of computer memory needed, as the raw data did not need to be stored in the computer's RAM. In conclusion, large fields of view could be acquired.

Resolution in MS-PWFD mesoscopy

After the image quality of SW-PWFD mesoscopy was established, it was of interest whether introducing MS-PWFD would diminish it. Therefore, *phantom 4* was scanned again using the same parameters as in the SW-PWFD (fig. 4.12). By comparing the resolution along R_x, R_y, R_z, no evidence for deterioration in signal quality when switching from SW-PWFD to MS-PWFD was found. The best comparison to SW-PWFD was presented by the first laser because it is the same laser operating at the same repetition rate as used for the measurements (fig. 4.8). However, due to the low SNR achieved at 638 nm and 808 nm, the pulse duration of the laser was increased by adding additional capacitors to the circuit (fig. 3.3a). This resulted in a slightly worse resolution dropping from 34 µm to 41 µm (fig. 4.12).

In summary MS-PWFD is the first instrument capable of providing multispectral information at mesoscopic resolutions without time sharing, making it the ideal application for medical and biological measurements.

5.4 Medical applications of MS-PWFD

The laser wavelengths utilized in MS-PWFD were split in two regimes, **short wavelengths** (445 nm and 465 nm) and **long wavelengths** (638 nm and 808 nm). In section 4.3, the usability of MS-PWFD for skin imaging has been demonstrated. The **long wavelengths** did not provide sufficient SNR to contribute information to the image (fig. 4.13). Therefore, they were not considered for applications that only provide intrinsic contrast (without using contrast agents). Both lasers in the **short wavelengths** showed a clear contrast between the individual skin layers. They allowed vessels to a depth of more than 600 µm to be identified, which was comparable to values reported for SW-SPTD-mesoscopy systems [189]. These systems reported penetration depths up to 800 µm. However, they operate at 532 nm, which featured less scattering and absorption compared to the **short wavelengths** used in MS-PWFD. Similar to previous work, the morphological structures of skin, such as the epidermal-dermal junction could be clearly identified.

Multispectral mesoscopic measurements of human skin potentially allows analysis of blood oxygenation of small vessels, total blood volume and label-free biomarkers [148]. As MS-PWFD offers comparable penetration depth and resolution as SPTD systems, these advantages could also apply. However, the **long wavelengths** did not provide any usable information from human skin. It might be desirable to either replace the laser diodes with more powerful versions, providing a higher pulse energy, or with laser diodes at different wavelengths, at which intrinsic contrast would be present.

5.5 Biological applications of MS-PWFD

The **short wavelengths** featured extraordinary strong absorption by biological chromophores (fig. 1.9). The **longer wavelength** could be used to detect contrast agents because their absorption spectrum did not fundamentally overlap with that of hemoglobin (see figure 1.10). At first, the results relating to functional imaging of contrast agents will be discussed. Subsequently, the discussion will be extended to imaging biological chromophores.

Imaging contrast agents using MS-PWFD

A reproducible measurement environment was required, to investigate the visibility of important contrast agents using *MS-PWFD Mesoscopy Setup 4*. As the systems resolution was determined to be in the range of 30–40 µm, the simulating phantom should be of comparable size. The signal that has traveled through the TOPAS and the signal that has not were compared (fig. 4.16). The signal through TOPAS was attenuated by about 45% compared to the signal that did not travel through TOPAS. Furthermore, the signal traveling through TOPAS arrived at the transducer $\delta_t = 65$ ns earlier. Assuming a speed of sound in water of $v_s = 1540$ m/s

yields a speed of sound of:

$$v_{TOPAS} = \frac{d_{TOPAS}}{\frac{d_{TOPAS}}{v_s} - \delta_t} = \frac{140\,\mu m}{\frac{140\,\mu m}{1540\,m/s} - 65\,ns} = 4973\,m/s \qquad (5.2)$$

This striking mismatch in speed of sound made reconstructing data acquired through TOPAS difficult. Nevertheless, measuring the optoacoustic signal generated by contrast agents in controlled environments was able to provide a solid understanding of the behaviour of these contrast agents in the presented system. Three contrast agents were injected into the microfluidic chip and measured using *MS-PWFD Mesoscopy Setup 4* (fig. 4.17). The reconstructed channel size was much larger than 100 μm. This may be due to the significant speed of sound mismatch of TOPAS to water (fig. 4.16a). The mutli-spectral composition of each signal is presented in figure 4.18. For Alexa Fluor 780, an excellent agreement between the optoacoustic signal and the literature values could be reported. For DiD and Indocyanine green (ICG), no data for the full spectrum acquired in MS-PWFD was available. However, for the two data points at 638 nm and 808 nm it was shown that the measured value of ICG deviated from the expected value. A possible explanation for this is that the measurement was performed using an ICG concentration of $c = 6.5\,mM$, while the reference data used assumed a concentration of $c = 1.25\,mM$. At these high concentrations, no major dependency of the extinction spectrum on the concentration was assumed. However, the excellent agreement in the data of Alexa Fluor 780 and the unsatisfactory agreement for ICG suggests that the assumed spectrum of ICG did not match the actual spectrum. The spectrum of ICG is dependent on numerous variables. To perform an accurate comparison, the spectrum of the sample under question would need to be determined using other methods just before or after the optoacoustic measurement. As the shape of the spectrum is a function of the concentration, as well as of the properties of the solvent, the possibility to derive functional information from the spectral properties of ICG could be considered. Accurately measuring the spectrum would allow to draw further conclusions of the biological environment in which ICG is present.

In vivo imaging of contrast agents using MS-PWFD

The study clearly demonstrated that Alexa Fluor 780 and ICG provide a substantial signal at 808 nm and DiD at 638 nm. Therefore, it appeared promising to conduct studies in a model organism using contrast agents. ICG primarily binds to blood proteins [190]. Thus, it will remain in the blood stream until it is processed by the liver to the bile within 120–180 s [191]. This sparked great interest for numerous medical applications where vessel dynamics were visualized including angiography, dermatology, gastroenterology and cardiology [192–195]. Optoacoustic visualization of ICG in order to monitor perfusion has been demonstrated with optoacoustic tomography [196–198]. The ability to visualize ICG at mesoscopic resolution and simultaneously provided further metabolic information at **short wavelengths** was demonstrated (fig. 4.19).

The *in vivo* procedure is described in section 3.10. To ensure meaningful images could be obtained despite the short half life of ICG, the field of view was limited to 4 mm by 4 mm to keep the acquisition time short. Furthermore, the ICG was injected only after the scan was started. The ICG sample used for injection has the same concentration as that investigated in section 4.4 of 5 mg/mL corresponding to 6.5 mM. The LD_{50} of ICG for mouse is 60 mg/kg [199]. Two dosages of ICG were used for this investigation, 75 μg and 250 μg. Assuming the body mass of the used test animal to be 20 g, the first dosage corresponds to 6.25% of the LD_{50} and the second to 20% of the LD_{50} value. This was done to simulate a dosage which would be used for clinical applications, in which no side effects were expected, while the second dosage was chosen so high that it is likely to be of no therapeutic value, yet not toxic to the test animal. Studies have shown that dosages of up to 2 mg/kg are well tolerated by patients. This corresponds to 3.3% of LD_{50} which is half of the first dose used in this measurement [200]. The maximum daily dose of ICG in clinical applications should not exceed 5 mg/kg, which corresponds to 8.3% of the LD_{50} and lies in between the two doses used here. [201].

A strong signal from hemoglobin was apparent at the **short wavelengths** during all measurements (fig. 4.19). No significant signal at 638 nm could be acquired for any measurements. However, at 808 nm, the effect of ICG was clearly visible. While no significant signal was present without injection, major vessels become visible at the first dosage. This effect increased for the second dosage, where even smaller vessels became apparent. Depending on the exact biological or medical application, a trade-off between visibility of small vessels and dosage has to be found.

Blood oxygenation measurements using MS-PWFD

Nearly all metabolic processes require oxygen which is transported via hemoglobin through the body [202]. The concentration of oxygen in blood vessels can be determined by the spectral properties of hemoglobin [203–206]. Multispectral optoacoustics provided three dimensional oxygenation maps at high resolution due to the wavelength-dependent absorption of oxygenated (HbO_2) and deoxygenated (Hb) hemoglobin (fig. 1.9) [141, 148, 207]. By acquiring the optoacoustic signal at different excitation wavelengths and deploying multispectral unmixing techniques (sec. 2.4), precise spatial and temporal measurements of oxygenation could be made. Using *MS-PWFD Mesoscopy Setup 4*, high absorption by hemoglobin was expected at the **short wavelengths**. To achieve a reliable oxygenation value, the absorption of Hb and HbO_2 must be different between the utilized wavelengths. In addition, the absorption must be high to generate a sufficient optoacoustic signal. Therefore, the **short wavelengths** were a logical choice for oxygenation measurements (tab. 5.1). The absorption of both Hb and HbO_2 was almost ten times higher than that at the **long wavelengths**. Furthermore, at 445 nm, the Hb absorption was more than three times higher than that of HbO_2. At 465 nm, the HbO_2 absorption is 2.8 times higher than the Hb absorption.

The ear of a CD-1 mouse has been measured using MS-PWFD (fig. 4.6). Since the contrast of Hb and HbO_2 is very high between the two **short wavelengths**,

λ (nm)	$\epsilon(\text{HbO}_2)$ $(cm^{-1}M^{-1})$	$\epsilon(\text{Hb})(cm^{-1}M^{-1})$	$\epsilon(\text{HbO}_2)$ / $\epsilon(\text{Hb})$
445 nm	78884 (100%)	259974 (100%)	0.3
465 nm	38440 (48%)	18702 (7%)	2.1
638 nm	460 (0.6%)	4474 (1.7%)	0.1
808 nm	856 (1%)	724 (0.3%)	1.2

Table 5.1: Molar extinction coefficient of Hemoglobin in water at wavelength used in MS-PWFD [52–54]. Percentages give relative values to the absorption at 445 nm.

no unmixing was performed. Instead, the two channels were color coded with green being 445 nm, which mainly corresponds to Hb and red being 465 nm mainly corresponding to HbO$_2$. Vessels that appeared mainly red were considered to be oxygen-deprived and regarded as arterial blood vessels. Additionally, vessels that were mainly green were considered oxygen-rich, and therefore veins. This method could be evaluated by using known mouse anatomy. Commonly, arteries and veins run in parallel. Therefore, if parallel vessels can be identified, most likely one is an artery and one is a vein. Focusing on the large vessel at the center of the image, a difference in color indicated that the differential absorption allowed blood oxygenation to be determined. Upon the death of the test animal, it seized to respire. As its tissue was still consuming oxygen, the oxygenation level in all blood vessels dropped until it reached (close to) zero. In the *ex vivo* image, the absorption at 445 nm was expected to dominate and the image was mostly green (fig. 4.20). The total absorption at 465 nm was much lower than at 445 nm. Hence, oxygen-rich, small vessels would be more easily concealed by noise than oxygen-deprived vessels. This caused the oxygen content of small vessels to be underestimated. More advanced algorithms will be required to precisely account for this effect.

The differential absorption of wavelengths in blood vessels in human skin have been measured (fig. 4.13 and 4.15). Yet, assigning oxygenation values to identify vessels is difficult due to the complexity of human skin. Deploying a fluence correction model for each wavelength independently may help to resolve these features, even in morphological complex structures such as human skin.

Visualization of circulating tumor cells (CTC)

Metastasis is a fundamental step in the development of carcinogenic diseases. The cells of the initial tumor begin to migrate through the surrounding tissue until they reach the body's vascular system. These circulating tumor cells (CTCs) have the ability to develop into lesions in previously unaffected regions of the body causing the majority of cancer-related deaths [208]. Current imaging methods focus on detecting tumours (sec. 1.1). However, they are unable to fully acquire the distribution mechanism mainly because a very low number of CTCs is responsible for metastasis . To enable early detection, the system must be able to detect CTCs at very low concentrations, as little as 500 cells per milliliter of blood [208–211].

The real-time, multispectral capability at mesoscopic resolution *MS-PWFD* offers the opportunity to not only study the propagation of CTCs, but also put it in

an anatomical context. The metabolic and morphological information was mainly provided by the **short wavelengths** at 445 nm and 465 nm, as these wavelengths allowed to image the blood vessel distribution, as well as the oxygenation (sec. 4.6). The absorption of HbO_2 and Hb dropped substantially at wavelengths longer than 600 nm (fig. 1.9). Therefore, excitation lasers operating at these wavelengths were able to visualize contrast agents. In the past, optoacoustic microscopy at NIR wavelengths have been used to detect CTCs *in vivo* [143, 212], but optoacoustic microscopy is limited to superficial blood vessels (sec. 1.9). Hence, detecting CTCs in the very low concentrations required for clinical applications may be difficult. As *MS-PWFD* does not depend on optical focusing, it can potentially target deeper and larger vessels than microscopic methods drastically reducing the acquisition times needed to measure a given blood volume for the presence of CTCs.

To determine the sensitivity of *MS-PWFD* for identifying CTCs, a sample of B16F10 cells suspended in agarose has been prepared and scanned using *MS-PWFD Mesoscopy Setup 4* . The concentration of cells was $500\,mm^{-3}$ (fig. 4.22). The number of detected absorbers was far lower than that measured using *phantom 4* (fig. 4.12) despite using nearly the same concentration in both cases. However, the good agreement between the spectral properties of the acquired data with that of melanin, which is expressed by B16F10 cells, indicated that the detected signal originated from B16F10 cells. CTCs are often present in the form of microclusters [143, 208, 210]. Therefore, the imaged structures in figure 4.22 were possibly not individual cells, but most likely microclusters. Hence, the sensitivity of the MS-PWFD setup was sufficient to identify clusters of B16F10 cells, but not individual cells.

The detectability of B16F10 cells as CTCs was explored by scanning a mouse ear before and after administering $2 \cdot 10^6$ B16F10 cells intravenously. Assuming a total blood volume of 2 mL, this corresponds to a cell concentration of $1000\,mm^{-3}$. While the signal at the **short wavelengths** was expected to be concealed by the strong absorption of hemoglobin, a difference at the **long wavelengths** was expected (fig. 4.23). While no signal change before and after injection was apparent 808 nm, an increase in signal amplitude can be seen at 638 nm along the blood vessels of the mouse ear. This can be explained by the drop in absorption of melanin between 638 nm and 808 nm.

In conclusion, the sensitivity of the presented setup is insufficient to monitor individual circulating CTCs. However, it is possible to qualify the distribution of CTCs over the very large field accessible by *MS-PWFD* and at penetration depths not possible by optoacoustic microscopy. Therefore, statistical methods may be used to determine the distribution of CTCs in anatomical regions not accessible by optoacoustic microscopy.

5.6   Conclusion

This thesis introduced the novel modality of PWFD, which uses a pulse wave to generate the optoacoustic signal which is then detected in the frequency domain. This opened up the possibility of frequency multiplexing between multiple laser

light sources. In result, simultaneous multispectral imaging was enabled. In this implementation the number of acquired wavelengths had no effect on the acquisition time and motion artefacts between wavelength acquisition. This was enabled by continuous wave laser diodes operated by pulsed current drivers to generate short yet intensive light pulses. They can be used to perform multispectral optoacoustic mesoscopy in the frequency domain. Through a comprehensive SNR analysis, this method was shown to be equivalent to PWTD optoacoustics, which represents the current state of the art of optoacoustic imaging. Additionally, it is far more efficient than SWFD optoacoustics, which was mainly deployed for optoacoustic imaging utilizing laser diodes.

Unlike time domain methods, PWFD allows to acquire multiple lasers operating at different frequencies through frequency multiplexing without time sharing. Therefore, true simultaneous multispectral optoacoustics was demonstrated, for the first time. Currently, multispectral mesoscopy utilizes optical parametric oscillators with an extremely low repetition rate or multiple solid state lasers causing an increase in acquisition time proportional to the numbers of lasers used. For *in vivo* applications, this may result in unacceptable long acquisition times, since the process of interest features faster time scales than the acquisition time, or introduce motion artefacts that diminish the resolution. In MS-PWFD, the acquisition time is unaffected by the number of acquired wavelengths. This allows for numerous medical and biological applications. The presented systems utilizes four laser diodes that can be split into **short wavelengths** which are particular suitable to acquire metabolic information and **long wavelengths** which operate near the optical window of tissue in which high penetration depths are achieved and contrast agents can be imaged.

The presented medical application addresses the need to visualize human skin in a non-invasive manner. The ability to penetrate several $100\,\mu m$ was demonstrated on a multitude of volunteers. The skins microvasculature was imaged and due to the differential absorption of hemoglobin at the **short wavelengths**, oxygenation values at mesoscopic resolutions could be estimated.

For biological applications, it has been demonstrated that common contrast agents such as ICG can be visualized using the **long wavelengths** of MS-PWFD, in combination with the metabolic information of the **short wavelengths**. This presents the unprecedented opportunity to study contrast agents with respect to their biological environment at mesoscopic resolutions. Potentially, this can establish a reproducible relationship between observations in metabolic changes and effects that can only be made visible through contrast agents. Hence, besides enhancing the understanding of biological processes on a holistic level, such knowledge may help to reduce the need of conducting measurements aided by contrast agents.

Despite the promising results enabled by MS-PWFD, two major shortcomings were identified compared to conventional time domain mesoscopy. First, the resolution achieved did not fully match the theoretical expectations. Second, the limited pulse energy yielded an insufficient sensitivity for single-cell imaging and caused a rather high acquisition time. The limited accuracy can be addressed by deploying

stages with faster position encoders. This will reduce the position inaccuracy at a given projection to acceptable limits. In addition, software algorithms can be used to reduce the effect of position uncertainty. This could either be cross-correlation algorithms, similar to those used in motion correction, or could use a model for the actual position of the transducer to increase the accuracy [213]. Furthermore, the decreased resolution, due to motion of the transducer, may be reduced by diminishing the speed of the stage during measurements. This will increase the measurement time. Alternatively, a deconvolution algorithm can be used to correct the acquired data with the known speed and step size of the transducer. This could potentially increase the system's resolution, but would require further investigations.

Operating at frequencies well above 100 MHz introduces electromagnetic waves in the PCB with wavelengths shorter than 30 cm. To enable an efficient power transfer from the driver circuit to the laser diode, the wave impedance of both circuits must be matched. Typically, impedance matching can be achieved for a limited bandwidth only [214]. However, short pulses require a high bandwidth. Methods for broadband coupling have been explored and may be suitable to enhance the coupling for pulsed laser diodes [215].

Finally, the acquisition time is limited by the system being raster scanning which means all projections are acquired sequentially. Ultrasound arrays are available to capture the acoustic field across a line or an area. These arrays are typically non-focused and may not provide the sensitivity needed to perform MS-PWFD. Furthermore, when acquiring multiple pulses, the data increases proportionally. Even when using a single channel, this presents a significant challenge to the data acquisition and processing system. When multiple channels are to be used simultaneously, the amount of data generated may push the limits of what is currently technologically feasible. Recently, compressed sensing methods have sparked interest in optoacoustic imaging. These methods can reduce the amount of the acquired data significantly. It has been shown that sensitive optical ultrasound detectors based on etalons can be used in combination with compressed sensing [90]. These may present an attractive augmentation of MS-PWFD enabling it for real-time applications.

Acknowledgements

List of Figures

List of Tables

Bibliography

[1] Gordon H Guyatt. Evidence-based medicine. *ACP Journal Club*, 114(2):A16–A16, 1991.

[2] David M Eddy. Evidence-based medicine: a unified approach. *Health affairs*, 24(1):9–17, 2005.

[3] John Enderle and Joseph Bronzino. *Introduction to biomedical engineering.* Academic press, 2012.

[4] N Barrie Smith and A Webb. Introduction to medical imaging: Physics, engineering and clinical applications, 2010.

[5] William G Bradley. History of medical imaging. *Proceedings of the American Philosophical Society*, 152(3):349–361, 2008.

[6] Richard A Robb. *Biomedical imaging, visualization, and analysis.* John Wiley & Sons, Inc., 1999.

[7] Bhupinder Natt, Harold M Szerlip, and L Lee Hamm. The lost art of the history and physical. *The American journal of the medical sciences*, 348(5):423–425, 2014.

[8] José F Guadalajara Boo. Auscultation of the heart: an art on the road to extinction. *Gaceta medica de Mexico*, 151(2):260–265, 2015.

[9] W. C. Röntgen. *W. C. Röntgen: Ueber eine neue Art von Strahlen*, pages 2–16. Stahel'sche K. Hof- und Universitätsbuch- und Kunsthandlung, Würzburg, 1895.

[10] Clyde A. Brant, William E.; Helms. *Diagnostic Imaging Methods. Fundamentals of Diagnostic Radiology.* Lippincott Williams & Wilkins, Philadelphia, 2007.

[11] Dimitrios S Evangelopoulos, Simone Deyle, Heinz Zimmermann, and Aristomenis K Exadaktylos. Personal experience with whole-body, low-dosage, digital x-ray scanning (lodox-statscan) in trauma. *Scandinavian journal of trauma, resuscitation and emergency medicine*, 17(1):41, 2009.

[12] Elizabeth C Beckmann. Ct scanning the early days. *The British journal of radiology*, 79(937):5–8, 2006.

[13] Johann Radon. 1.1 über die bestimmung von funktionen durch ihre integralwerte längs gewisser mannigfaltigkeiten. *Classic papers in modern diagnostic radiology*, 5:21, 2005.

[14] He Wang, Sunil Krishnan, Xiaochun Wang, A Sam Beddar, Tina M Briere, Christopher H Crane, Radhe Mohan, and Lei Dong. Improving soft-tissue contrast in four-dimensional computed tomography images of liver cancer patients using a deformable image registration method. *International Journal of Radiation Oncology* Biology* Physics*, 72(1):201–209, 2008.

[15] Webb, W. Richard Brant, Wiliam E., and Nancy M. Major. *Fundamentals of Body CT.*, page 152. Elsevier Health Sciences., 2014.

[16] Amy Berrington de Gonzalez and Sarah Darby. Risk of cancer from diagnostic x-rays: estimates for the uk and 14 other countries. *The lancet*, 363(9406):345–351, 2004.

[17] David J Brenner and Eric J Hall. Computed tomography—an increasing source of radiation exposure. *New England Journal of Medicine*, 357(22):2277–2284, 2007.

[18] Erik Odeblad and Gunnar Lindström. Some preliminary observations on the proton magnetic resonance in biologic samples. *Acta Radiologica*, 43(6):469–476, 1955.

[19] Paul C Lauterbur et al. Image formation by induced local interactions: examples employing nuclear magnetic resonance. *nature*, 242(190), 1973.

[20] Acoustical Terminology. American national standard. *ANSI S1*, pages 1–1994, 2006.

[21] Richard SC Cobbold. *Foundations of biomedical ultrasound.* Oxford University Press, 2006.

[22] Mikael Haggstrom et al. Medical gallery of mikael haggstrom 2014. *WikiJournal of Medicine*, 1(2):1, 2014.

[23] Aladin Carovac, Fahrudin Smajlovic, and Dzelaludin Junuzovic. Application of ultrasound in medicine. *Acta Informatica Medica*, 19(3):168, 2011.

[24] F Stuart Foster, GR Lockwood, LK Ryan, KA Harasiewicz, L Berube, and AM Rauth. Principles and applications of ultrasound backscatter microscopy. *IEEE transactions on ultrasonics, ferroelectrics, and frequency control*, 40(5):608–617, 1993.

[25] Josef Flammer, Maneli Mozaffarieh, and Hans Bebie. The interaction between light and matter. In *Basic Sciences in Ophthalmology*, pages 21–39. Springer, 2013.

[26] Steven L Jacques. Optical properties of biological tissues: a review. *Physics in Medicine & Biology*, 58(11):R37, 2013.

[27] Peter Osypka. Fiber optic endoscope, January 14 1997. US Patent 5,593,405.

[28] Max Cutler. Transillumination as an aid in the diagnosis of breast lesions. *Surgery, gynecology and obstetrics*, 48:721–729, 1929.

[29] Frans F Jobsis. Noninvasive, infrared monitoring of cerebral and myocardial oxygen sufficiency and circulatory parameters. *Science*, 198(4323):1264–1267, 1977.

[30] Barabra Monsees, JM Destouet, and D Gersell. Light scan evaluation of nonpalpable breast lesions. *Radiology*, 163(2):467–470, 1987.

[31] Gary Strangman, David A Boas, and Jeffrey P Sutton. Non-invasive neuroimaging using near-infrared light. *Biological psychiatry*, 52(7):679–693, 2002.

[32] B Chance, JS Leigh, H Miyake, DS Smith, S Nioka, R Greenfeld, M Finander, K Kaufmann, W Levy, and M Young. Comparison of time-resolved and-unresolved measurements of deoxyhemoglobin in brain. *Proceedings of the National Academy of Sciences*, 85(14):4971–4975, 1988.

[33] David A Benaron and David K Stevenson. Optical time-of-flight and absorbance imaging of biologic media. *Science*, 259(5100):1463–1466, 1993.

[34] Maria Angela Franceschini, Vlad Toronov, Mattia E Filiaci, Enrico Gratton, and Sergio Fantini. On-line optical imaging of the human brain with 160-ms temporal resolution. *Optics express*, 6(3):49–57, 2000.

[35] Huabei Jiang, Brian W Pogue, Michael S Patterson, Keith D Paulsen, and Ulf L Osterberg. Simultaneous reconstruction of optical absorption and scattering maps in turbid media from near-infrared frequency-domain data. *Optics letters*, 20(20):2128–2130, 1995.

[36] Colin L. Smithpeter, Andrew K. Dunn, A. J. Welch, and Rebecca Richards-Kortum. Penetration depth limits of in vivo confocal reflectance imaging. *Appl. Opt.*, 37(13):2749–2754, May 1998.

[37] Colin J. R. Sheppard and David M. Shotton. *Confocal Laser Scanning Microscopy*, pages 37, 39–42. BIOS Scientific Publishers Limited, 1997.

[38] Alberto Diaspro, Paolo Bianchini, Giuseppe Vicidomini, Mario Faretta, Paola Ramoino, and Cesare Usai. Multi-photon excitation microscopy. *Biomedical engineering online*, 5(1):36, 2006.

[39] W Denk, JH Strickler, and WW Webb. Two-photon laser scanning fluorescence microscopy. *Science*, 248(4951):73–76, 1990.

[40] Fritjof Helmchen and Winfried Denk. Deep tissue two-photon microscopy. *Deep tissue two-photon microscopy*, 932-940, 2005.

[41] J. M. Schmitt. Optical coherence tomography (oct): a review. *IEEE Journal of Selected Topics in Quantum Electronics*, 5(4):1205–1215, July 1999.

[42] Boris I Gramatikov. Modern technologies for retinal scanning and imaging: an introduction for the biomedical engineer. *Biomedical engineering online*, 13(1):52, 2014.

[43] Zahid Yaqoob, Jigang Wu, and Changhuei Yang. Spectral domain optical coherence tomography: a better oct imaging strategy. *BioTechniques*, 39, 2005.

[44] Talisa E. de Carlo, Andre Romano, Nadia K. Waheed, and Jay S. Duker. A review of optical coherence tomography angiography (octa). *International Journal of Retina and Vitreous*, 1(1):5, Apr 2015.

[45] R. Huber, M. Wojtkowski, and J. G. Fujimoto. Fourier domain mode locking (fdml): A new laser operating regime and applications for optical coherence tomography. *Opt. Express*, 14(8):3225–3237, Apr 2006.

[46] Hans Breuer. *dtv-Atlas Physik, Band 1. Mechanik, Akustik, Thermodynamik, Optik*. dtv-Verlag, 1996.

[47] David J. Griffiths. *Introduction to Electrodynamics*. Prentice Hall, 2008.

[48] Wolfgang Demtröder. *Elektrizität und Optik (Experimentalphysik, Bd.2)*. Prentice Hall, Springer.

[49] Martin O Culjat, David Goldenberg, Priyamvada Tewari, and Rahul S Singh. A review of tissue substitutes for ultrasound imaging. *Ultrasound in medicine & biology*, 36(6):861–873, 2010.

[50] George M Hale and Marvin R Querry. Optical constants of water in the 200-nm to 200-μm wavelength region. *Applied optics*, 12(3):555–563, 1973.

[51] Robert LP van Veen, HJCM Sterenborg, A Pifferi, A Torricelli, and R Cubeddu. Determination of vis-nir absorption coefficients of mammalian fat, with time-and spatially resolved diffuse reflectance and transmission spectroscopy. In *Biomedical Topical Meeting*, page SF4. Optical Society of America, 2004.

[52] M.K. Moaveni. *A Multiple Scattering Field Theory Applied to Whole Blood*. PhD thesis, Dept. of Electrical Engineering, University of Washington, 1970.

[53] Yue Zhao, Lina Qiu, Yunlong Sun, Chong Huang, and Ting Li. Optimal hemoglobin extinction coefficient data set for near-infrared spectroscopy. *Biomedical optics express*, 8(11):5151–5159, 2017.

[54] Willem Gerrit Zijlstra, Anneke Buursma, and Onno Willem van Assendelft. *Visible and near infrared absorption spectra of human and animal haemoglobin: determination and application.* VSP, 2000.

[55] T Sarna and RC Sealy. Photoinduced oxygen consumption in melanin systems. action spectra and quantum yields for eumelanin and synthetic melanin. *Photochemistry and photobiology*, 39(1):69–74, 1984.

[56] PR Crippa, V t Cristofoletti, and N Romeo. A band model for melanin deduced from optical absorption and photoconductivity experiments. *Biochimica et Biophysica Acta (BBA)-General Subjects*, 538(1):164–170, 1978.

[57] ML Landsman, G Kwant, GA Mook, and WG Zijlstra. Light-absorbing properties, stability, and spectral stabilization of indocyanine green. *Journal of applied physiology*, 40(4):575–583, 1976.

[58] Gustav Mie. Beiträge zur optik trüber medien, speziell kolloidaler metallösungen. *Annalen der physik*, 330(3):377–445, 1908.

[59] AJ Cox, Alan J DeWeerd, and Jennifer Linden. An experiment to measure mie and rayleigh total scattering cross sections. *American Journal of Physics*, 70(6):620–625, 2002.

[60] Paolo Christillin. Nuclear compton scattering. *Journal of Physics G: Nuclear Physics*, 12(9):837, 1986.

[61] Griffiths David. Introduction to elementary particles, 1987.

[62] Lihong V Wang and Hsin-i Wu. *Biomedical optics: principles and imaging.* John Wiley & Sons, 2012.

[63] Lihong Wang, Steven L. Jacques, and Liqiong Zheng. Mcml—monte carlo modeling of light transport in multi-layered tissues. *Computer Methods and Programs in Biomedicine*, 47(2):131 – 146, 1995.

[64] Alexander Graham Bell. Art. xxxiv.–on the production and reproduction of sound by light. *American Journal of Science (1880-1910)*, 20(118):305, 1880.

[65] ML Viegerov. Eine methode der gasanalyse, beruhend auf der optisch-akustischen tyndall-röntgenerscheinung. In *Dokl. Akad. Nauk SSSR*, volume 19, pages 687–688, 1938.

[66] KF Luft. Über eine neue methode der registrierenden gasanalyse mit hilfe der absorption ultraroter strahlen ohne spektrale zerlegung. *Z. tech. Phys*, 24:97–104, 1943.

[67] A Korpel and LW Kessler. Comparison of methods of acoustic microscopy. In *Acoustical Holography*, pages 23–43. Springer, 1971.

[68] Allan Rosencwaig and Allen Gersho. Photoacoustic effect with solids: A theoretical treatment. *Science*, 190(4214):556–557, 1975.

[69] LB Kreuzer. Ultralow gas concentration infrared absorption spectroscopy. *Journal of Applied Physics*, 42(7):2934–2943, 1971.

[70] Frank BA Früngel. *Optical Pulses-Lasers-Measuring Techniques*. Academic Press, 2014.

[71] Vasilis Ntziachristos. Going deeper than microscopy: the optical imaging frontier in biology. *Nature Methods*, 2010.

[72] FJ McClung and RW Hellwarth. Giant optical pulsations from ruby. *Applied Optics*, 1(101):103–105, 1962.

[73] DC Hanna, B Luther-Davies, and RC Smith. Active q switching technique for producing high laser power in a single longitudinal mode. *Electronics Letters*, 8(15):369–370, 1972.

[74] John J Degnan. Optimization of passively q-switched lasers. *IEEE Journal of Quantum Electronics*, 31(11):1890–1901, 1995.

[75] Uddhav A Patil and Lakshyajit D Dhami. Overview of lasers. *Indian Journal of Plastic Surgery: Official Publication of the Association of Plastic Surgeons of India*, 41(Suppl):S101, 2008.

[76] JA Giordmaine and Robert C Miller. Tunable coherent parametric oscillation in linb o 3 at optical frequencies. *Physical Review Letters*, 14(24):973, 1965.

[77] SA Akhmanov, AI Kovrigin, AS Piskarskas, VV Fadeev, and RV Khokhlov. Observation of parametric amplification in the optical range. *Jetp Lett*, 2:191–193, 1965.

[78] Brian J Orr, MJ Johnson, and JG Haub. Spectroscopic applications of pulsed tunable optical parametric oscillators. *OPTICAL ENGINEERING-NEW YORK-MARCEL DEKKER INCORPORATED-*, 50:11–11, 1995.

[79] YX Fan, RC Eckardt, RL Byer, J Nolting, and R Wallenstein. Visible bab2o4 optical parametric oscillator pumped at 355 nm by a single-axial-mode pulsed source. *Applied physics letters*, 53(21):2014–2016, 1988.

[80] Olympus NDT Inc., 48 Woerd Avenue, Waltham MA 02453, USA. *Panametrics Ultrasound transducers*, 2010.

[81] Wallace Arden Smith, Avner Shaulov, and BA Auld. Tailoring the properties of composite piezoelectric materials for medical ultrasonic transducers. In *IEEE 1985 Ultrasonics Symposium*, pages 642–647. IEEE, 1985.

[82] Haifeng Wang and Wenwu Cao. Characterizing ultra-thin matching layers of high-frequency ultrasonic transducer based on impedance matching principle. *ieee transactions on ultrasonics, ferroelectrics, and frequency control*, 51(2):211–215, 2004.

[83] Pietro Patimisco, Gaetano Scamarcio, Frank K. Tittel, and Vincenzo Spagnolo. Quartz-enhanced photoacoustic spectroscopy: A review. *Sensors*, 14(4):6165–6206, 2014.

[84] GR Lockwood, DH Turnball, DA Christopher, and F Stuart Foster. Beyond 30 mhz [applications of high-frequency ultrasound imaging]. *IEEE Engineering in Medicine and Biology Magazine*, 15(6):60–71, 1996.

[85] F Stuart Foster, Kasia A Harasiewicz, and Michael D Sherar. A history of medical and biological imaging with polyvinylidene fluoride (pvdf) transducers. *IEEE transactions on ultrasonics, ferroelectrics, and frequency control*, 47(6):1363–1371, 2000.

[86] Daniel Rohrbach. *Quantitative ultrasound in transverse transmission for bone quality assessment and monitoring fracture healing*. PhD thesis, Humboldt-Universität zu Berlin, Mathematisch-Naturwissenschaftliche Fakultät I, 2013.

[87] Tomás E Gómez Álvarez-Arenas, Jorge Camacho, and Carlos Fritsch. Passive focusing techniques for piezoelectric air-coupled ultrasonic transducers. *Ultrasonics*, 67:85–93, 2016.

[88] Edward ZY Zhang and Paul C Beard. Ultrahigh-sensitivity wideband fabry-perot ultrasound sensors as an alternative to piezoelectric pvdf transducers for biomedical photoacoustic detection. In *Photons Plus Ultrasound: Imaging and Sensing*, volume 5320, pages 222–230. International Society for Optics and Photonics, 2004.

[89] M Lamont and PC Beard. 2d imaging of ultrasound fields using ccd array to map output of fabry-perot polymer film sensor. *Electronics Letters*, 42(3):187–189, 2006.

[90] Nam Huynh, Edward Zhang, Marta Betcke, Simon Arridge, Paul Beard, and Ben Cox. Single-pixel optical camera for video rate ultrasonic imaging. *Optica*, 3(1):26–29, 2016.

[91] Edward Zhang, Jan Laufer, and Paul Beard. Backward-mode multiwavelength photoacoustic scanner using a planar fabry-perot polymer film ultrasound sensor for high-resolution three-dimensional imaging of biological tissues. *Applied optics*, 47(4):561–577, 2008.

[92] István A Veres, Peter Burgholzer, Thomas Berer, Amir Rosenthal, Georg Wissmeyer, and Vasilis Ntziachristos. Characterization of the spatio-temporal response of optical fiber sensors to incident spherical waves. *The Journal of the Acoustical Society of America*, 135(4):1853–1862, 2014.

[93] Georg Wissmeyer, Dominik Soliman, Rami Shnaiderman, Amir Rosenthal, and Vasilis Ntziachristos. All-optical optoacoustic microscope based on wideband pulse interferometry. *Optics letters*, 41(9):1953–1956, 2016.

[94] Jens Horstmann and Ralf Brinkmann. Non-contact photoacoustic tomography using holographic full field detection. In *European Conference on Biomedical Optics*, page 880007. Optical Society of America, 2013.

[95] C Buj, J Horstmann, M Münter, and R Brinkmann. Speckle-based holographic detection for non-contact photoacoustic tomography. *Proc. Biomed. Tech*, 59:844, 2014.

[96] Robert G. Hunsperger. *Acousto-Optic Modulators*, pages 175–191. Springer Berlin Heidelberg, Berlin, Heidelberg, 2002.

[97] Frans J.M. Harren, Gina Cotti, Jos Oomens, and Sacco te Lintel Hekkert. *Photoacoustic Spectroscopy in Trace Gas Monitoring*. John Wiley & Sons, Ltd, 2006.

[98] W. C. Röntgen. Ueber Töne, welche durch intermittirende Bestrahlung eines Gases entstehen. *Annalen der Physik*, 248:155–159, 1881.

[99] John Tyndall. Action of an intermittent beam of radiant heat upon gaseous matter. *Journal of the Franklin Institute*, 111(4):297 – 308, 1881.

[100] William Henry Preece. I. on the conversion of radiant energy into sonorous vibrations. *Proceedings of the Royal Society of London*, 31(206-211):506–520, 1881.

[101] Ali Javan, William R Bennett Jr, and Donald R Herriott. Population inversion and continuous optical maser oscillation in a gas discharge containing a he-ne mixture. *Physical Review Letters*, 6(3):106, 1961.

[102] Paul A Remillard and Michael C Amorelli. Lock-in amplifier, May 11 1993. US Patent 5,210,484.

[103] John H Scofield. Frequency-domain description of a lock-in amplifier. *American Journal of Physics*, 62(2):129–133, 1994.

[104] Allan Rosencwaig. Photoacoustic spectroscopy of solids. *Optics Communications*, 7(4):305–308, 1973.

[105] Jeremy C Hebden, Simon R Arridge, and David T Delpy. Optical imaging in medicine: I. experimental techniques. *Physics in Medicine & Biology*, 42(5):825, 1997.

[106] AP Gibson, JC Hebden, and Simon R Arridge. Recent advances in diffuse optical imaging. *Physics in Medicine & Biology*, 50(4):R1, 2005.

[107] Allan Rosencwaig. Photoacoustic spectroscopy of biological materials. *Science*, 181(4100):657–658, 1973.

[108] Roger M Leblanc and Germain Puccetti. Photoacoustic spectroscopy applied to biological materials. In *Analytical Use of Fluorescent Probes in Oncology*, pages 59–64. Springer, 1996.

[109] C Buschmann. Photoacoustic investigation of biological materials. *FORTSCHRITTE DER AKUSTIK*, 28:440–441, 2002.

[110] CGA Hoelen, FFM De Mul, R Pongers, and A Dekker. Three-dimensional photoacoustic imaging of blood vessels in tissue. *Optics letters*, 23(8):648–650, 1998.

[111] Xueding Wang, Yongjiang Pang, Geng Ku, Xueyi Xie, George Stoica, and Lihong V Wang. Noninvasive laser-induced photoacoustic tomography for structural and functional in vivo imaging of the brain. *Nature biotechnology*, 21(7):803, 2003.

[112] Robert A Kruger, William L Kiser, Daniel R Reinecke, Gabe A Kruger, and Kathy D Miller. Thermoacoustic molecular imaging of small animals. *Molecular Imaging*, 2(2):15353500200303109, 2003.

[113] A Buehler, XL Deán-Ben, J Claussen, V Ntziachristos, and D Razansky. Three-dimensional optoacoustic tomography at video rate. *Optics express*, 20(20):22712–22719, 2012.

[114] Minghua Xu and Lihong V Wang. Universal back-projection algorithm for photoacoustic computed tomography. *Physical Review E*, 71(1):016706, 2005.

[115] X Luís Dean-Ben, Andreas Buehler, Vasilis Ntziachristos, and Daniel Razansky. Accurate model-based reconstruction algorithm for three-dimensional optoacoustic tomography. *IEEE Transactions on Medical Imaging*, 31(10):1922–1928, 2012.

[116] Daniel Razansky, Claudio Vinegoni, and Vasilis Ntziachristos. Multispectral photoacoustic imaging of fluorochromes in small animals. *Optics letters*, 32(19):2891–2893, 2007.

[117] Rui Ma, Adrian Taruttis, Vasilis Ntziachristos, and Daniel Razansky. Multispectral optoacoustic tomography (msot) scanner for whole-body small animal imaging. *Optics express*, 17(24):21414–21426, 2009.

[118] Daniel Razansky, Andreas Buehler, and Vasilis Ntziachristos. Volumetric real-time multispectral optoacoustic tomography of biomarkers. *Nature protocols*, 6(8):1121, 2011.

[119] Max Masthoff, Anne Helfen, Jing Claussen, Wolfgang Roll, Angelos Karlas, Heidemarie Becker, Gert Gabriëls, Jan Riess, Walter Heindel, Michael Schäfers, et al. Multispectral optoacoustic tomography of systemic sclerosis. *Journal of biophotonics*, page e201800155, 2018.

[120] Josefine Reber, Monja Willershäuser, Angelos Karlas, Korbinian Paul-Yuan, Gael Diot, Daniela Franz, Tobias Fromme, Saak V Ovsepian, Nicolas Bézière, Elena Dubikovskaya, et al. Non-invasive measurement of brown fat metabolism based on optoacoustic imaging of hemoglobin gradients. *Cell metabolism*, 27(3):689–701, 2018.

[121] Tony Wilson. Confocal microscopy. *Academic Press: London, etc*, 426:1–64, 1990.

[122] Fritjof Helmchen and Winfried Denk. Deep tissue two-photon microscopy. *Nature methods*, 2(12):932, 2005.

[123] Hao F Zhang and Daniel Razansky. Special issue introduction: Photoacoustic microscopy., 2016.

[124] Junjie Yao and Lihong V Wang. Photoacoustic microscopy. *Laser & photonics reviews*, 7(5):758–778, 2013.

[125] Lihong V Wang and Song Hu. Photoacoustic tomography: in vivo imaging from organelles to organs. *science*, 335(6075):1458–1462, 2012.

[126] George J Tserevelakis, Dominik Soliman, Murad Omar, and Vasilis Ntziachristos. Hybrid multiphoton and optoacoustic microscope. *Optics letters*, 39(7):1819–1822, 2014.

[127] Dominik Soliman, George J Tserevelakis, Murad Omar, and Vasilis Ntziachristos. Combined label-free optical and optoacoustic imaging of model organisms at mesoscopy and microscopy resolutions. In *Photons Plus Ultrasound: Imaging and Sensing 2016*, volume 9708, page 97083B. International Society for Optics and Photonics, 2016.

[128] Song Hu, Konstantin Maslov, and Lihong V Wang. Second-generation optical-resolution photoacoustic microscopy with improved sensitivity and speed. *Optics letters*, 36(7):1134–1136, 2011.

[129] Murad Omar, Mathias Schwarz, Dominik Soliman, Panagiotis Symvoulidis, and Vasilis Ntziachristos. Pushing the optical imaging limits of cancer with multi-frequency-band raster-scan optoacoustic mesoscopy (rsom). *Neoplasia*, 17(2):208–214, 2015.

[130] L. V. Wang. Tutorial on photoacoustic microscopy and computed tomography. *IEEE Journal of Selected Topics in Quantum Electronics*, 14(1):171–179, Jan 2008.

[131] Martin Greenspan and Carroll E Tschiegg. Tables of the speed of sound in water. *The Journal of the Acoustical Society of America*, 31(1):75–76, 1959.

[132] John David Jackson. *Classical electrodynamics*, pages 125–127. Wiley, New York, NY, 3rd ed. edition, 1999.

[133] Chulhong Kim, Todd N Erpelding, Ladislav Jankovic, Michael D Pashley, and Lihong V Wang. Deeply penetrating in vivo photoacoustic imaging using a clinical ultrasound array system. *Biomedical optics express*, 1(1):278–284, 2010.

[134] Meng Yang, Lingyi Zhao, Xujin He, Na Su, ChenYang Zhao, Hewen Tang, Tao Hong, Wenbo Li, Fang Yang, Lin Lin, et al. Photoacoustic/ultrasound dual imaging of human thyroid cancers: an initial clinical study. *Biomedical optics express*, 8(7):3449–3457, 2017.

[135] Mithun Kuniyil Ajith Singh, Naoto Sato, and Toshitaka Agano. Acousticx: Handheld led-based multispectral photoacoustic/ultrasound imaging system. *Nature Methods*, 11 2017.

[136] Lihong V Wang. Multiscale photoacoustic microscopy and computed tomography. *Nature photonics*, 3(9):503, 2009.

[137] RA Lemons and CF Quate. Acoustic microscope—scanning version. *Applied Physics Letters*, 24(4):163–165, 1974.

[138] Guenther Paltauf, JA Viator, SA Prahl, and SL Jacques. Iterative reconstruction algorithm for optoacoustic imaging. *The Journal of the Acoustical Society of America*, 112(4):1536–1544, 2002.

[139] Amir Rosenthal, Vasilis Ntziachristos, and Daniel Razansky. Acoustic inversion in optoacoustic tomography: A review. *Current medical imaging reviews*, 9(4):318—336, November 2013.

[140] Lu Ding, Xosé Luís Deán-Ben, and Daniel Razansky. 20 frames per second model-based reconstruction in cross-sectional optoacoustic tomography. In *Photons Plus Ultrasound: Imaging and Sensing 2017*, volume 10064, page 100641A. International Society for Optics and Photonics, 2017.

[141] Vasilis Ntziachristos and Daniel Razansky. Molecular imaging by means of multispectral optoacoustic tomography (msot). *Chemical reviews*, 110(5):2783–2794, 2010.

[142] Lu Ding, Xosé Luís Deán-Ben, Neal C Burton, Robert W Sobol, Vasilis Ntziachristos, and Daniel Razansky. Constrained inversion and spectral unmixing in multispectral optoacoustic tomography. *IEEE transactions on medical imaging*, 36(8):1676–1685, 2017.

[143] Yun He, Lidai Wang, Junhui Shi, Junjie Yao, Lei Li, Ruiying Zhang, Chih-Hsien Huang, Jun Zou, and Lihong V Wang. In vivo label-free photoacoustic flow cytography and on-the-spot laser killing of single circulating melanoma cells. *Scientific reports*, 6:39616, 2016.

[144] JJ Zayhowski, J Ochoa, and A Mooradian. Gain-switched pulsed operation of microchip lasers. *Optics letters*, 14(23):1318–1320, 1989.

[145] GJ Spühler, R Paschotta, R Fluck, B Braun, M Moser, G Zhang, E Gini, and U Keller. Experimentally confirmed design guidelines for passively q-switched microchip lasers using semiconductor saturable absorbers. *JOSA B*, 16(3):376–388, 1999.

[146] John J Zayhowski. Microchip lasers. In *Handbook of Solid-State Lasers*, pages 359–402. Elsevier, 2013.

[147] Gunnar Arisholm. Quantum noise initiation and macroscopic fluctuations in optical parametric oscillators. *JOSA B*, 16(1):117–127, 1999.

[148] Mathias Schwarz, Andreas Buehler, Juan Aguirre, and Vasilis Ntziachristos. Three-dimensional multispectral optoacoustic mesoscopy reveals melanin and blood oxygenation in human skin in vivo. *Journal of biophotonics*, 9(1-2):55–60, 2016.

[149] Roy GM Kolkman, Wiendelt Steenbergen, and Ton G van Leeuwen. In vivo photoacoustic imaging of blood vessels with a pulsed laser diode. *Lasers in medical science*, 21(3):134–139, 2006.

[150] Khalid Daoudi, PJ Van Den Berg, O Rabot, A Kohl, S Tisserand, P Brands, and Wiendelt Steenbergen. Handheld probe integrating laser diode and ultrasound transducer array for ultrasound/photoacoustic dual modality imaging. *Optics express*, 22(21):26365–26374, 2014.

[151] Tianheng Wang, Sreyankar Nandy, Hassan S Salehi, Patrick D Kumavor, and Quing Zhu. A low-cost photoacoustic microscopy system with a laser diode excitation. *Biomedical optics express*, 5(9):3053–3058, 2014.

[152] Paul Kumar Upputuri and Manojit Pramanik. Pulsed laser diode based optoacoustic imaging of biological tissues. *Biomedical Physics & Engineering Express*, 1(4):045010, 2015.

[153] Toshitaka Agano, Naoto Sato, Hitoshi Nakatsuka, Kazuo Kitagawa, Takamitsu Hanaoka, Koji Morisono, and Yusuke Shigeta. Comparative experiments of photoacoustic system using laser light source and led array light source. In *Photons Plus Ultrasound: Imaging and Sensing 2015*, volume 9323, page 93233X. International Society for Optics and Photonics, 2015.

[154] Thomas J Allen and Paul C Beard. High power visible light emitting diodes as pulsed excitation sources for biomedical photoacoustics. *Biomedical optics express*, 7(4):1260–1270, 2016.

[155] Xianjin Dai, Hao Yang, and Huabei Jiang. In vivo photoacoustic imaging of vasculature with a low-cost miniature light emitting diode excitation. *Optics letters*, 42(7):1456–1459, 2017.

[156] JS Speck and SF Chichibu. Nonpolar and semipolar group iii nitride-based materials. *MRS bulletin*, 34(5):304–312, 2009.

[157] Désirée Queren, Adrian Avramescu, Georg Brüderl, Andreas Breidenassel, Marc Schillgalies, Stephan Lutgen, and Uwe Strauß. 500 nm electrically driven ingan based laser diodes. *Applied Physics Letters*, 94(8):081119, 2009.

[158] Adrian Avramescu, Teresa Lermer, Jens Müller, Christoph Eichler, Georg Bruederl, Matthias Sabathil, Stephan Lutgen, and Uwe Strauss. True green laser diodes at 524 nm with 50 mw continuous wave output power on c-plane gan. *Applied physics express*, 3(6):061003, 2010.

[159] AJ Hymans and J Lait. Analysis of a frequency-modulated continuous-wave ranging system. *Proceedings of the IEE-Part B: electronic and communication engineering*, 107(34):365–372, 1960.

[160] Mateusz Malanowski and Krzysztof Kulpa. Detection of moving targets with continuous-wave noise radar: theory and measurements. *IEEE Transactions on Geoscience and Remote Sensing*, 50(9):3502–3509, 2012.

[161] Shuang Gao and Rongqing Hui. Frequency-modulated continuous-wave lidar using i/q modulator for simplified heterodyne detection. *Optics letters*, 37(11):2022–2024, 2012.

[162] Edward C Farnett and George H Stevens. Pulse compression radar. *Radar handbook*, 2:10–1, 1990.

[163] Stephan Kellnberger, Nikolaos C Deliolanis, Daniel Queirós, George Sergiadis, and Vasilis Ntziachristos. In vivo frequency domain optoacoustic tomography. *Optics letters*, 37(16):3423–3425, 2012.

[164] Bahman Lashkari and Andreas Mandelis. Comparison between pulsed laser and frequency-domain photoacoustic modalities: signal-to-noise ratio, contrast, resolution, and maximum depth detectivity. *Review of Scientific Instruments*, 82(9):094903, 2011.

[165] Sreekumar Kaiplavil and Andreas Mandelis. Highly depth-resolved chirped pulse photothermal radar for bone diagnostics. *Review of Scientific Instruments*, 82(7):074906, 2011.

[166] Alexander Melnikov, Liangjie Chen, Diego Ramirez Venegas, Koneswaran Sivagurunathan, Qiming Sun, Andreas Mandelis, and Ignacio Rojas Rodriguez. Single frequency thermal wave radar: A next-generation dynamic thermography for quantitative non-destructive imaging over wide modulation frequency ranges. *Review of Scientific Instruments*, 89(4):044901, 2018.

[167] Bahman Lashkari and Andreas Mandelis. Photoacoustic radar imaging signal-to-noise ratio, contrast, and resolution enhancement using nonlinear chirp modulation. *Optics letters*, 35(10):1623–1625, 2010.

[168] Todd W Murray, Suraj Bramhavar, Ashwin Sampathkumar, and Bruno Pouet. Theory and applications of frequency domain photoacoustic microscopy. *The Journal of the Acoustical Society of America*, 123(5):3370–3370, 2008.

[169] Gregor Langer, Bianca Buchegger, Jaroslaw Jacak, Thomas A Klar, and Thomas Berer. Frequency domain photoacoustic and fluorescence microscopy. *Biomedical optics express*, 7(7):2692–2702, 2016.

[170] Deepu George, Harriet Lloyd, Ronald H Silverman, and Parag V Chitnis. A frequency-domain non-contact photoacoustic microscope based on an adaptive interferometer. *Journal of biophotonics*, 2018.

[171] Hui Fang, Konstantin Maslov, and Lihong V Wang. Photoacoustic doppler flow measurement in optically scattering media. *Applied Physics Letters*, 91(26):264103, 2007.

[172] Konstantin I Maslov and Lihong V Wang. Photoacoustic imaging of biological tissue with intensity-modulated continuous-wave laser. *Journal of biomedical optics*, 13(2):024006, 2008.

[173] Boaz Rafaely, Barak Weiss, and Eitan Bachmat. Spatial aliasing in spherical microphone arrays. *IEEE Transactions on Signal Processing*, 55(3):1003–1010, 2007.

[174] ANSI Standard. Z136. 1. american national standard for the safe use of lasers. american national standards institute. *Inc., New York*, 1993.

[175] Da-Kang Yao, Chi Zhang, Konstantin I Maslov, and Lihong V Wang. Photoacoustic measurement of the grüneisen parameter of tissue. *Journal of biomedical optics*, 19(1):017007, 2014.

[176] Wolfram Müller, Timothy G Lohman, Arthur D Stewart, Ronald J Maughan, Nanna L Meyer, Luis B Sardinha, Nuwanee Kirihennedige, Alba Reguant-Closa, Vanessa Risoul-Salas, Jorunn Sundgot-Borgen, et al. Subcutaneous fat patterning in athletes: selection of appropriate sites and standardisation of a novel ultrasound measurement technique: ad hoc working group on body composition, health and performance, under the auspices of the ioc medical commission. *Br J Sports Med*, 50(1):45–54, 2016.

[177] Antonios Stylogiannis, Ludwig Prade, Andreas Buehler, Juan Aguirre, George Sergiadis, and Vasilis Ntziachristos. Continuous wave laser diodes enable fast optoacoustic imaging. *Photoacoustics*, 9:31–38, 2018.

[178] Garo Khanarian. Optical properties of cyclic olefin copolymers. *Optical Engineering*, 40(6):1024–1030, 2001.

[179] Tim Jerman, Franjo Pernuš, Boštjan Likar, and Žiga Špiclin. Enhancement of vascular structures in 3d and 2d angiographic images. *IEEE transactions on medical imaging*, 35(9):2107–2118, 2016.

[180] X Luís Deán-Ben, Andre C Stiel, Yuanyuan Jiang, Vasilis Ntziachristos, Gil G Westmeyer, and Daniel Razansky. Imaging the distribution of photoswitchable probes with temporally-unmixed multispectral optoacoustic tomography. In *Photons Plus Ultrasound: Imaging and Sensing 2016*, volume 9708, page 970825. International Society for Optics and Photonics, 2016.

[181] Paul Vetschera, Kanuj Mishra, Juan-Pablo Fuenzalida Werner, Andriy Chmyrov, Vasilis Ntziachristos, and Andre C Stiel. Characterization of reversibly switchable fluorescent proteins (rsfps) in optoacoustic imaging. *Analytical chemistry*, 2018.

[182] Excelitas. *Pulsed Laser Diodes – PGA – PGEW Series.*

[183] BPJ Bret, TL Sonnemans, and TW Hijmans. Capturing a light pulse in a short high-finesse cavity. *Physical Review A*, 68(2):023807, 2003.

[184] Richard Y Chiao and Xiaohui Hao. Coded excitation for diagnostic ultrasound: A system developer's perspective. In *Ultrasonics, 2003 IEEE Symposium on*, volume 1, pages 437–448. IEEE, 2003.

[185] Cheng Jin, Si-ping Chen, Tian-fu Wang, et al. A new scheme of coded ultrasound using golay codes. *Journal of Zhejiang University SCIENCE C*, 11(6):476–480, 2010.

[186] Martin P Mienkina, Annika Eder, Georg Schmitz, Claus-Stefan Friedrich, Nils C Gerhardt, and Martin R Hofmann. Simulation study of photoacoustic coded excitation using golay codes. In *Ultrasonics Symposium, 2008. IUS 2008. IEEE*, pages 1242–1245. IEEE, 2008.

[187] Ali Hariri, Jeanne Lemaster, Junxin Wang, AnanthaKrishnan S Jeevarathinam, Daniel L Chao, and Jesse V Jokerst. The characterization of an economic and portable led-based photoacoustic imaging system to facilitate molecular imaging. *Photoacoustics*, 9:10–20, 2018.

[188] Martin P Mienkina, Claus-Stefan Friedrich, Nils C Gerhardt, Martin F Beckmann, Martin F Schiffner, Martin R Hofmann, and Georg Schmitz. Multispectral photoacoustic coded excitation imaging using unipolar orthogonal golay codes. *Optics Express*, 18(9):9076–9087, 2010.

[189] Juan Aguirre, Mathias Schwarz, Dominik Soliman, Andreas Buehler, Murad Omar, and Vasilis Ntziachristos. Broadband mesoscopic optoacoustic tomography reveals skin layers. *Optics letters*, 39(21):6297–6300, 2014.

[190] Shin Yoneya, Tamiya Saito, Yoshiko Komatsu, Iwao Koyama, Keiichi Takahashi, and Josephine Duvoll-Young. Binding properties of indocyanine green in human blood. *Investigative ophthalmology & visual science*, 39(7):1286–1290, 1998.

[191] J Caesar. The use of indocyanine green in the measurement of hepatic blood flow and as a test of hepatic function. *Clin. Sci.*, 21:43–57, 1961.

[192] Albert J Augustin. Grundzüge der angiographie. In *Augenheilkunde*, pages 917–960. Springer, 2001.

[193] G Moneta, M Brülisauer, K Jäger, and A Bollinger. Infrared fluorescence videomicroscopy of skin capillaries with indocyanine green. *International journal of microcirculation, clinical and experimental*, 6(1):25–34, 1987.

[194] Christopher J Gostout and Steven L Jacques. Infrared video imaging of subsurface vessels: a feasibility study for the endoscopic management of gastrointestinal bleeding. *Gastrointestinal endoscopy*, 41(3):218–224, 1995.

[195] Edward C Bradley, John W Barr, et al. Determination of blood volume using indocyanine green (cardio-green (r)) dye. *Life sciences*, 7:1001–1007, 1968.

[196] Christian Lutzweiler, Reinhard Meier, Ernst Rummeny, Vasilis Ntziachristos, and Daniel Razansky. Real-time optoacoustic tomography of indocyanine green perfusion and oxygenation parameters in human finger vasculature. *Optics letters*, 39(14):4061–4064, 2014.

[197] Xosé Luís Deán-Ben, Steven James Ford, and Daniel Razansky. High-frame rate four dimensional optoacoustic tomography enables visualization of cardiovascular dynamics and mouse heart perfusion. *Scientific reports*, 5:10133, 2015.

[198] Zhenyue Chen, Xosé Luís Deán-Ben, Sven Gottschalk, and Daniel Razansky. Performance of optoacoustic and fluorescence imaging in detecting deep-seated fluorescent agents. *Biomedical optics express*, 9(5):2229–2239, 2018.

[199] Gerard A Lutty. The acute intravenous toxicity of biological stains, dyes, and other fluorescent substances. *Toxicology and applied pharmacology*, 44(2):225–249, 1978.

[200] DKF Meijer, B Weert, and GA Vermeer. Pharmacokinetics of biliary excretion in man. vi. indocyanine green. *European journal of clinical pharmacology*, 35(3):295–303, 1988.

[201] ICG-Pulsion Data Sheet. Pulsion medizintechnik.

[202] John Emsley. *Nature's building blocks: an AZ guide to the elements.* Oxford University Press, 2011.

[203] K Matthes. Untersuchungen über die sauerstoffsättigung des menschlichen arterienblutes. *Naunyn-Schmiedebergs Archiv für experimentelle Pathologie und Pharmakologie*, 179(6):698–711, 1935.

[204] Glenn A Millikan. The oximeter, an instrument for measuring continuously the oxygen saturation of arterial blood in man. *Review of scientific Instruments*, 13(10):434–444, 1942.

[205] Sonnia Maria Lopez Silva, María Luisa Dotor Castilla, and Juan Pedro Silveira Martín. Near-infrared transmittance pulse oximetry with laser diodes. *Journal of Biomedical Optics*, 8(3):525–534, 2003.

[206] Nitin Shah, Hamsa B Ragaswamy, Kavitha Govindugari, and Laverne Estanol. Performance of three new-generation pulse oximeters during motion and low perfusion in volunteers. *Journal of clinical anesthesia*, 24(5):385–391, 2012.

[207] Stratis Tzoumas, Antonio Nunes, Ivan Olefir, Stefan Stangl, Panagiotis Symvoulidis, Sarah Glasl, Christine Bayer, Gabriele Multhoff, and Vasilis Ntziachristos. Eigenspectra optoacoustic tomography achieves quantitative blood oxygenation imaging deep in tissues. *Nature communications*, 7:ncomms12121, 2016.

[208] Christine L Chaffer and Robert A Weinberg. A perspective on cancer cell metastasis. *Science*, 331(6024):1559–1564, 2011.

[209] Patricia S Steeg. Tumor metastasis: mechanistic insights and clinical challenges. *Nature medicine*, 12(8):895, 2006.

[210] Vicki Plaks, Charlotte D Koopman, and Zena Werb. Circulating tumor cells. *Science*, 341(6151):1186–1188, 2013.

[211] Jocelyn Kaiser. Cancer's circulation problem. *Science*, 327(5969):1072–1074, 2010.

[212] Ekaterina I Galanzha, Evgeny V Shashkov, Paul M Spring, James Y Suen, and Vladimir P Zharov. In vivo, noninvasive, label-free detection and eradication of circulating metastatic melanoma cells using two-color photoacoustic flow cytometry with a diode laser. *Cancer research*, 69(20):7926–7934, 2009.

[213] Mathias Schwarz, Natalie Garzorz-Stark, Kilian Eyerich, Juan Aguirre, and Vasilis Ntziachristos. Motion correction in optoacoustic mesoscopy. *Scientific reports*, 7(1):10386, 2017.

[214] P Biernacki and Alan R Mickelson. Impedance matching of laser diodes using packaged microstrip lines: active and passive. In *Lasers and Electro-Optics Society Annual Meeting, 1995. 8th Annual Meeting Conference Proceedings, Volume 1., IEEE*, volume 1, pages 238–239. IEEE, 1995.

[215] Carolina Regoli. Impedance matching by using a multi-stub system. *Proceedings of the 7th WSEAS International Conference on Simulation, Modelling and Optimization, Beijing, China*, 2007.